UNIVERSIDAD DE EXTREMADURA

TESIS DOCTORAL

TÍTULO: Propiedades estructurales y termofísicas de modelos de partículas Janus con orientación fija.

AUTOR: Miguel Ángel González Maestre.

PROGRAMA: Modelización y Experimentación en Ciencia y Tecnología (R007).

AÑO DE LECTURA: 2021

UNIVERSIDAD DE EXTREMADURA

TESIS DOCTORAL

TÍTULO: Propiedades estructurales y termofísicas de modelos de partículas Janus con orientación fija.

AUTOR: Miguel Ángel González Maestre.

PROGRAMA: Modelización y Experimentación en Ciencia y Tecnología (R007).

AÑO DE LECTURA: 2021

Conformidad de los directores de la tesis (La conformidad de los directores de la tesis consta en el original de esta Tesis Doctoral):

DIRECTOR: Andrés Santos Reyes.

Firma: ……..

CODIRECTOR: Riccardo Fantoni.

Firma: ……..

Acknowledgements

No other way to start, except by paying hommage to those who made this thesis possible.

First of all, to my family, especially my grandparents *Manuel and Estilita*. Because their love is not of this world.

During my years as a student, I was privileged by working alongside with many scientists and colleagues from my research group: *Vicente Garzó, Santos Bravo Yuste, Enrique Abad, Antonio Astillero, Moisés García Chamorro, Juan Jesús Ruiz Lorenzo, and Mariano López de Haro*. With such a team, even the hardest challenge seems a piece of cake.

In addition, I would like to express my thanks to Riccardo Fantoni. His wise comments were very useful in many stages of my work.

Mention apart deserves Professor Andrés Santos. Though impressive, the gifted insight he possesses is nothing compared with his humanity and kindness.

My sincere gratitude to them all.

Summary

This thesis studies various systems made of Janus particles. Firstly, we start calculating the equilibrium properties of the one-dimensional fluid. The system is composed of particles with two faces, so that the pair interaction is that of hard rods, except if the two active faces are in front of each other, in which case the interaction has a square-well attractive tail. Our exact solution refers to *quenched* systems (i.e., each particle has a fixed face orientation). Comparison between theoretical results and Monte Carlo simulations for quenched and *annealed* (i.e. each particle can dynamically flip its face and orientation) systems, respectively, shows an excellent agreement.

On the other hand, the analytical approach in three dimensions hinges on a mapping of the above Janus fluid onto a quenched binary mixture interacting via a "quasi" isotropic potential and formed by colloidal spheres with the hydrophobic hemisphere constrained to point either up or down. The anisotropic nature of the original Kern–Frenkel potential is reflected by the asymmetry in the interactions occurring between the unlike components of the mixture. A rational-function approximation extending the corresponding symmetric case is obtained in the sticky limit, where the square-well becomes infinitely narrow and deep, and allows for a fully analytical approach. Notwithstanding the rather drastic approximations in the analytical theory, this is shown to provide a rather precise estimate of the structural and thermodynamical properties of the quenched fluid simulated through the Monte Carlo method.

Finally, a class of quenched asymmetric binary mixtures formed by colloidal Janus spherical particles with the attractive hemisphere constrained to point either up or down are studied by means of Gibbs ensemble Monte Carlo simulations and simple analytical approximations. The gas-liquid and demixing phase transitions for each of five choices of the patch-patch affinities are analyzed. It is found that a gas-liquid transition is present in all the models, even if only one of the four possible patch-patch interactions is attractive. Moreover, provided the attraction between

like particles is stronger than between unlike particles, the system demixes into two subsystems with different composition at sufficiently low temperatures and high densities.

Resumen

Esta tesis abordará el estudio de varios sistemas compuestos por partículas de Janus. En primer lugar, calcularemos las propiedades en equilibrio del fluido unidimensional, cuyas partículas presentan dos regiones bien diferenciadas, con potencial de esfera dura excepto si las dos regiones activas interaccionan, tomando entonces la forma del potencial de pozo cuadrado. La solución analítica corresponde al sistema *quenched* (con orientaciones fijas en una dirección del espacio). En cualquier caso, la comparación entre los resultados teóricos y simulaciones, tanto para el caso quenched como *annealed* (orientaciones libres) muestra un acuerdo excelente.

Por otra parte, el desarrollo analítico en tres dimensiones se basará en mapear el fluido en una mezcla binaria que interactúa mediante un potencial "cuasi" isotrópico y formado por esferas coloidales cuyos hemisferios hidrofóbicos apuntan arriba o abajo. La naturaleza anisotrópica del potencial de Kern–Frenkel original se verá reflejada por la asimetría en las interacciones entre los diferentes componente de la mezcla. Una aproximación del tipo RFA (Rational Function Approximation), extendiendo el correspondiente caso simétrico, es obtenida para el caso de atracción adhesiva (*sticky)*, donde el potencial pozo se convierte en infinitamente estrecho y profundo, permitiendo un estudio analítico. A pesar de implementar una aproximación tan drástica, los resultados proporcionan una estimación precisa de las propiedades estructurales y termodinámicas del fluido *quenched* simulado mediante el método de Monte Carlo.

Por último, una mezcla binaria del fluido de Janus, formado por esferas coloidales con hemisferios hodrófóbico alineados en una dirección (arriba o abajo), será estudiada por medio de simulaciones de Monte Carlo en la colectividad de Gibbs, junto con aproximaciones analíticas. A su vez, tanto las transiciones líquido-gas como la separación de fases (*demixing*) serán analizados en cinco modelos específicos con diferentes afinidades entre los hemisferios, descubriendo que la transición *demixing* se haya presente en los cinco modelos, incluso si solo una de las cuatro posibles

interacciones es atractiva.

Sin embargo, si la atracción entre partículas similares es más fuerte que entre partículas diferentes, el sistema se dividirá en dos subsistemas con diferente composición, para una temperatura suficientemente baja a alta densidad.

Contents

List of Figures

Que un individuo quiera despertar
en otro individuo *pensamientos*
que no pertenecieron más que a un
tercero, es una paradoja evidente.

Jorge Luis Borges, *Evaristo Carriego.*

Le véritable voyage de découverte
ne consiste pas à chercher de
nouveaux paysages, mais à avoir
de nouveaux yeux.

Marcel Proust, *À la recherche du temps perdu.*

Et lux in tenebris lucet.

John 1,5.

1

General Introduction

The study of colloidal particles has been a subject of increasing interest in the last decades, not only due to the numerous technological applications associated with these systems, but also regarding their fundamental role within liquid theory [1, 2].

Many of the mathematical models describing colloids were linked from their very inception to the concept of patchy particles, in which uniform spheres present a surface region (called a *patch*) with an interaction pattern different from that of the rest of the surface. Simple as it may seem, this approach of adding a little *patchy* impurity on the homogeneous chemical surface endows the corresponding fluid model with a good deal of rich features providing a powerful tool to get a better understanding of their aggregation properties (regarding both organic and

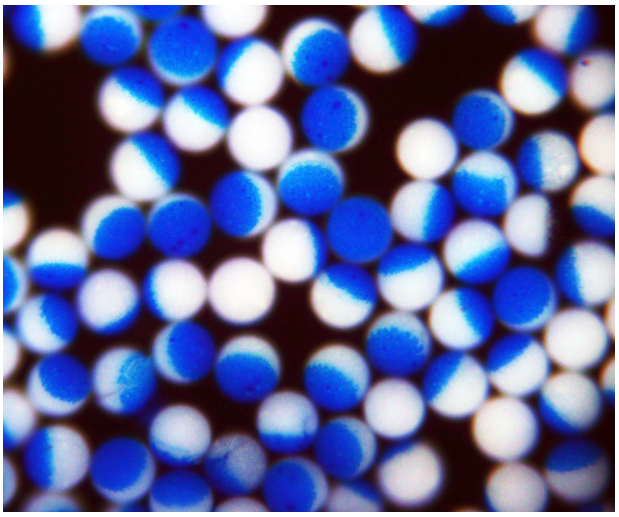

FIGURE 1.1: Opaque Microspheres for coatings in industrial implementations. Source: Yelena Lipovetskaya.

inorganic molecules), colloidal hierarchical structures (micelles, vesicles, nanocomposites, polymers, etc.), and eventually, laboratory synthesis of new materials. As a matter of fact, material science has experienced a true revolution thanks to the unprecedented development of innovative techniques related not only to the chemical but also physical or mechanical synthesis technology. This avant-garde processes are generating new sets of colloidal particles with a wide range of size, composition, and anisotropic patch structure [3, 4, 5] (see Fig. 1.1).

Janus fluids are made of colloidal-size particles whose surface is divided into two symmetric regions (patches) with different properties (for example, chemical composition), thus presenting different behaviors [5, 6, 7]. The lack of centrosymmetry inherent to the pair potential yields a dynamic and vigorous surface activity derived from its anisotropic character, in some cases more interactional than a uniform particle in the same context [8]. The remarkable precision of these avant-garde methods of synthesis makes it possible to obtain experimental results involving chainlike or one-dimensional arrays of Janus particles [9, 10].

Analysis of Janus particles lies in the focus of many scientific fields, ranging from physics and chemistry, to biological systems and active matter. As may be observed from databases indexes, the academic efforts devoted to the study of

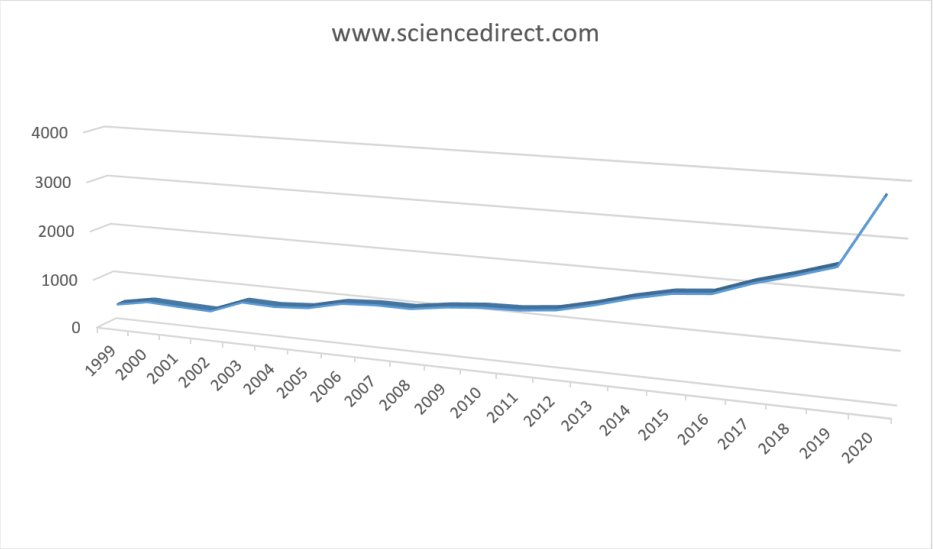

FIGURE 1.2: Appearance by year of the word "Janus" in the headline of papers recorded by the web **www.sciencedirect.com**.

these particles has been steadily rising up in the recent years (see Fig. 1.2).

The concept of a Janus fluid was firstly envisaged by the French physicist Pierre-Gilles de Gennes, during his Physics Nobel Prize speech in 1991. In that occasion, de Gennes proposed the Janus particle as a colloid with a well-differentiated structure in every hemisphere that could form, in his own words "a skin able to breathe" [11]. This speech was the first time that molecules consisting in two symmetric hemispheres with different composition was called after Janus, the Roman god of duality (see Fig. 1.3).

The insight that de Gennes had in mind arises clearly if we consider the two hemispheres of the particle behaving as solvophilic and solvophobic substances. Provided this amphiphilic character between the two regions, Janus particles might be regarded as the simplest and most elementary case of a surfactant.

Therefore, combining the properties exhibited by these particles (simple geometry, amphiphilic behavior, and surfactant character), we can easily consider the

FIGURE 1.3: Mythological Janus. Commonly represented as a man with two heads looking in opposites directions, he was the god of beginnings, endings, transitions, and duality. A prominent temple within the Forum of Rome was devoted to *Ianus Geminus*, one of the few roman deities without any Greek counterpart. The term "Janus particle" was coined in the nineties by the Nobel Prize winner Pierre-Gilles de Gennes.

Janus spheres as a perfect candidate for fluids systems with peculiar aggregation and clustering properties as relevant as proteins, nanocomposites, and polymers [5].

De Gennes' simile "the skin that is able to breathe" proves to be an intuitive and meaningful allegory, as *the skin* would refer to the adsorption at the layer interface between two fluids, while the *ability to breathe* should refer to the possible diffusion through the layer.

The self-assembly is just one of the mechanism that has recently attracted increasing attention due to the unprecedented improvement in the chemical synthesis and functionalization of such colloidal particles, that allows a precise and reliable control on the aggregation process that was not possible until a few years ago [12]. From a technological point of view, this is very attractive as it paves

the way to a bottom-up design and engineering of nanomaterials alternative to conventional top-down techniques [13].

One popular choice of model describing the typical duality characteristic of the Janus fluid is the Kern–Frenkel model [14]. This model considers a fluid of rigid spheres having their surfaces partitioned into two hemispheres. One of them has a square-well (SW) character, i.e., it attracts other *similar* hemispheres through a SW interaction, thus mimicking the short-range hydrophobic interactions occurring in real Janus fluids. The other part of the surface is assumed to have hard-sphere (HS) interactions with all other hemispheres, i.e., with both like HS as well as SW hemispheres. The HS hemisphere hence models the charged part in the limit of highly screened interactions that is required to have aggregation of the clusters.

Although in the present work only an even distribution between SW and HS surface distributions will be considered (Janus limit), other choices of the coverage, that is the fraction of SW surface with respect to the total one, have been studied within the Kern–Frenkel model [15]. In fact, one of the most attractive features of the general model stems from the fact that it smoothly interpolates between an isotropic HS fluid (zero coverage) and an equally isotropic SW fluid (full coverage)[16, 17].

On the other hand, the behavior of patchy and Janus particles under external fields has received a great deal of attention in the recent years [18, 19]. By applying an external electrical or magnetic field, appropriately synthesized dipolar Janus particles may be made to align orientationally, so as to expose their functionally active hemisphere either all up or all down (See Ref. [19], Secs. 1.4.3.1 and 1.4.3.2, and references therein). By mixing the two species one could have in the laboratory a binary mixture of Janus particles where the functionally active patch points in opposite directions for each species.

While theoretical studies have been keeping up with, and sometimes even anticipated, experimental developments, the complexities of the anisotropic interactions

in patchy colloids have mainly restricted these investigations to numerical simulations, which have revealed interesting specificities in the corresponding phase diagrams.

The aim of this thesis is to contribute to the understanding of the equilibrium properties of Janus fluids by focusing on one-dimensional and three-dimensional structures. This allows us to obtain a description of the thermodynamic and structural spatial correlation quantities. Apart from its interest in modelling laboratory realizations of colloidal chains [9, 10], the results derived in this work can also be useful as a benchmark to test approximate fluid-state theories.

This thesis is organized as follows:
We start with the development of the Janus-rod study in the one-dimensional case in Ch. 2 [20]. The model of amphiphilic Janus particles in three dimensions is presented in Ch. 3 [21]. Then, we develop the study of the phase diagram for this model in Ch. 4 [22]. Finally, an overview of the thesis is presented, with some remarks and conclusions in Ch. 5.
Apart from the main text, five Appendixes has been added at the end of this work, in order to support and give additional background to the topics discussed in the remainder of the thesis.

2

One-dimensional Janus fluids. Exact solution and mapping from the quenched to the annealed system

2.1 Introduction

This work opens with the study of the equilibrium properties of particular Janus fluids constrained in one-dimensional geometry. Some methods developed in the next pages allow us to obtain an exact description of the thermodynamic and spatial correlation quantities.

The remainder of this chapter is organized as follows: Section 2.2 presents the exact equilibrium statistical-mechanical solution of a general m-component mixture with nearest-neighbor interactions where the interaction potential between two adjacent particles α and $\gamma = \alpha \pm 1$ may depend on their ordering (i.e., $\gamma = \alpha - 1$ versus $\gamma = \alpha + 1$). The particularization to a binary mixture (but yet with arbitrary anisotropic pair interactions) is worked out in Sec. 2.3 with expressions for thermodynamic quantities (density, Gibbs free energy, chemical potentials, and internal energy) and structural properties (pair correlation functions in Laplace space) as functions of pressure, temperature, and composition. Those expressions are made more explicit in Sec. 2.4, where the Kern–Frenkel anisotropic interaction potential [14] is considered, the thermodynamic and structural properties being plotted for several representative cases. Moreover, an analysis in Sec. 2.4 of the asymptotic decay of the pair correlation functions shows the absence of a Fisher–Widom transition line (separating a region in the density-temperature plane where the decay is oscillatory from a region where the decay is monotonic) [23]. While the decay is always oscillatory, a structural crossover line exists between a region with a large wavelength from a region with a smaller wavelength. All those results correspond to a mixture of particles with quenched orientation, but in Sec. 2.5 we provide compelling arguments on the mapping of those results onto the case of one-component Janus fluids of particles with flipping orientation (annealed system). Such an equivalence is confirmed in Sec. 2.6 by comparison between the theoretical results for quenched systems and Monte Carlo simulations for annealed systems.

2.2 General (quenched) mixture with anisotropic interactions

2.2.1 The system

Let us consider an N-particle, m-component fluid mixture with number densities $\{\rho_i; i = 1, \ldots, m\}$, so that the total number density is $\rho = \sum_{i=1}^{m} \rho_i$ and the mole

fractions are $x_i = \rho_i/\rho$. The species i any given particle α belongs to is *fixed*, and in this sense the system is said to be *quenched*.

The potential energy function of a particle α (located at $\mathbf{r}_\alpha$) of species i due to the interaction with another particle γ (located at $\mathbf{r}_\gamma$) of species j will be denoted by $\phi_{ij}(\mathbf{r}_\gamma - \mathbf{r}_\alpha)$. According to Newton's third law, $\phi_{ij}(\mathbf{r}_\gamma - \mathbf{r}_\alpha) = \phi_{ji}(\mathbf{r}_\alpha - \mathbf{r}_\gamma)$, i.e., $\phi_{ij}(\mathbf{r}) = \phi_{ji}(-\mathbf{r})$ for all species pairs i, j. On the other hand, the interaction potential is assumed to be *anisotropic* and thus one may have, in general, $\phi_{ij}(\mathbf{r}) \neq \phi_{ji}(\mathbf{r})$ if $i \neq j$. This anisotropic character means that, in general, the potential energy of a particle α due to the action of another particle γ depends not only on the distance $|\mathbf{r}_\gamma - \mathbf{r}_\alpha|$ between both particles but also on the relative orientation of γ with respect to α. We will also assume that $\lim_{\mathbf{r}\to\mathbf{0}} \phi_{ij}(\mathbf{r}) = \infty$ and $\lim_{r\to\infty} \phi_{ij}(\mathbf{r}) = 0$, implying that the particles are impenetrable and the interactions have a finite range.

Now we particularize to a system confined to *one dimension*, so that particles are aligned along an axis of length L. By assuming that the interaction is restricted to nearest neighbors, the total potential energy can be written as

$$\Phi_N(\mathbf{r}_1, \mathbf{r}_2, \ldots, \mathbf{r}_N) = \sum_{\alpha=1}^{N-1} \phi_{i_\alpha, i_{\alpha+1}}(\mathbf{r}_{\alpha+1} - \mathbf{r}_\alpha), \tag{2.1}$$

where $i_\alpha (= 1, 2, \ldots, m)$ denotes the species of particle α and, without loss of generality, we assume that particles $1, 2, \ldots, N$ are ordered from left to right. Therefore, $\phi_{i_\alpha, i_{\alpha+1}}(\mathbf{r}_{\alpha+1} - \mathbf{r}_\alpha) = \phi_{i_\alpha, i_{\alpha+1}}(r_{\alpha,\alpha+1})$, where $r_{\alpha,\alpha+1} \equiv |\mathbf{r}_{\alpha+1} - \mathbf{r}_\alpha|$. The anisotropy of the interaction implies that, in general, $\phi_{ij}(r) \neq \phi_{ji}(r)$. Figure 2.1 shows a sketch of the system in the case of a binary mixture ($m = 2$) of Janus particles (see Sec. 2.3). More in general, one can imagine w different side faces (or "colors") and $m = w(w-1)$ species corresponding to the different ways of ordering pairs of unequal faces. It is also possible to think of an m-component mixture where every particle of a given species has a patch spin vector pointing in one of m possible directions; in the polydisperse limit ($m \to \infty$), the spin vector would point in any arbitrary direction.

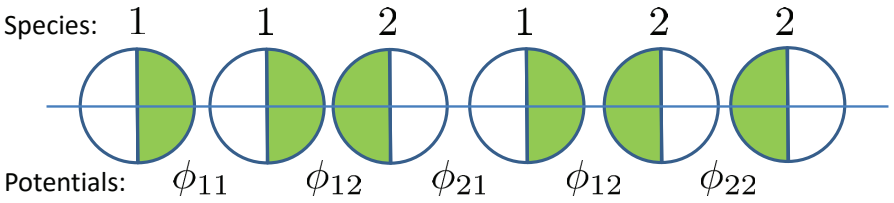

FIGURE 2.1: Sketch of a binary mixture of one-dimensional Janus particles. Particles of species 1 (2) have a white (green) left face and a green (white) right face. Three types of interactions are possible: green–white (ϕ_{11} and ϕ_{22}), green–green (ϕ_{12}), and white–white (ϕ_{21}). Note that, due to invariance under reflection, one must have $\phi_{11}(r) = \phi_{22}(r)$.

2.2.2 Probability densities

Let us now use arguments similar to those conventionally used for isotropic potentials [24, 25, 26, 27, 28, 29] to derive the structural properties of the mixture. Given a reference particle of species i, we focus on those particles to its right and denote by $p_{ij}^{(\ell,+)}(r)dr$ the (conditional) probability that its ℓth right neighbor belongs to species j and is located at a distance between r and $r+dr$. In particular, $p_{ij}^{(1,+)}(r)$ is the right *nearest-neighbor* probability distribution function. Obviously, if $\ell = 0$ one has $p_{ij}^{(0,+)}(r) = \delta_{ij}\delta(r)$. The (conditional) *total* probability density of finding a particle of species j at a distance r to the right of a given particle of species i is

$$p_{ij}^{(+)}(r) \equiv \sum_{\ell=1}^{\infty} p_{ij}^{(\ell,+)}(r). \tag{2.2}$$

In making the upper limit of the summation equal to infinity, we are assuming the thermodynamic limit ($L \to \infty$, $N \to \infty$, $\rho = N/L = \text{constant}$).

Let us consider now a few basic relations. First, since the ℓth right neighbor must be somewhere and belong to any of the species, the normalization condition reads

$$\sum_{j=1}^{m} \int_0^{\infty} dr\, p_{ij}^{(\ell,+)}(r) = 1. \tag{2.3}$$

As before, the infinite upper limit of the integral reflects the thermodynamic limit assumption. An obvious condition is the recurrence relation [27]

$$p_{ij}^{(\ell,+)}(r) = \sum_{k=1}^{m} \int_0^r dr'\, p_{ik}^{(\ell-1,+)}(r') p_{kj}^{(1,+)}(r-r'). \tag{2.4}$$

Equation (2.4) allows one to prove by induction that the normalization condition (2.3) is satisfied by all $p_{ij}^{(\ell,+)}(r)$, provided it is satisfied by $p_{ij}^{(1,+)}(r)$.

Another physical condition is [24, 25, 27]

$$\lim_{r\to\infty} \frac{p_{ij}^{(1,+)}(r)}{p_{ik}^{(1,+)}(r)} = \text{independent of } i. \tag{2.5}$$

This means that the ratio between the two probabilities that the right nearest neighbor of a given reference particle is located at a certain distance r and belongs to species j and k, respectively, becomes asymptotically insensitive to the nature of the reference particle in the limit of large separations. This is a consequence of the fact that the reference particle and its nearest neighbor do not interact if r is beyond the range of $\phi_{ij}(r)$ or $\phi_{ik}(r)$.

In analogy with $p_{ij}^{(\ell,+)}(r)$ and $p_{ij}^{(+)}(r)$, one can introduce the distribution $p_{ij}^{(\ell,-)}(r)$ for neighbors of species j located at a distance r to the left of i, as well as the associated total distribution $p_{ij}^{(-)}(r)$. Obviously, the symmetry relation

$$\rho_i p_{ij}^{(\ell,+)}(r) = \rho_j p_{ji}^{(\ell,-)}(r) \tag{2.6}$$

holds. Even though, in general, $p_{ij}^{(\ell,+)}(r) \neq p_{ij}^{(\ell,-)}(r)$ at a local level, one has

$$\int_0^\infty dr\, p_{ij}^{(\ell,+)}(r) = \int_0^\infty dr\, p_{ij}^{(\ell,-)}(r). \tag{2.7}$$

This implies that, given a reference particle of species i, the probability that its ℓth neighbor (regardless of the distance) belongs to species j is independent of whether the neighbor is located to the right or to the left of the reference particle.

Combination of Eqs. (2.6) and (2.7) yields

$$\rho_i \int_0^\infty dr\, p_{ij}^{(\ell,+)}(r) = \rho_j \int_0^\infty dr\, p_{ji}^{(\ell,+)}(r). \tag{2.8}$$

Because of the symmetry relation (2.6), henceforth we will restrict ourselves to the right probability densities $p_{ij}^{(\ell,+)}(r)$ and $p_{ij}^{(+)}(r)$.

The convolution structure of the integral in Eq. (2.4) suggests the introduction of the Laplace transforms

$$P_{ij}^{(\ell)}(s) \equiv \int_0^\infty dr\, e^{-sr} p_{ij}^{(\ell,+)}(r), \quad P_{ij}(s) \equiv \int_0^\infty dr\, e^{-sr} p_{ij}^{(+)}(r), \tag{2.9}$$

so that Eq. (2.4) becomes

$$P_{ij}^{(\ell)}(s) = \sum_{k=1}^m P_{ik}^{(\ell-1)}(s) P_{kj}^{(1)}(s), \quad \mathsf{P}^{(\ell)}(s) = \left[\mathsf{P}^{(1)}(s)\right]^\ell, \tag{2.10}$$

where $\mathsf{P}^{(\ell)}(s)$ is the $m \times m$ matrix of elements $P_{ij}^{(\ell)}(s)$. Consequently, from Eq. (2.2) we have

$$\mathsf{P}(s) = \mathsf{P}^{(1)}(s) \cdot \left[\mathsf{I} - \mathsf{P}^{(1)}(s)\right]^{-1}, \tag{2.11}$$

where $\mathsf{P}(s)$ is the matrix whose elements are $P_{ij}(s)$ and I is the $m \times m$ identity matrix.

Condition (2.3) for $\ell = 1$ is equivalent to

$$\sum_{j=1}^m P_{ij}^{(1)}(0) = 1 \tag{2.12}$$

for any i, what implies $\det\left[\mathsf{I} - \mathsf{P}^{(1)}(0)\right] = 0$. Thus, the matrix $\mathsf{P}(s)$ is singular at $s = 0$. Also, Eq. (2.8) implies

$$\rho_i P_{ij}^{(\ell)}(0) = \rho_j P_{ji}^{(\ell)}(0). \tag{2.13}$$

As in the case of Eqs. (2.3), the recursion relation (2.10) allows one to prove by induction that Eq. (2.13) is satisfied for all ℓ provided it holds for $\ell = 1$.

2.2.3 Pair correlation function

The probability distribution $p_{ij}^{(+)}(r)$ is related to the pair correlation function $g_{ij}(r)$ (where a particle of species j is supposed to be located at a distance r to the right of a particle of species i) by [24, 27]

$$\rho_j g_{ij}(r) = p_{ij}^{(+)}(r). \tag{2.14}$$

Note that, in general, $g_{ij}(r) \neq g_{ji}(r)$. One can also define an *average* pair correlation function as

$$g(r) = \sum_{i,j} x_i x_j g_{ij}(r). \tag{2.15}$$

In Laplace space, Eq. (2.14) becomes

$$G_{ij}(s) = \frac{1}{\rho_j} P_{ij}(s), \tag{2.16}$$

where $G_{ij}(s)$ is the Laplace transform of $g_{ij}(r)$. If we denote by $H_{ij}(s)$ the Laplace transform of the total correlation function $h_{ij}(r) \equiv g_{ij}(r) - 1$, we have

$$G_{ij}(s) = \frac{1}{s} + H_{ij}(s). \tag{2.17}$$

The values $H_{ij}(0)$ are related to the isothermal compressibility (see below) and must be finite. Theqrefore, the behavior of $G_{ij}(s)$ for small s is

$$G_{ij}(s) = \frac{1}{s} + H_{ij}(0) + \mathcal{O}(s). \tag{2.18}$$

According to Eq. (2.16), this implies

$$\lim_{s \to 0} s P_{ij}(s) = \rho_j. \tag{2.19}$$

This confirms that, as said before, the matrix $\mathsf{P}(s)$ is singular at $s = 0$. Equations (2.5), (2.12), (2.13), and (2.19) are basic constraints on $P_{ij}^{(1)}(s)$ that will be used later on.

2.2.4 Nearest-neighbor distribution. Isothermal-isobaric ensemble

From Eqs. (2.11) and (2.16) we see that the knowledge of the nearest-neighbor distribution functions $\{P_{ij}^{(1)}(s)\}$ suffices to determine the pair correlation functions $\{G_{ij}(s)\}$.

In the isothermal-isobaric ensemble, the N-body probability distribution function in configuration space is proportional to $e^{-\beta pL-\beta\Phi_N(\mathbf{r}_1,\ldots,\mathbf{r}_N)}$, where p is the pressure and $\beta\equiv 1/k_BT$ (k_B and T being the Boltzmann constant and the absolute temperature, respectively) [27]. Therefore, the evaluation of any physical quantity implies integrating over the system size L and over the particle coordinates. Thus, in this ensemble the nearest-neighbor probability distribution function is [25, 27]

$$p_{ij}^{(1,+)}(r)\propto\int_r^\infty dL\,e^{-\beta pL}\int_{r_2}^L dr_3\int_{r_3}^L dr_4\cdots\int_{r_{N-1}}^L dr_N\,e^{-\beta\Phi_N(\mathbf{r}_1,\ldots,\mathbf{r}_N)},\tag{2.20}$$

where, without loss of generality, we have chosen the particles $\alpha=1$ (at $r_1=0$) and $\alpha=2$ (at $r_2=r$) as the canonical nearest-neighbor pair of species i and j, respectively. After taking into account Eq. (2.1), applying periodic boundary conditions, and performing the change of variables $r_\alpha\to\hat{r}_\alpha=r_\alpha-r_{\alpha-1}$ ($\alpha=3,\ldots,N$), one gets [27]

$$p_{ij}^{(1,+)}(r)=x_jK_{ij}e^{-\beta pr-\beta\phi_{ij}(r)},\tag{2.21}$$

where the amplitudes K_{ij} are normalization constants. These m^2 parameters can be determined by application of the consistency conditions (2.5), (2.12), and (2.13). Once determined, the equation of state relating ρ, p, and T is obtained by application of Eq. (2.19).

First, we note that, according to Eq. (2.5), the ratio K_{ij}/K_{ik} does not depend on the index i. In particular, $K_{ij}/K_{ii}=K_{jj}/K_{ji}$, i.e.,

$$K_{ij}K_{ji}=K_{ii}K_{jj}\tag{2.22}$$

for all pairs (i,j). Next, Laplace transformation of Eq. (2.21) yields

$$P_{ij}^{(1)}(s) = x_j K_{ij} \Omega_{ij}(s+\beta p), \tag{2.23}$$

where

$$\Omega_{ij}(s) \equiv \int_0^\infty dr\, e^{-sr} e^{-\beta\phi_{ij}(r)}. \tag{2.24}$$

Note that these functions depend parameterically on temperature. For small s,

$$P_{ij}^{(1)}(s) = x_j K_{ij} \left[\Omega_{ij}(\beta p) + \Omega'_{ij}(\beta p) s + \mathcal{O}(s^2)\right], \tag{2.25}$$

where the prime denotes a derivative with respect to s. Therefore, the normalization condition (2.12) implies

$$\sum_{j=1}^{m} x_j K_{ij} \Omega_{ij}(\beta p) = 1. \tag{2.26}$$

Finally, Eq. (2.13) with $\ell = 1$ gives

$$K_{ij}\Omega_{ij}(\beta p) = K_{ji}\Omega_{ji}(\beta p). \tag{2.27}$$

Equations (2.22), (2.26), and (2.27) give $m(m-1)/2 + m + m(m-1)/2 = m^2$ constraints that allow one to determine the m^2 parameters $\{K_{ij}\}$ in terms of the set of mole fractions $\{x_i\}$, the temperature T, and the pressure p. Then, the equation of state $\rho(T, p, \{x_i\})$ is given by Eq. (2.19). Although the matrix equation (2.19) is in principle equivalent to m^2 scalar equations, it turns out that all of them collapse into a single scalar equation. This consistency test, that will be checked in Sec. 2.3 for the case $m = 2$, is a direct consequence of the exact character of the results presented in this section.

2.3 Binary anisotropic (quenched) mixture

2.3.1 Exact solution

Let us now particularize the general scheme of Sec. 2.2 to the case of a binary mixture ($m = 2$), although the interaction potentials $\phi_{ij}(r)$ will not be specified yet. In that case, Eqs. (2.22), (2.26), and (2.27) become

$$K_{11}K_{22} = K_{12}K_{21}, \tag{2.28a}$$

$$x_1K_{11}\Omega_{11}(\beta p) + x_2K_{12}\Omega_{12}(\beta p) = 1, \quad x_1K_{21}\Omega_{21}(\beta p) + x_2K_{22}\Omega_{22}(\beta p) = 1, \tag{2.28b}$$

$$K_{12}\Omega_{12}(\beta p) = K_{21}\Omega_{21}(\beta p). \tag{2.28c}$$

From Eqs. (2.28b) and (2.28c) it is possible to express K_{11}, K_{22}, and K_{21} in terms of K_{12}:

$$K_{11} = \frac{1 - x_2K_{12}\Omega_{12}(\beta p)}{x_1\Omega_{11}(\beta p)}, \quad K_{22} = \frac{1 - x_1K_{12}\Omega_{12}(\beta p)}{x_2\Omega_{22}(\beta p)}, \quad K_{21} = \frac{\Omega_{12}(\beta p)}{\Omega_{21}(\beta p)}K_{12}. \tag{2.29}$$

Then, insertion of Eqs. (2.29) into Eq. (2.28a) gives a quadratic equation for K_{12} whose physical solution is

$$K_{12} = \frac{2}{\Omega_{12}(\beta p)\left(1 + \sqrt{1 - 4x_1x_2R}\right)}, \quad R \equiv 1 - \frac{\Omega_{11}(\beta p)\Omega_{22}(\beta p)}{\Omega_{12}(\beta p)\Omega_{21}(\beta p)}. \tag{2.30}$$

Once the normalization constants $\{K_{ij}\}$ are known in terms of p, T, x_1, and $x_2 = 1 - x_1$, we can proceed to the determination of the equation of state. First, Eq. (2.11) in the binary case gives

$$P_{11}(s) = \frac{1 - P_{22}^{(1)}(s)}{D(s)} - 1, \quad P_{22}(s) = \frac{1 - P_{11}^{(1)}(s)}{D(s)} - 1, \tag{2.31a}$$

$$P_{12}(s) = \frac{P_{12}^{(1)}(s)}{D(s)}, \quad P_{21}(s) = \frac{P_{21}^{(1)}(s)}{D(s)}, \tag{2.31b}$$

where

$$D(s) \equiv \left[1 - P_{11}^{(1)}(s)\right]\left[1 - P_{22}^{(1)}(s)\right] - P_{12}^{(1)}(s)P_{21}^{(1)}(s) \tag{2.32}$$

is the determinant of $\mathsf{I} - \mathsf{P}^{(1)}(s)$. Using Eqs. (2.25) and (2.28b), one can easily prove that $D(s) = D'(0)s + \mathcal{O}(s^2)$ with

$$\begin{aligned} D'(0) &= -x_1x_2K_{12}K_{21}\left[\Omega'_{12}(\beta p)\Omega_{21}(\beta p) + \Omega_{12}(\beta p)\Omega'_{21}(\beta p)\right] \\ &\quad -x_1^2K_{11}K_{21}\Omega'_{11}(\beta p)\Omega_{21}(\beta p) - x_2^2K_{12}K_{22}\Omega_{12}(\beta p)\Omega'_{22}(\beta p). \end{aligned} \tag{2.33}$$

Application of Eq. (2.19) gives

$$\rho x_1 = \frac{1 - x_2K_{22}\Omega_{22}(\beta p)}{D'(0)} = \frac{x_1K_{21}\Omega_{21}(\beta p)}{D'(0)}, \tag{2.34a}$$

$$\rho x_2 = \frac{1 - x_1K_{11}\Omega_{11}(\beta p)}{D'(0)} = \frac{x_2K_{12}\Omega_{12}(\beta p)}{D'(0)}. \tag{2.34b}$$

Equations (2.28b) and (2.28c) show that, out of the four equalities in Eqs. (2.34a) and (2.34b), only one is new, i.e., $\rho = K_{12}\Omega_{12}(\beta p)/D'(0)$. Therefore, the equation of state is

$$-\frac{1}{\rho(T,p,x_1)} = x_1^2K_{11}\Omega'_{11}(\beta p) + x_2^2K_{22}\Omega'_{22}(\beta p) + x_1x_2\left[K_{12}\Omega'_{12}(\beta p) + K_{21}\Omega'_{21}(\beta p)\right]. \tag{2.35}$$

This closes the solution to the problem (see Appendix A Ec. (A.4)). Given the four interaction potentials $\{\phi_{ij}(r)\}$, the mole fraction x_1, the temperature T, and the pressure p, the normalization constants $\{K_{ij}\}$ are given by Eqs. (2.29) and (2.30), while the number density ρ is given by Eq. (2.35). Then, Eqs. (2.16), (2.23), and (2.31b) provide the pair correlation functions $\{g_{ij}(r)\}$ in Laplace space.

2.3.2 Thermodynamic properties

Since the exact explicit solution of the statistical-mechanical problem relies upon the isothermal-isobaric ensemble, the key thermodynamic quantity is the Gibbs

free energy $\mathcal{G}(T,p,N_1,N_2)$ [27]. Using the thermodynamic relation

$$\frac{N}{\rho}=\left(\frac{\partial\mathcal{G}}{\partial p}\right)_{T,N_1,N_2} \tag{2.36}$$

in combination with Eq. (2.35), and after some algebra, it can be found that:

$$\begin{aligned}\frac{\mathcal{G}(T,p,N_1,N_2)}{Nk_BT} &= x_1\ln\frac{x_1\Lambda_1}{\Omega_{11}}+x_2\ln\frac{x_2\Lambda_2}{\Omega_{22}}-\ln\frac{1+\sqrt{1-4x_1x_2R}}{2\sqrt{1-R}}\\ &\quad+|x_1-x_2|\ln\frac{|x_1-x_2|+\sqrt{1-4x_1x_2R}}{(|x_1-x_2|+1)\sqrt{1-R}},\end{aligned} \tag{2.37}$$

where $\Lambda_i=h/\sqrt{2\pi m_ik_BT}$ is the thermal de Broglie's wavelength of species i (h and m_i being the Planck constant and the mass of a particle of species i, respectively) and henceforth the absence of arguments in functions of s (Ω_{ij}, Ω'_{ij}, ...) means that those functions are evaluated at $s=\beta p$. From Eq. (2.37) one can derive the chemical potential of species i by means of the thermodynamic relation $\mu_i=(\partial\mathcal{G}/\partial N_i)_{T,p,N_{j\neq i}}$ as

$$\begin{aligned}\beta\mu_i(T,p,x_1) &= \ln\frac{x_i\Lambda_i}{\Omega_{ii}}-\ln\frac{1+\sqrt{1-4x_1x_2R}}{2\sqrt{1-R}}\\ &\quad+\mathrm{sgn}\,(2x_i-1)\ln\frac{|x_1-x_2|+\sqrt{1-4x_1x_2R}}{(|x_1-x_2|+1)\sqrt{1-R}},\end{aligned} \tag{2.38}$$

where the sign function is $\mathrm{sgn}(x)=+1$ if $x>0$ and -1 otherwise. Notice that $\mathcal{G}=N_1\mu_1+N_2\mu_2$, as should be.

The internal energy U obeys the thermodynamic relation

$$U=\mathcal{G}-T\left(\frac{\partial\mathcal{G}}{\partial T}\right)_{p,N_1,N_2}-p\left(\frac{\partial\mathcal{G}}{\partial p}\right)_{T,N_1,N_2}. \tag{2.39}$$

If $\mathcal{G}$ is seen as a function of $(\beta,\beta p,N_1,N_2)$ rather than as a function of (T,p,N_1,N_2), it is easy to check that the previous relation is equivalent to $U=(\partial\beta\mathcal{G}/\partial\beta)_{\beta p,N_1,N_2}$. Thus, Eq. (2.37) gives

$$\frac{U(T,p,N_1,N_2)}{N}=\frac{k_BT}{2}+x_1\Upsilon_{11}+x_2\Upsilon_{22}-x_1x_2K_{12}\Omega_{12}\left(\Upsilon_{11}+\Upsilon_{22}-\Upsilon_{12}-\Upsilon_{21}\right), \tag{2.40}$$

where [see Ec. (A.12) in Appendix A]

$$\Upsilon_{ij}(s) \equiv -\frac{\partial \ln \Omega_{ij}(s)}{\partial \beta} = \frac{1}{\Omega_{ij}(s)} \int_0^\infty dr\, e^{-sr} \phi_{ij}(r) e^{-\beta \phi_{ij}(r)}. \tag{2.41}$$

As tests on the exact character of the solution, it is proved in Appendix A that the equation of state (2.35) and the internal energy (2.40) are consistent with standard (virial, compressibility, and energy) routes to derive the thermodynamic quantities from the pair correlation functions [27, 30].

2.4 Quenched Janus particles with Kern–Frenkel interaction

The solution of the one-dimensional statistical-mechanical problem for an arbitrary mixture with anisotropic interactions has been developed in Sec. 2.2. Next, the specialization to binary mixtures has allowed us in Sec. 2.3 to reach more explicit and detailed expressions. Now we go a step forward and particularize to a binary mixture of Janus particles (see Fig. 2.1). The Janus symmetry implies that a particle of species 1 is the specular reflection of a particle of species 2, so that only three interactions need to be fixed: $\phi_{11}(r) = \phi_{22}(r)$ (green–white), $\phi_{12}(r)$ (green–green), and $\phi_{21}(r)$ (white–white). Moreover, we assume the Kern–Frenkel model [14], i.e., the white face acts as a hard sphere (HS) of diameter σ in front of any face (either white or green), while the ("active") green face acts as a square-well (SW) sphere of hard-core diameter σ, range $\lambda\sigma$, and well depth ϵ in front of another green face. Therefore, the precise model is

$$\phi_{11}(r) = \phi_{22}(r) = \phi_{21}(r) = \begin{cases} \infty, & r < \sigma, \\ 0, & r > \sigma, \end{cases} \qquad \phi_{12}(r) = \begin{cases} \infty, & r < \sigma, \\ -\epsilon, & \sigma < r < \lambda\sigma, \\ 0, & r > \lambda\sigma, \end{cases} \tag{2.42}$$

where $\lambda \leq 2$. Therefore,

$$\Omega_{11}(s) = \Omega_{22}(s) = \Omega_{21}(s) = \Omega(s) = \frac{e^{-s}}{s}, \quad \Omega_{12}(s) = (1+\theta)\Omega(s) - \lambda\theta\Omega(\lambda s), \tag{2.43}$$

where we have taken $\sigma = 1$ and the quantity $\theta \equiv e^{\beta\epsilon} - 1$ embodies all the dependence on temperature.

2.4.1 Thermodynamic properties

Despite the simplicity of Eq. (2.43), the equation of state (2.35) gives ρ as an explicit function of βp and β but cannot be analytically inverted to express βp as a function of ρ and β. Actually, Eq. (2.35) can be seen as a transcendental equation for $\beta p(\rho, \beta)$ that needs to be solved numerically. On the other hand, by inserting the virial expansion

$$\beta p(\rho, T) = \rho + B_2(T)\rho^2 + B_3(T)\rho^3 + B_4(T)\rho^4 + \cdots \tag{2.44}$$

into Eq. (2.35) and equating terms of the same order in both sides, one can easily obtain the virial coefficients $B_n(T)$ sequentially. In particular, the second, third, and fourth coefficients are

$$B_2(T) = 1 - x_1 x_2(\lambda - 1)\theta, \quad B_3(T) = 1 - x_1 x_2(\lambda - 1)\theta\left[3 - \lambda - (\lambda - 1)\theta\right], \tag{2.45a}$$

$$\begin{aligned} B_4(T) &= 1 - x_1 x_2 \frac{\lambda - 1}{2}\theta\{13 - 8\lambda + \lambda^2 - 3(\lambda - 1)\theta[3 - \lambda - x_1 x_2(\lambda - 1) \\ &\quad + 2(\lambda - 1)^2\theta^2 1 + x_1 x_2)\}. \end{aligned} \tag{2.45b}$$

The second virial coefficient is negative, implying a prevalence of the attraction between green–green faces in the low-density regime, if the temperature is smaller than a certain Boyle temperature T_B, i.e., $T^* \equiv k_B T/\epsilon < T_B^* = 1/\ln[1 + 1/x_1 x_2(\lambda - 1)]$. At exactly $T^* = T_B^*$, $B_2 = 0$ but $B_3(T_B) = 1/x_1 x_2 - (2 - \lambda) > 0$, so that $\beta p/\rho$ is an increasing function of ρ at $T^* = T_B^*$.

It is instructive to consider the high-temperature and low-temperature limits. The results are

$$\beta p(\rho,T)=\frac{\rho}{1-\rho}-\frac{\rho^2}{(1-\rho)^2}e^{-(\lambda-1)\rho/(1-\rho)}x_1x_2(\lambda-1)\beta\epsilon+\mathcal{O}(\beta^2), \tag{2.46a}$$

$$\lim_{T^*\to 0}\frac{1}{\rho}=\frac{1+\beta p}{\beta p}-\min(x_1,x_2)\frac{\lambda-1}{e^{(\lambda-1)\beta p}-1}. \tag{2.46b}$$

Equation (2.46a) displays the first high-temperature correction to the equation of state of the HS Tonks gas [31] due to the SW nature of the interaction $\phi_{12}(r)$. On the other hand, Eq. (2.46b) shows that in the opposite zero-temperature limit the equation of state is far from trivial and cannot be analytically inverted to express βp as a function of ρ.

As for the excess internal energy per particle $u_{\text{ex}}=U/N-k_BT/2$, Eq. (2.40) yields

$$\frac{u_{\text{ex}}}{\epsilon}=-x_1x_2K_{12}(1+\theta)\frac{e^{-\beta p}-e^{-\lambda\beta p}}{\beta p}. \tag{2.47}$$

In the limit of low densities,

$$\frac{u_{\text{ex}}(\rho,T)}{\epsilon}=u_2(T)\rho+u_3(T)\rho^2+u_4(T)\rho^3+\cdots, \tag{2.48}$$

where

$$u_2(T)=-x_1x_2(\lambda-1)e^{\beta\epsilon},\quad u_3(T)=-x_1x_2\frac{\lambda-1}{2}e^{\beta\epsilon}\left[3-\lambda-2(\lambda-1)\theta\right], \tag{2.49a}$$

$$u_4(T)=-x_1x_2\frac{\lambda-1}{6}e^{\beta\epsilon}\{13-8\lambda+\lambda^2-6(\lambda-1)\theta[3-\lambda-x_1x_2(\lambda-1)]. \tag{2.49b}$$

$$+6(\lambda-1)^2\theta^2(1+x_1x_2)\}. \tag{2.49c}$$

The curvature of $u_{\text{ex}}(\rho,T)/\epsilon$ at $\rho=0$ is dictated by the sign of the coefficient $u_3(T)$. Thus, $u_{\text{ex}}(\rho,T)/\epsilon$ is concave (convex) at $\rho=0$ if $T^*<T_u^*$ ($T^*>T_u^*$), where $T_u^*=1/\ln[(\lambda+1)/2(\lambda-1)]>T_B^*$. As before, it is instructive to analyze

the high-temperature and low-temperature limits. The results are

$$\lim_{T^*\to\infty} \frac{u_{\text{ex}}(\rho,T)}{\epsilon} = -x_1x_2[1-e^{-(\lambda-1)\rho/(1-\rho)}], \tag{2.50a}$$

$$\lim_{T^*\to 0} \frac{u_{\text{ex}}(\rho,T)}{\epsilon} = -\min(x_1,x_2). \tag{2.50b}$$

Equation (2.50a) shows that $\lim_{T^*\to\infty} u_{\text{ex}}(\rho,T)/\epsilon$ is a non-trivial finite limit, even though $\lim_{T^*\to\infty} u_{\text{ex}}(\rho,T)/k_BT = 0$. In what concerns Eq. (2.50b), it has a simple interpretation. Suppose that $N_1 \leq N_2$. At zero temperature and any finite density, the free energy is minimized by minimizing the internal energy and this corresponds to configurations of N_1 pairs of the type 1–2 plus $N_2 - N_1$ particles of species 2. The total internal energy is then $U = -N_1/\epsilon$, what implies $u_{\text{ex}}/\epsilon = -x_1$.

It is interesting to remark that the limits $\rho \to 0$ and $T^* \to 0$ do not commute. While $\lim_{\rho\to 0} \beta p(\rho,T)/\rho = 1$ and $\lim_{\rho\to 0} u_{\text{ex}}(\rho,T)/\epsilon = 0$ at any *non-zero* temperature, Eqs. (2.46b) and (2.50b) imply that $\lim_{\rho\to 0}\lim_{T^*\to 0} \beta p(\rho,T)/\rho = 1 - \min(x_1,x_2)$ and $\lim_{\rho\to 0}\lim_{T^*\to 0} u_{\text{ex}}(\rho,T)/\epsilon = -\min(x_1,x_2)$. Notice also that Eqs. (2.44)–(2.50b) are consistent with the exact thermodynamic relation [27]

$$\rho^2 \left(\frac{\partial u_{\text{ex}}}{\partial \rho}\right)_{\beta,x_1} = \left(\frac{\partial \beta p}{\partial \beta}\right)_{\rho,x_1}. \tag{2.51}$$

As an illustration, Fig. 2.2 shows $\beta p/\rho$ and u_{ex}/ϵ versus ρ at temperatures $T^* = 0, 0.1, 0.2, 0.5, 1, \infty$ for an equimolar mixture ($x_1 = x_2 = \frac{1}{2}$) with $\lambda = 1.2$. For such a system, $T_B^* = 0.328$ and $T_u^* = 0.587$. We observe that, as expected, the isotherms are "sandwiched" between the curves corresponding to the limits $T^* = 0$ and $T^* \to \infty$. It is quite apparent that the compressibility factor $\beta p/\rho$ at $T^* = 0.1$ is practically indistinguishable from the one corresponding to $T^* = 0$, except for very small densities. Analogously, the isotherm $T^* = 1$ in Fig. 2.2(a) is very close to that of infinite temperature. Thus, in contrast to what happens in the case of the conventional SW fluid [27], the influence of temperature on the equation of state is relatively moderate. On the other hand, temperature does

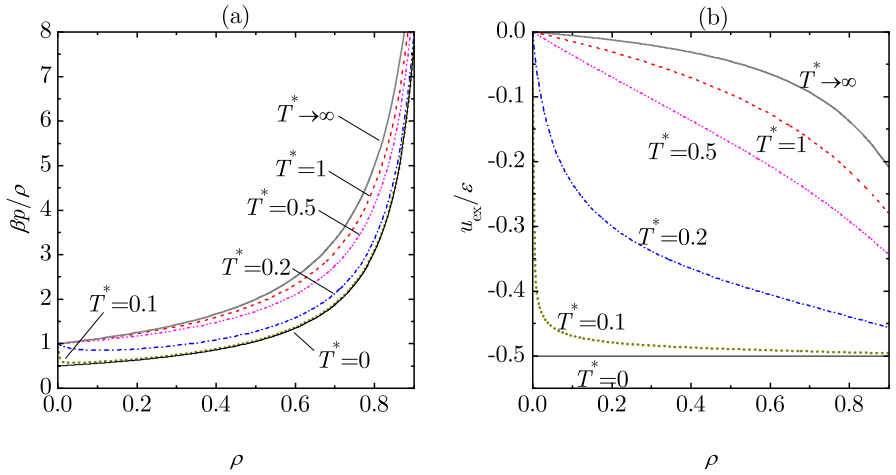

FIGURE 2.2: Plot of (a) the compressibility factor $\beta p/\rho$ and (b) the excess internal energy per particle u_{ex}/ϵ versus density at temperatures $T^* = 0, 0.1, 0.2, 0.5, 1, \infty$ for an equimolar mixture ($x_1 = x_2 = \frac{1}{2}$) with $\lambda = 1.2$.

play a relevant role on the excess internal energy, as Fig. 2.2(b) shows. A clear transition from concavity to convexity can be observed as temperature increases. In the case of $T^* = 0.5 < T_u^*$, although the curve is slightly concave at $\rho = 0$, an inflection point is present at $\rho = 0.293$, the curve becoming convex thereafter.

2.4.2 Structural properties

According to Eqs. (2.23) and (2.32), the determinant $D(s)$ becomes

$$D(s) = 1 - a\Omega(s+\beta p) - b\Omega(s+\beta p)\left[\Omega(s+\beta p) - \lambda\Omega(\lambda(s+\beta p))\right], \tag{2.52}$$

where we have called

$$a \equiv x_1 K_{11} + x_2 K_{22}, \quad b \equiv x_1 x_2 K_{11} K_{22} \theta. \tag{2.53}$$

Moreover, from Eqs. (2.16), (2.31a), and (2.31b), we find the following expressions for the pair correlation functions in Laplace space:

$$G_{11}(s) = \frac{K_{11}}{\rho}\Psi^{(1,0)}(s) + \frac{x_2 K_{11} K_{22}\theta}{\rho}\left[\Psi^{(2,0)}(s) - \lambda\Psi^{(1,1)}(s)\right], \tag{2.54a}$$

$$G_{22}(s) = \frac{K_{22}}{\rho}\Psi^{(1,0)}(s) + \frac{x_1 K_{11} K_{22}\theta}{\rho}\left[\Psi^{(2,0)}(s) - \lambda\Psi^{(1,1)}(s)\right], \tag{2.54b}$$

$$G_{12}(s) = \frac{K_{12}(1+\theta)}{\rho}\Psi^{(1,0)}(s) - \frac{K_{12}\lambda\theta}{\rho}\Psi^{(0,1)}(s), \tag{2.54c}$$

$$G_{21}(s) = \frac{K_{21}}{\rho}\Psi^{(1,0)}(s), \tag{2.54d}$$

where

$$\Psi^{(k_1,k_2)}(s) \equiv \frac{[\Omega(s+\beta p)]^{k_1}\,[\Omega(\lambda(s+\beta p))]^{k_2}}{D(s)}. \tag{2.55}$$

The pair correlation functions $g_{ij}(r)$ in real space are given by expressions analogous to Eq. (2.54a)–(2.54d) with the replacement $\Psi^{(k_1,k_2)}(s) \to \psi^{(k_1,k_2)}(r)$, where the function $\psi^{(k_1,k_2)}(r) = \mathcal{L}^{-1}\left[\Psi^{(k_1,k_2)}(s)\right]$ is the inverse Laplace transform of $\Psi^{(k_1,k_2)}(s)$. In order to find practical representations of $g_{ij}(r)$, let us use the mathematical identity

$$[1 - ax - bx(x-y)]^{-1} = \sum_{n=0}^{\infty}\sum_{\ell=0}^{n} C_{n,\ell}\, x^n y^\ell \tag{2.56}$$

where

$$C_{n,\ell} \equiv \frac{a^{n-\ell}(-b)^\ell}{\ell!}\sum_{q=0}^{[(n-\ell)/2]}\frac{(n-q)!}{q!(n-\ell-2q)!}(b/a^2)^q, \tag{2.57}$$

$[(n-\ell)/2]$ denoting the integer part of $(n-\ell)/2$. Equation (2.52) shows that $D(s)$ has the structure $1 - ax - bx(x-y)$ with $x = \Omega(s+\beta p)$ and $y = \lambda\Omega(\lambda(s+\beta p))$. Therefore,

$$\begin{aligned}\Psi^{(k_1,k_2)}(s) &= \sum_{n=0}^{\infty}\sum_{\ell=0}^{n} C_{n,\ell}\lambda^\ell\,[\Omega(s+\beta p)]^{n+k_1}\,[\Omega(\lambda(s+\beta p))]^{\ell+k_2} \\ &= \frac{1}{\lambda^{k_2}}\sum_{n=0}^{\infty}\sum_{\ell=0}^{n} C_{n,\ell}\frac{e^{-(n+k_1+\lambda\ell+\lambda k_2)(s+\beta p)}}{(s+\beta p)^{n+\ell+k_1+k_2}}.\end{aligned} \tag{2.58}$$

Then, taking into account the Laplace property

$$\mathcal{L}^{-1}\left[\frac{e^{-n(s+\beta p)}}{(s+\beta p)^{\ell+1}}\right]=\frac{(r-n)^{\ell}}{\ell!}e^{-\beta pr}\Theta(r-n), \tag{2.59}$$

where $\Theta(x)$ is the Heaviside step function, we finally have

$$\begin{aligned}\psi^{(k_1,k_2)}(r) &= \frac{e^{-\beta pr}}{\lambda^{k_2}}\sum_{n=0}^{\infty}\sum_{\ell=0}^{n}C_{n,\ell}\frac{(r-n-k_1-\lambda\ell-\lambda k_2)^{n+\ell+k_1+k_2-1}}{(n+\ell+k_1+k_2-1)!}\\ &\quad\times\Theta(r-n-k_1-\lambda\ell-\lambda k_2).\end{aligned} \tag{2.60}$$

Although in principle the summation in Eq. (2.60) extends to $n\to\infty$, truncation at $n=n_{\max}$ allows one to obtain $\psi^{(k_1,k_2)}(r)$ in the interval $1\le r\le n_{\max}+1+k_1+\lambda k_2$. In view of Eqs. (2.54a)–(2.54d), this implies that truncation at $n=n_{\max}$ guarantees the exact evaluation of $g_{ij}(r)$ up to $r=n_{\max}+2$.

As an illustration, Fig. 2.3 considers the same system as in Fig. 2.2, i.e., an equimolar mixture ($x_1=x_2=\frac{1}{2}$) with $\lambda=1.2$, and displays the pair correlation functions $g_{11}(r)=g_{22}(r)$, $g_{21}(r)$, and $g_{12}(r)$, as well as the average function $g(r)=\frac{1}{2}g_{11}(r)+\frac{1}{4}g_{12}(r)+\frac{1}{4}g_{21}(r)$ [see Eq. (2.15)] for the representative density $\rho=0.7$ and the same temperatures as in Fig. 2.2. Clear changes in the structural properties are apparent as the temperature changes. In the limit $T^*\to\infty$, all the correlation functions are identical and coincide with that of the pure HS system. In fact, at temperature $T^*=1$ the deviations from the common HS function are rather small, except for the discontinuity of $g_{12}(r)$ and $g(r)$ at $r=\lambda$. The deviations from the HS pair correlation function become much more important as temperature decreases to $T^*=0.5$ and then to $T^*=0.2$. At $T^*=0.1$ the correlation functions are hardly distinguishable from those corresponding to $T^*=0$ and exhibit features characteristic of the expected "dimer" configurations (1–2)—(1–2)—(1–2)—$\cdots$, where the two particles of a dimer (1–2) are separated a distance between $r=1$ and $r=\lambda$, while the distance between two adjacent dimers is more flexible, its typical value depending on density. Thus, we observe that, at $T^*=0$, $g_{11}(r)$ and $g_{22}(r)$ vanish for $1\le r\le 2$ and $g_{12}(r)$ vanish for $\lambda<r<3$.

The special sticky-hard-sphere limit [21, 22, 27, 32], where $T^*\to 0$ and $\lambda\to 1$

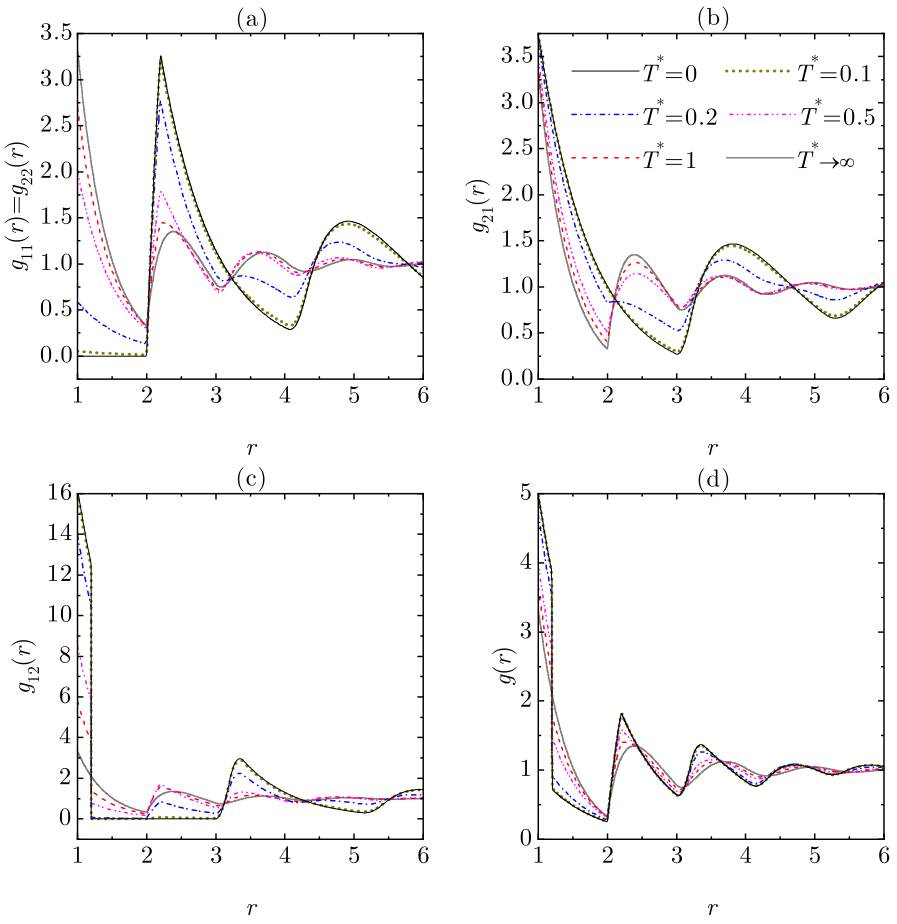

FIGURE 2.3: Plot of (a) $g_{11}(r) = g_{22}(r)$, (b) $g_{21}(r)$, (c) $g_{12}(r)$, and (d) $g(r)$ at density $\rho = 0.7$ and temperatures $T^* = 0, 0.1, 0.2, 0.5, 1, \infty$ for an equimolar mixture ($x_1 = x_2 = \frac{1}{2}$) with $\lambda = 1.2$.

with a constant *stickiness* parameter $\tau^{-1} \equiv (\lambda - 1)\theta$, is worked out in Appendix B.

2.4.3 Asymptotic decay of correlations. Structural crossover

The representation of $g_{ij}(r)$ in terms of the auxiliary functions $\psi^{(k_1,k_2)}(r)$ [see Eqs. (2.54a)–(2.54d) and (2.60)] is not practical for asymptotically large values of r because of the many terms involved. In that case, the asymptotic behaviors of the total correlation functions $h_{ij}(r) = g_{ij}(r) - 1$ and of the average function $h(r) = g(r) - 1 = \sum_{i,j} x_i x_j h_{ij}(r)$ are of the form [33]

$$h_{ij}(r) \sim A_{ij} e^{-\kappa r} \cos(\omega r + \varphi_{ij}), \quad h(r) \sim A e^{-\kappa r} \cos(\omega r + \varphi), \tag{2.61}$$

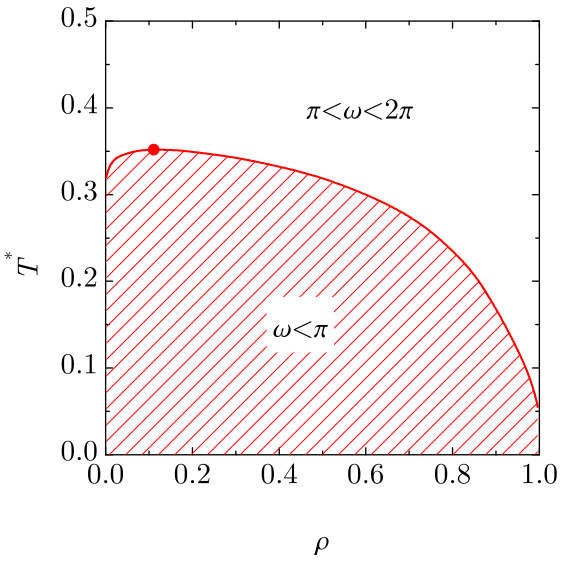

FIGURE 2.4: Phase diagram for an equimolar mixture ($x_1 = x_2 = \frac{1}{2}$) with $\lambda = 1.2$. In the states above the crossover line, the pair correlation functions present an asymptotic oscillatory behavior with a wavelength $2\pi/\omega$ comprised between the values 1 and 2 (i.e., a spatial frequency $\pi < \omega < 2\pi$), while the wavelength $2\pi/\omega$ is larger than 2 (i.e., $\omega < \pi$) for states below the curve. The circle represents the "critical" point $\rho_c = 0.1105$, $T_c^* = 0.3517$. When crossing the curve, the value of ω experiences a discontinuous change.

where $s_\pm = -\kappa \pm \mathrm{i}\omega$ are the conjugate pair of zeroes of $D(s)$ with a real part closest to the origin. Setting $D(s_\pm) = 0$ in Eq. (2.52) yields the two coupled equations

$$\begin{aligned} e^{-\xi}(\xi\cos\omega + \omega\sin\omega) &= -a - \frac{b}{\xi^2+\omega^2}[e^{\lambda\xi}(\xi\cos\lambda\omega + \omega\sin\lambda\omega) \\ &\quad -e^{\xi}(\xi\cos\omega + \omega\sin\omega)], \qquad (2.62a) \\ e^{-\xi}(\xi\sin\omega - \omega\cos\omega) &= \frac{b}{\xi^2+\omega^2}[e^{\lambda\xi}(\xi\sin\lambda\omega - \omega\cos\lambda\omega) \\ &\quad -e^{\xi}(\xi\sin\omega - \omega\cos\omega)], \qquad (2.62b) \end{aligned}$$

where $\xi \equiv \kappa - \beta p$.

An analysis of the numerical solutions of the set of Eqs. (2.62a) and (2.62a) shows that the zeroes of $D(s)$ with a real part closest to the origin are always complex numbers (i.e., $\omega \neq 0$). Therefore, no Fisher–Widom line [23] separating the oscillatory and monotonic large-distance behaviors exists in a one-dimensional Janus fluid, in contrast to what happens in the case of one-dimensional isotropic fluids [23, 29, 34]. Therefore, the restriction of attractive interactions to only the

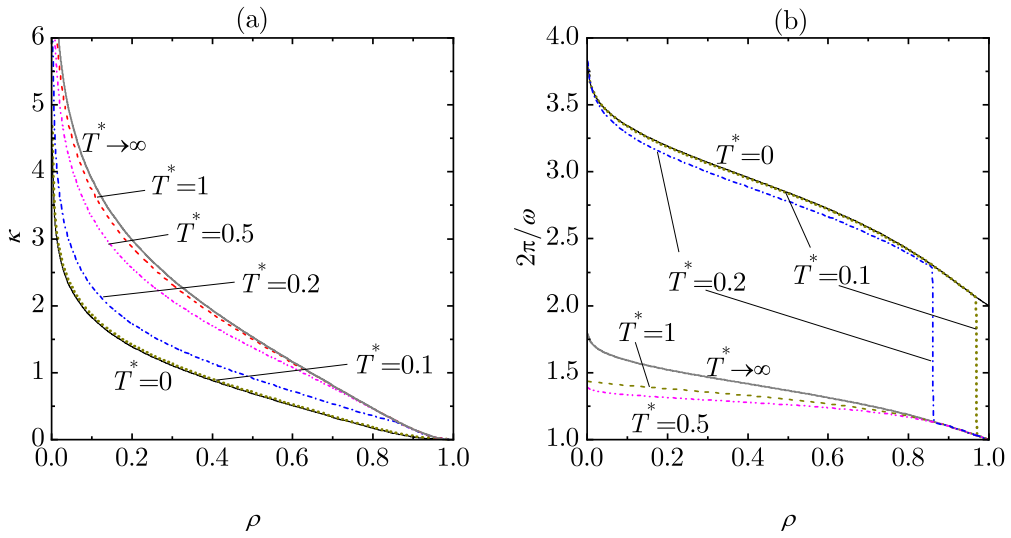

FIGURE 2.5: Plot of (a) the damping coefficient κ and (b) the wavelength $2\pi/\omega$ versus density at temperatures $T^* = 0, 0.1, 0.2, 0.5, 1, \infty$ for an equimolar mixture ($x_1 = x_2 = \frac{1}{2}$) with $\lambda = 1.2$.

1–2 pair frustrates the possibility of monotonic decay of correlations, even at low temperature.

However, a structural crossover line can be identified on the plane T^* vs ρ separating (typically high-temperature) states where the wavelength $2\pi/\omega$ of the oscillations lies between the values 1 and 2 from (typically low-temperature) states with a larger wavelength. This crossover transition is reminiscent of the one observed in binary HS mixtures [35, 36, 37].

The structural crossover line, and the associated phase diagram, are shown in Fig. 2.4 for an equimolar mixture ($x_1 = x_2 = \frac{1}{2}$) with $\lambda = 1.2$. The line has a maximum at a "critical" point $\rho_c = 0.1105$, $T_c^* = 0.3517$, so that if $T^* > T_c^*$ the asymptotic oscillatory behavior corresponds to $1 < 2\pi/\omega < 2$. However, if $0.32 < T^* < T_c^*$, there exists a window of densities $\rho_-(T^*) < \rho < \rho_+(T^*)$ around ρ_c where the oscillations have a wavelength $2\pi/\omega > 2$. Such a window extends to $0 < \rho < \rho_+(T^*)$ if $T^* < 0.32$. Upon crossing the line, the transition from shorter to longer wavelength (or vice versa) is discontinuous.

Figure 2.5 shows κ and ω versus ρ at temperatures $T^* = 0, 0.1, 0.2, 0.5, 1, \infty$ for an equimolar mixture ($x_1 = x_2 = \frac{1}{2}$) with $\lambda = 1.2$. As density increases

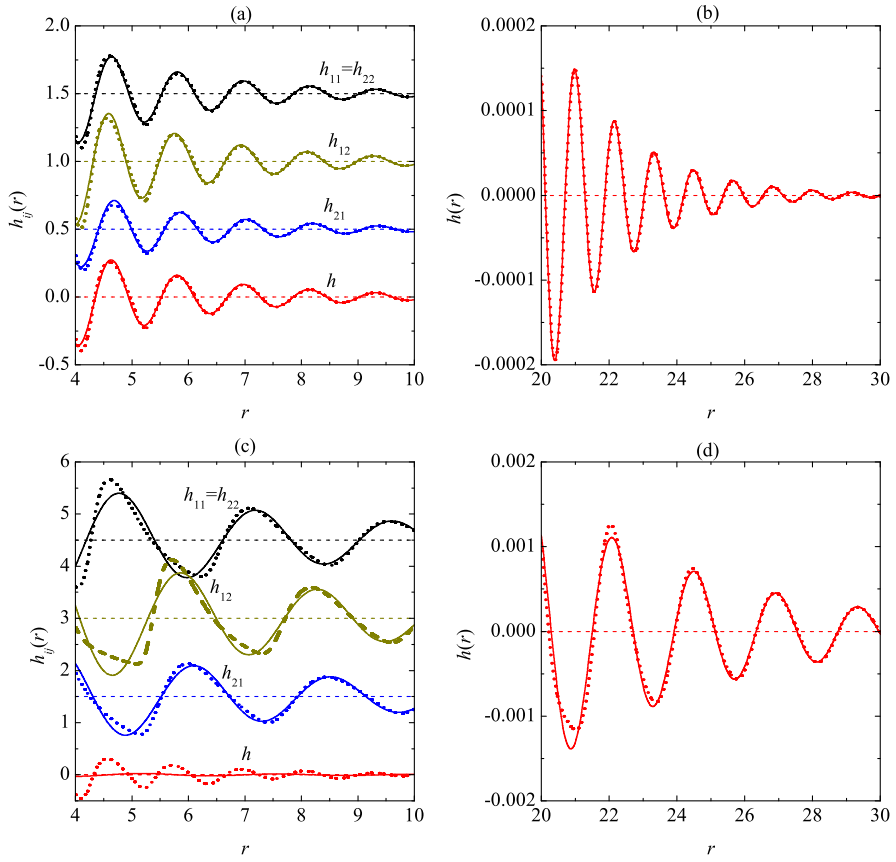

FIGURE 2.6: Plot of of the total correlation functions $h_{ij}(r)$ and $h(r)$ for an equimolar mixture ($x_1 = x_2 = \frac{1}{2}$) with $\lambda = 1.2$ at $\rho = 0.8$. Panels (a) and (b) correspond to $T^* = 0.5$, while panels (c) and (d) correspond to $T^* = 0.1$. The dotted curves represent the full functions, while the solid lines represent the asymptotic behavior (2.61). Note that in panels (a) and (c) the curves representing h_{ij} have been shifted vertically for better clarity.

and/or temperature decreases, the damping coefficient κ and the wavelength $2\pi/\omega$ decrease. In analogy with Fig. 2.2(a), the curves corresponding to $T^* = 0.1$ are hardly distinguishable from those corresponding to $T^* = 0$, except for the discontinuous change of ω at $\rho_+(T^* = 0.1) = 0.969$. In the case of $T^* = 0.2$ the transition takes place at $\rho_+(T^* = 0.2) = 0.860$.

The amplitudes (A_{ij}, A) and phases (φ_{ij}, φ) in Eq. (2.61) are obtained by application of the residue theorem as

$$A_{ij} = 2|\mathcal{R}_{ij}|, \quad \varphi_{ij} = \arg(\mathcal{R}_{ij}), \quad A = 2|\mathcal{R}|, \quad \varphi = \arg(\mathcal{R}), \tag{2.63}$$

where, according to Eqs. (2.54a)–(2.54d),

$$\mathcal{R}_{11} = \frac{1 - x_2 K_{22}\Omega(s_\pm + \beta p)}{\rho x_1 D'(s_\pm)}, \quad \mathcal{R}_{22} = \frac{1 - x_1 K_{11}\Omega(s_\pm + \beta p)}{\rho x_2 D'(s_\pm)}, \tag{2.64a}$$

$$\mathcal{R}_{12} = \frac{K_{12}\Omega_{12}(s_\pm + \beta p)}{\rho D'(s_\pm)}, \quad \mathcal{R}_{21} = \frac{K_{21}\Omega(s_\pm + \beta p)}{\rho D'(s_\pm)}, \quad \mathcal{R} = \sum_{i,j} x_i x_j \mathcal{R}_{ij}. \tag{2.64b}$$

From a practical point of view, the asymptotic behavior of Eq. (2.61) is, in general, already very accurate at not too large distances. Figure 2.6 displays the partial functions $h_{ij}(r)$ and the average function $h(r)$, again for an equimolar mixture ($x_1 = x_2 = \frac{1}{2}$) with $\lambda = 1.2$. Two representative states have been chosen, one above the transition line of Fig. 2.4, namely $(\rho, T^*) = (0.8, 0.5)$, and the other one below the line, namely $(\rho, T^*) = (0.8, 0.1)$. The associated values of the damping coefficient and the wavelength are $(\kappa, 2\pi/\omega) = (0.460, 1.168)$ and $(\kappa, 2\pi/\omega) = (0.185, 2.417)$, respectively. We observe from Fig. 2.6(a) that the oscillations of $h_{11}(r) = h_{22}(r)$, $h_{12}(r)$, and $h_{21}(r)$ are almost on phase, so that the average correlation function $h(r)$ is qualitatively very similar to the partial functions $h_{ij}(r)$. Figure 2.6(b) clearly shows that $h(r)$ asymptotically oscillates with a wavelength smaller than 2. The scenario changes at the state $(\rho, T^*) = (0.8, 0.1)$. As shown by Fig. 2.6(c), $h_{12}(r)$ and $h_{21}(r)$ are rather on phase, but they are dephased almost half a wavelength with respect to $h_{11}(r) = h_{22}(r)$. As a consequence, a large amount of cancellation takes place when computing the average correlation function $h(r)$, its oscillations in the range $4 < r < 10$ being about twice as frequent as those of the partial contributions $h_{ij}(r)$. In fact, it can be seen from Fig. 2.6(c) that the asymptotic function $h(r)$ corresponding to $(\kappa, 2\pi/\omega) = (0.185, 2.417)$ is not accurate at all in the range $4 < r < 10$ and one needs to move to much larger distances to match the asymptotic form, as Fig. 2.6(d) shows. It is interesting to note that the behavior of $h(r)$ in the range $4 < r < 10$ is very well captured (not shown) by the asymptotic form associated with the "competing" (subleading) root $(\kappa', 2\pi/\omega') = (0.435, 1.159)$.

To understand the physical origin of the crossover transition, consider the extreme cases $T^* \gg 1$ and $T^* \ll 1$. In the first case, the asymptotic behavior of

the correlation functions $h_{ij}(r)$ is qualitatively similar to that of a hard-rod one-component system, with oscillation wavelengths between the hard-core diameter and twice that value. On the other hand, dimer-like configurations (1–2)—(1–2)—(1–2)—$\cdots$ prevail if $T^* \ll 1$, resulting in larger wavelengths.

2.5 Orientationally constrained Janus models. Mapping of the quenched (binary-mixture) system onto the annealed (one-component) system

In Janus models of one-dimensional rods, only two orientations of the active face are possible, as exemplified in Fig. 2.1. However, in the case of particles in two and three dimensions, even if confined in a one-dimensional channel, the unit "spin" vector $\mathbf{s}_\alpha$ characterizing the orientation of the active face of particle α can point in any direction. In such a case, a mixture version of the model requires considering a polydisperse system with an infinite number of species, each one characterized by a different frozen spin vector.

On the other hand, one can also assume two- or three-dimensional models where only two mutually anti-parallel (up–down) spin vectors $\mathbf{s}_+ = -\mathbf{s}_-$ are allowed (see Chaps. 3 and 4). In this special class of orientationally constrained Janus models, the system can be one- or two-component. In the former case (annealed system), the spin $\mathbf{s}_\alpha$ of any particle α is not fixed and can flip from $\mathbf{s}_\alpha = \mathbf{s}_+$ to $\mathbf{s}_\alpha = \mathbf{s}_-$, and vice versa. In contrast, in the two-component (quenched) system the spins are frozen, so that $\mathbf{s}_\alpha$ is fixed to $\mathbf{s}_\alpha = \mathbf{s}_+$ if particle α belongs to species $i = 1$, while it is fixed to $\mathbf{s}_\alpha = \mathbf{s}_-$ if particle α belongs to species $i = 2$. The fraction of particles having spin $\mathbf{s}_+$ *fluctuates* around $\frac{1}{2}$ in the one-component (annealed) case, while it is strictly *fixed* to the mole fraction $x_1 = \frac{1}{2}$ in the parallel two-component (quenched) case. More in general, in a *biased* one-component system, the fraction of particles with spin $\mathbf{s}_+$ may fluctuate around a value $x_1 \neq \frac{1}{2}$. While

the arguments of this section can be extended to that more general scenario, here we focus for simplicity on the unbiased case ($x_1 = \frac{1}{2}$).

The total number of possible spin configurations is 2^N in the annealed system and $\binom{N}{N_1} \simeq \sqrt{2/\pi N}2^N$ in the quenched system with $N_1 = N/2$. The interesting question is, does there exist a relationship between the physical properties of both systems? The aim of this section is to argue that the pair correlation functions of the annealed one-component system coincide with those of the quenched binary mixture in the thermodynamic limit.

First, we describe the annealed and quenched versions of the system in any dimensionality.

2.5.1 Annealed system

In this case, all the particles are identical and the specification of a microstate (in configuration space) requires, apart from the positions $\mathbf{r}^N \equiv \{\mathbf{r}_1, \ldots, \mathbf{r}_N\}$ of the N particles, the spins $\mathbf{s}^N \equiv \{\mathbf{s}_1, \ldots, \mathbf{s}_N\}$. Thus, a given microstate is specified as $\varsigma^N \equiv \{\varsigma_1, \ldots, \varsigma_N\}$ with the short-hand notation $\varsigma_\alpha \equiv \{\mathbf{s}_\alpha, \mathbf{r}_\alpha\}$. The total potential energy is

$$\Phi_N^{\text{ann}}(\varsigma^N) = \sum_{\alpha=1}^{N-1} \sum_{\gamma=\alpha+1}^{N} \phi(\varsigma_\alpha, \varsigma_\gamma), \quad \phi(\varsigma_\alpha, \varsigma_\gamma) \equiv \phi(\mathbf{s}_\alpha, \mathbf{r}_\alpha; \mathbf{s}_\gamma, \mathbf{r}_\gamma) = \phi_{\mathbf{s}_\alpha, \mathbf{s}_\gamma}(\mathbf{r}_{\gamma\alpha}), \quad (2.65)$$

where the superscript "ann" stands for "annealed." The interaction potential $\phi(\varsigma_\alpha, \varsigma_\gamma)$ between two particles α and γ depends not only on their positions $\mathbf{r}_\alpha$ and $\mathbf{r}_\gamma$ (actually on the relative vector $\mathbf{r}_{\gamma\alpha} \equiv \mathbf{r}_\gamma - \mathbf{r}_\alpha$) but also on their spins $\mathbf{s}_\alpha$ and $\mathbf{s}_\gamma$

In the canonical ensemble, the probability density of the microstate ς^N is [27, 30]

$$\rho_N^{\text{ann}}(\varsigma^N) = \frac{\exp\left[-\beta\Phi_N^{\text{ann}}(\varsigma^N)\right]}{Q_N^{\text{ann}}}, \quad Q_N^{\text{ann}} = \int d\varsigma^N \exp\left[-\beta\Phi_N^{\text{ann}}(\varsigma^N)\right], \quad (2.66)$$

where $Q_N^{\rm ann}$ is the configuration integral and the notations $\int d\varsigma^N \equiv \int d\varsigma_1 \cdots \int d\varsigma_N$ and $\int d\varsigma_\alpha \equiv \sum_{\mathbf{s}_\alpha=\mathbf{s}_\pm} \int d\mathbf{r}_\alpha$ have been introduced. The pair correlation function is defined as

$$\begin{aligned} g^{\rm ann}(\varsigma_a,\varsigma_b) &= \frac{1}{(\rho/2)^2}\left\langle \sum_{\alpha\neq\gamma} \delta(\varsigma_a-\varsigma_\alpha)\delta(\varsigma_b-\varsigma_\gamma)\right\rangle_{\rho_N^{\rm ann}} \\ &= \frac{4N(N-1)}{\rho^2 Q_N^{\rm ann}} \int d\varsigma^N\, \delta(\varsigma_a-\varsigma_1)\delta(\varsigma_b-\varsigma_2)\exp\left[-\beta\Phi_N^{\rm ann}(\varsigma^N)\right], \end{aligned} \tag{2.67}$$

where $\delta(\varsigma_a-\varsigma_\alpha)\equiv\delta_{\mathbf{s}_a,\mathbf{s}_\alpha}\delta(\mathbf{r}_a-\mathbf{r}_\alpha)$. In the absence of interactions, $Q_N^{\rm ann}\to 2^N V^N$ and $g^{\rm ann}(\varsigma_a,\varsigma_b)\to 1$ in the thermodynamic limit.

By standard diagrammatic methods [27] one can find the virial expansion of the pair correlation function as

$$g^{\rm ann}(\varsigma_1,\varsigma_2) = e^{-\beta\phi(\varsigma_1,\varsigma_2)}\left[1 + \;\rho + \frac{1}{2}\left(2\;\; + 4\;\; + \;\; + \;\;\right)\rho^2\right] + \mathcal{O}(\rho^3), \tag{2.68}$$

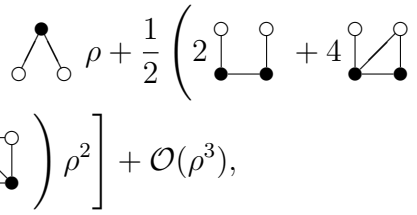

where, for instance,

$$= \frac{1}{2}\int d\varsigma_3\, f(\varsigma_1,\varsigma_3) f(\varsigma_3,\varsigma_2), \tag{2.69a}$$

$$= \frac{1}{2^2}\int d\varsigma_3 \int d\varsigma_4\, f(\varsigma_1,\varsigma_3) f(\varsigma_3,\varsigma_4) f(\varsigma_4,\varsigma_2). \tag{2.69b}$$

Here, $f(\varsigma_\alpha,\varsigma_\gamma)\equiv e^{-\beta\phi(\varsigma_\alpha,\varsigma_\gamma)}-1$ is the Mayer function. The rest of the diagrams are defined in a similar way.

By summing over the four possible combinations $(\mathbf{s}_1,\mathbf{s}_2)$, we can finally define the radial distribution function of the annealed system as

$$g^{\rm ann}(r_{12}) = \frac{1}{4}\sum_{\mathbf{s}_1=\mathbf{s}_\pm}\sum_{\mathbf{s}_2=\mathbf{s}_\pm} g^{\rm ann}(\mathbf{s}_1,\mathbf{r}_1;\mathbf{s}_2,\mathbf{r}_2). \tag{2.70}$$

2.5.2 Quenched system

Now we consider a system where N_1 particles have always spin up ($\mathbf{s}_+$) and therefore belong to species $i = 1$. The rest of the particles ($N_2 = N - N_1$) have always spin down ($\mathbf{s}_-$) and belong to species $i = 2$. Without loss of generality we can assume that species $i = 1$ is made of particles $\alpha = 1, \dots, N_1$ and species $i = 2$ is made of particles $\alpha = N_1 + 1, \dots, N$. The mole fractions are $x_i = N_i/N$. In this quenched binary mixture a microstate is specified by the set of positions $\mathbf{r}^N \equiv \{\mathbf{r}_1, \dots, \mathbf{r}_N\}$ only, as the spins are fixed from the beginning.

In the canonical ensemble, the probability density of the microstate $\{\mathbf{r}_1, \dots, \mathbf{r}_N\}$ is

$$\rho^{\text{quen}}_{N_1,N_2}(\mathbf{r}^N) = \frac{\exp\left[-\beta\Phi^{\text{quen}}_{N_1,N_2}(\mathbf{r}^N)\right]}{Q^{\text{quen}}_{N_1,N_2}}, \quad Q^{\text{quen}}_{N_1,N_2} = \int d\mathbf{r}^N \, \exp\left[-\beta\Phi^{\text{quen}}_{N_1,N_2}(\mathbf{r}^N)\right], \tag{2.71}$$

where the superscript "quen" stands for "quenched" and

$$\Phi^{\text{quen}}_{N_1,N_2}(\mathbf{r}^N) = \sum_{\alpha=1}^{N_1-1}\sum_{\gamma=\alpha+1}^{N_1}\phi_{11}(\mathbf{r}_{\gamma\alpha}) + \sum_{\alpha=N_1+1}^{N-1}\sum_{\gamma=\alpha+1}^{N}\phi_{22}(\mathbf{r}_{\gamma\alpha}) + \sum_{\alpha=1}^{N_1}\sum_{\gamma=N_1+1}^{N}\phi_{12}(\mathbf{r}_{\gamma\alpha}) \tag{2.72}$$

is the total potential energy. Comparison between Eqs. (2.66) and (2.71) shows the relationship

$$Q^{\text{ann}}_N = \sum_{N_1=0}^{N}\binom{N}{N_1} Q^{\text{quen}}_{N_1,N_2}. \tag{2.73}$$

The three pair correlation functions of the binary mixture are defined as

$$g_{11}^{\rm quen}(\mathbf{r}_a,\mathbf{r}_b) = \frac{1}{x_1^2\rho^2}\left\langle \sum_{\alpha=1}^{N_1}\sum_{\gamma=1}^{N_1}{}' \,\delta(\mathbf{r}_a-\mathbf{r}_\alpha)\delta(\mathbf{r}_b-\mathbf{r}_\gamma)\right\rangle_{\rho_N^{\rm quen}}$$
$$= \frac{N_1(N_1-1)}{x_1^2\rho^2 Q_{N_1,N_2}^{\rm quen}}\int d\mathbf{r}^N\,\delta(\mathbf{r}_a-\mathbf{r}_1)\delta(\mathbf{r}_b-\mathbf{r}_2)\exp\left[-\beta\Phi_{N_1,N_2}^{\rm quen}(\mathbf{r}^N)\right], \tag{2.74a}$$

$$g_{22}^{\rm quen}(\mathbf{r}_a,\mathbf{r}_b) = \frac{1}{x_2^2\rho^2}\left\langle \sum_{\alpha=N_1+1}^{N}\sum_{\gamma=N_1+1}^{N}{}' \,\delta(\mathbf{r}_a-\mathbf{r}_\alpha)\delta(\mathbf{r}_b-\mathbf{r}_\gamma)\right\rangle_{\rho_N^{\rm quen}}$$
$$= \frac{N_2(N_2-1)}{x_2^2\rho^2 Q_{N_1,N_2}^{\rm quen}}\int d\mathbf{r}^N\,\delta(\mathbf{r}_a-\mathbf{r}_{N-1})\delta(\mathbf{r}_b-\mathbf{r}_N)\exp\left[-\beta\Phi_{N_1,N_2}^{\rm quen}(\mathbf{r}^N)\right], \tag{2.74b}$$

$$g_{12}^{\rm quen}(\mathbf{r}_a,\mathbf{r}_b) = \frac{1}{x_1x_2\rho^2}\left\langle \sum_{\alpha=1}^{N_1}\sum_{\gamma=N_1+1}^{N} \,\delta(\mathbf{r}_a-\mathbf{r}_\alpha)\delta(\mathbf{r}_b-\mathbf{r}_\gamma)\right\rangle$$
$$= \frac{N_1N_2}{x_1x_2\rho^2 Q_{N_1,N_2}^{\rm quen}}\int d\mathbf{r}^N\,\delta(\mathbf{r}_a-\mathbf{r}_1)\delta(\mathbf{r}_b-\mathbf{r}_N)\exp\left[-\beta\Phi_{N_1,N_2}^{\rm quen}(\mathbf{r}^N)\right]. \tag{2.74c}$$

In Eqs. (2.74a) and (2.74b) the prime in the summations denotes the constraint $\alpha\neq\gamma$. Equations (2.74a)–(2.74c) can be written in a compact way as

$$g_{ij}^{\rm quen}(\mathbf{r}_a,\mathbf{r}_b) = \frac{N_i(N_j-\delta_{ij})}{x_ix_j\rho^2 Q_{N_1,N_2}^{\rm quen}}\int d\mathbf{r}^N\,\delta(\mathbf{r}_a-\mathbf{r}_{I_i})\delta(\mathbf{r}_b-\mathbf{r}_{J_j})\exp\left[-\beta\Phi_{N_1,N_2}^{\rm quen}(\mathbf{r}^N)\right]. \tag{2.75}$$

where $I_1=1$, $I_2=N-1$, $J_1=2$, $J_2=N$. Note that, in the absence of interactions, $Q_{N_1,N_2}^{\rm quen}=V^N$ and $g_{ij}(\mathbf{r}_a,\mathbf{r}_b)\to 1$ in the thermodynamic limit.

The virial expansion of the pair correlation function $g_{ij}^{\rm quen}(\mathbf{r}_1,\mathbf{r}_2)$ is

$$g_{ij}^{\rm quen}(\mathbf{r}_1,\mathbf{r}_2) = e^{-\beta\phi_{ij}(\mathbf{r}_1,\mathbf{r}_2)}\left[1+ \;\rho+\frac{1}{2}\left(2\;\;+4\;\;\right.\right.$$
$$\left.\left.+\;\;+\;\;\right)\rho^2\right]+\mathcal{O}(\rho^3), \tag{2.76}$$

where in this quenched case [compare with Eq. (2.69) for the annealed case],


$= \int^{\dagger} d\varsigma_3\, f(\varsigma_1,\varsigma_3) f(\varsigma_3,\varsigma_2),$

$= \int^{\dagger} d\varsigma_3 \int^{\dagger} d\varsigma_4\, f(\varsigma_1,\varsigma_3) f(\varsigma_3,\varsigma_4) f(\varsigma_4,\varsigma_2),$ (2.77)

and so on. Here, we have introduced the notation $\int^{\dagger} d\varsigma_\alpha \equiv \sum_{i_\alpha=1,2} x_{i_\alpha} \int d\mathbf{r}_\alpha$, where, in each term of the sum, particle α belongs to species i_α.

In analogy with Eq. (2.15), the average pair correlation function is

$$g^{\text{quen}}(r_{12}) = \sum_{i,j} x_i x_j g_{ij}^{\text{quen}}(\mathbf{r}_1,\mathbf{r}_2). \tag{2.78}$$

2.5.3 Mapping $g_{ij}^{\text{quen}}(\mathbf{r}_1,\mathbf{r}_2) \to g^{\text{ann}}(\varsigma_1,\varsigma_2)$

Comparison between Eqs. (2.67) and (2.75) shows that, for a finite value of N and in a strict mathematical sense, $g^{\text{ann}}(\mathbf{s}_i,\mathbf{r}_1;\mathbf{s}_j,\mathbf{r}_2) \neq g_{ij}^{\text{quen}}(\mathbf{r}_1,\mathbf{r}_2)$, even if the quenched mixture is equimolar ($x_1 = x_2 = \frac{1}{2}$). On the other hand, comparison between Eqs. (2.68) and (2.76) shows that

$$g^{\text{ann}}(\mathbf{s}_i,\mathbf{r}_1;\mathbf{s}_j,\mathbf{r}_2) = g_{ij}^{\text{quen}}(\mathbf{r}_1,\mathbf{r}_2) \tag{2.79}$$

if $x_1 = x_2 = \frac{1}{2}$. The equality in Eq. (2.79) is obvious to second order in density, as can be seen by comparison between Eqs. (2.69) and (2.77), but extends to any order.

The solution to this paradox lies in the fact that the thermodynamic limit needs to be taken in the derivation of Eqs. (2.68) and (2.76). Thus, the equivalence between the annealed and quenched systems holds in that limit, similarly to the equivalence between different statistical ensembles. In other words, if $N \to \infty$, the huge majority of the relevant microstates in the quenched system correspond to a number of up spins practically equal to the number of down spins. As a consequence, we can expect that [see Eq. (2.73)]

$$\ln Q_N^{\text{ann}} \approx \ln \left[\binom{N}{N/2} Q_{N/2,N/2}^{\text{quen}} \right] \tag{2.80}$$

and Eq. (2.79) holds true in the thermodynamic limit. As a plausibility argument in favor of Eq. (2.80), note that

$$\ln \sum_{N_1=0}^{N} \binom{N}{N_1} = N \ln 2 \approx \ln \binom{N}{N/2}. \tag{2.81}$$

As said before, the content of this section can easily be extended to the case where in the annealed system a certain bias makes the fraction of particles with spin $\mathbf{s}_+$ fluctuate around a value $x_1 \neq \frac{1}{2}$, in which case the equivalent quenched system has a mole fraction $x_1 \neq \frac{1}{2}$.

2.6 Validation of the quenched-annealed mapping by Monte Carlo simulations

Strictly speaking, the exact statistical-mechanical solution to the one-dimensional Janus fluid worked out in Sec. 2.4 applies to the quenched system with arbitrary composition, but not, in principle, to the annealed system. On the other hand, according to the arguments presented in Sec. 2.5, the annealed system is expected to be described in the thermodynamic limit by the solution to the quenched system. In order to validate and confirm this expectation, we have carried out NVT Monte Carlo (MC) simulations [38] on the one-component, annealed system.

In the MC simulations, a system of $N = 500$ Janus particles are distributed over a ring of length $L = N/\rho$ (with periodic boundary conditions). In each computational step, the microscopic configuration of the system is fully determined by the position and orientation of every particle. In order to thermalize the system and measure its equilibrium properties, a random walk over the configuration (position plus orientation) space is performed. In each MC step, a particle is selected at random and provisionally displaced a random distance. If an overlap occurs, the displacement is rejected and a new MC step is initiated. In the absence of any overlap, the active face of the chosen particle is provisionally assigned to

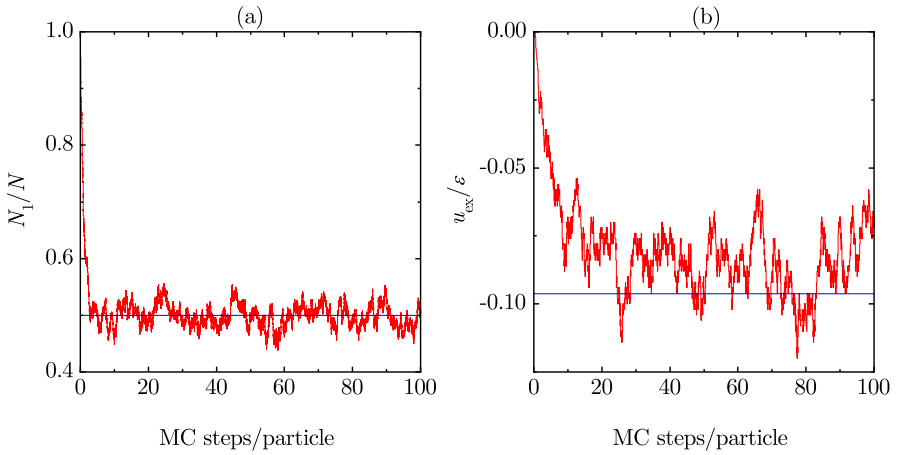

FIGURE 2.7: Evolution of (a) N_1/N and (b) u_{ex}/ϵ versus the number of MC steps per particle for an annealed system (unbiased one-component fluid) with $\lambda = 1.2$ at $T^* = 1$ and $\rho = 0.5$. The horizontal lines represent the equilibrium values (a) $N_1/N = \frac{1}{2}$ and (b) $u_{ex}/\epsilon = -0.0962(4)$.

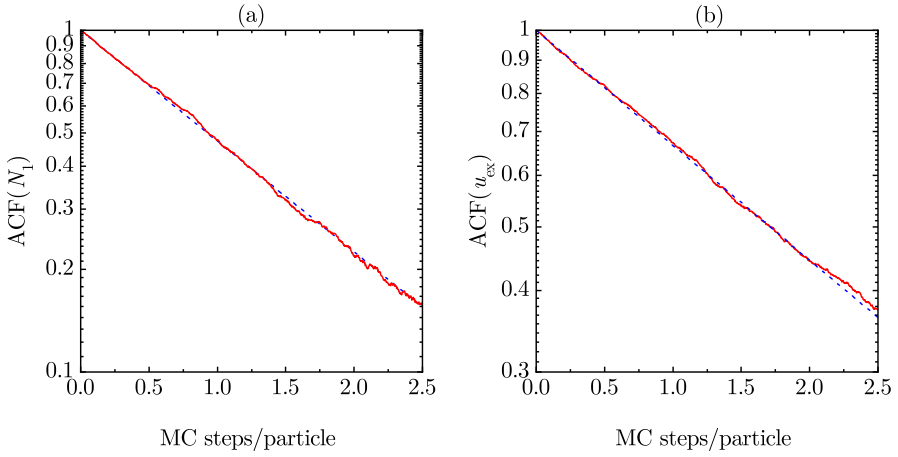

FIGURE 2.8: Logarithmic plot of the ACF of (a) N_1 and (b) u_{ex} versus the number of MC steps per particle for an annealed system (unbiased one-component fluid) with $\lambda = 1.2$ at $T^* = 1$ and $\rho = 0.5$. The dashed lines represent e^{-t/τ_c}, where t is the number of MC steps per particle and the autocorrelation time is (a) $\tau_c = 1.34$ and (b) $\tau_c = 2.47$.

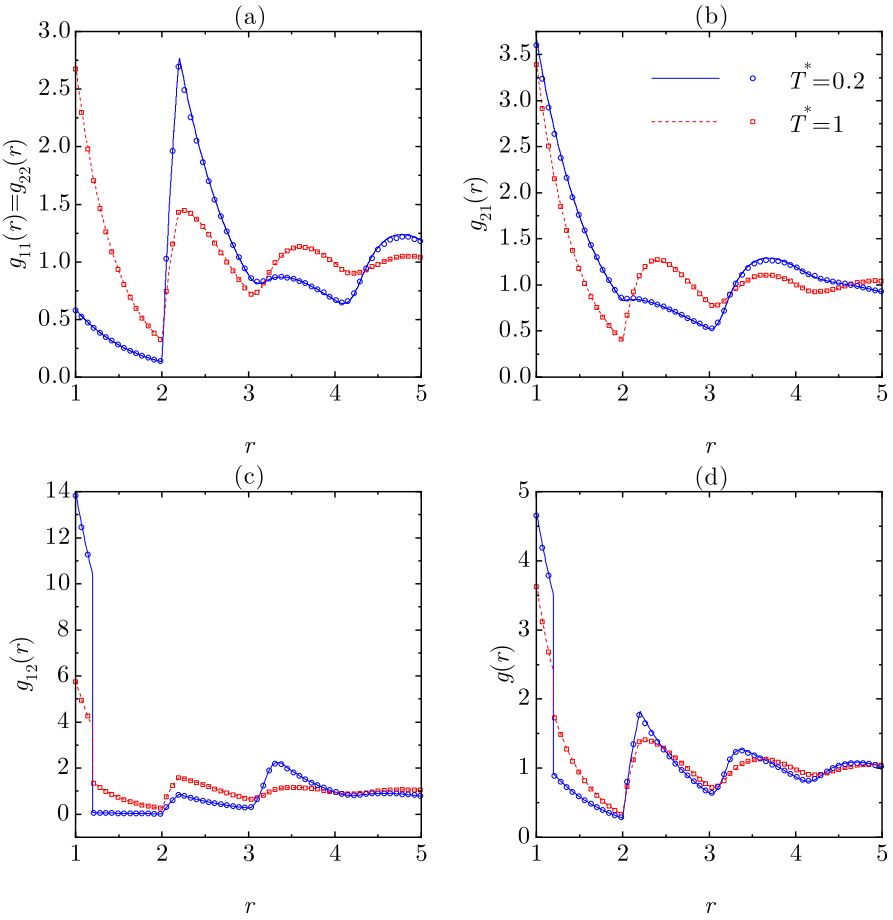

FIGURE 2.9: Plot of (a) $g_{11}(r) = g_{22}(r)$, (b) $g_{21}(r)$, (c) $g_{12}(r)$, and (d) $g(r)$ at density $\rho = 0.7$ and temperatures $T^* = 0.2$ and 1 for a Janus fluid with $\lambda = 1.2$. Lines represent the exact solution for the quenched system (equimolar binary mixture), while symbols are MC results for the annealed system (unbiased one-component fluid).

its right-hand side or to its left-hand side with probabilities q_1 or $q_2 = 1 - q_1$, respectively. The attempt (displacement plus active face assignment) is accepted according to the Metropolis criterion [38]. The size of the position displacement is adjusted so that the acceptance ratio is approximately 50%. We have typically used 10^5 MC steps per particle for equilibration plus an additional set of 5×10^5 MC steps per particle for the computation of the equilibrium quantities as averages. Except at the end of this section, we have restricted ourselves to *unbiased* annealed Janus fluids ($q_1 = q_2 = \frac{1}{2}$).

We have simulated annealed systems with $\lambda = 1.2$ at a low temperature ($T^* = 0.2$) and at an intermediate temperature ($T^* = 1$), in each case with densities

$\rho = 0.1, 0.2, \ldots, 0.8$. As an illustration of the evolution of the main quantities, Fig. 2.7 displays the MC evolution of the ratio N_1/N (where N_1 denotes the fluctuating number of particles with a right active face) and the (reduced) excess energy per particle u_{ex}/ϵ at $T^* = 1$ and $\rho = 0.5$. In the initial configuration, particles are equispaced (so that $u_{\text{ex}}/\epsilon = 0$) with their active faces oriented to the right (so that $N_1 = N$). As we can observe in Fig. 2.7(a), after about only 10 MC steps per particle the fraction of particles with a given orientation fluctuates about the value $\frac{1}{2}$. On the other hand, the equilibration of the thermodynamic and structural properties is much slower. In particular, Fig. 2.7(b) shows that the energy has not relaxed yet to its equilibrium value after about 100 MC steps per particle.

Figure 2.8 shows the autocorrelation function (ACF) [39, 40] of N_1 and u_{ex} for the same case as that of Fig. 2.7. The ACF has been obtained in the equilibrium stage by averaging over 4000 blocks, each one made of 2.5 MC steps per particle. It can be observed that in both cases the ACF decays exponentially with a characteristic autocorrelation time, τ_c, of about 1.34 and 2.47 MC steps per particle for N_1 and u_{ex}, respectively. Therefore, the number of MC steps needed to perform sampling between statistically uncorrelated configurations in the case of energy is almost twice that in the case of the number of particles with a given orientation.

In all the simulated states, we have found an excellent agreement between the theoretical and the MC functions $g_{ij}(r)$ for the quenched and annealed systems, respectively. As an example, Fig. 2.9 shows $g_{11}(r) = g_{22}(r)$, $g_{12}(r)$, $g_{21}(r)$, and $g(r)$ at $\rho = 0.7$ and $T^* = 0.2$ and 1.

Apart from the pair correlation functions, the excess internal energy per particle (u_{ex}/ϵ) and the pressure (βp) have been computed in the MC simulations. While the excess internal energy can be evaluated directly, the pressure requires an alternative method. According to Eqs. (2.2), (2.14), and (2.21), the cavity functions $y_{ij}(r) \equiv g_{ij}(r)e^{\beta\phi_{ij}(r)}$ are proportional to $e^{-\beta pr}$ within the first coordination shell ($1 < r < 2$). In the case of the Janus fluid, this means that a logarithmic plot of $y_{11}(r) = y_{22}(r) = g_{11}(r) = g_{22}(r)$, $y_{21}(r) = g_{21}(r)$, and

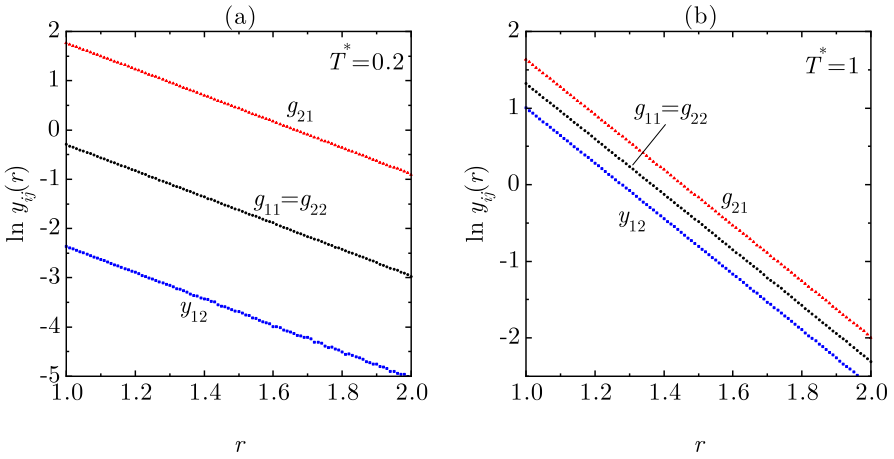

FIGURE 2.10: Plot of $\ln g_{11}(r) = \ln g_{22}(r)$, $\ln g_{21}(r)$, and $\ln y_{12}(r)$ in the first coordination shell ($1 < r < 2$), as obtained from MC simulations for an annealed system (unbiased one-component fluid) with $\lambda = 1.2$ at $\rho = 0.8$ and (a) $T^* = 0.2$ and (b) $T^* = 1$. The average slopes give (a) $\beta p = 2.68$ and (b) $\beta p = 3.63$, respectively.

$y_{12}(r) = g_{12}(r)\left[1 - (1 - e^{-1/T^*})\Theta(\lambda - r)\right]$ in the region $1 < r < 2$ should give straight lines with a *common* slope equal to $-\beta p$. As an illustration, Fig. 2.10 shows a plot of $\ln y_{ij}(r)$ in the cases $T^* = 0.2$ and $T^* = 1$, both with $\rho = 0.8$. It must be noted that this method to obtain the pressure cannot be applied to the average pair correlation function $g(r)$ but requires to disentangle the partial contributions $g_{ij}(r)$.

The thermodynamic quantities $\beta p/\rho$ and $u_{\rm ex}/\epsilon$ as functions of ρ are compared with the theoretical curves for the quenched systems in Fig. 2.11, again with a virtually perfect agreement. We have estimated the errors in the simulation values by dividing the 5×10^5 MC steps per particle into 25 blocks, each one made of 2×10^4 MC steps per particle, and checked that the error bars are smaller than the size of symbols in Fig. 2.11. For instance, in the state $\rho = 0.5$ and $T^* = 1$ we have obtained $u_{\rm ex}/\epsilon = -0.0962(4)$ and $\beta p = 1.890(2)$, where the numbers enclosed by parentheses represent standard deviations. In the case of pressure, the error estimate takes into account that the linear fit of $\ln y_{ij}(r)$ is made over 100 values equispaced between $r = 1$, and $r = 2$, each one with an error of about 0.014.

So far, we have paid special attention to the mapping between *unbiased* annealed systems and *equimolar* quenched systems. On the other hand, given that

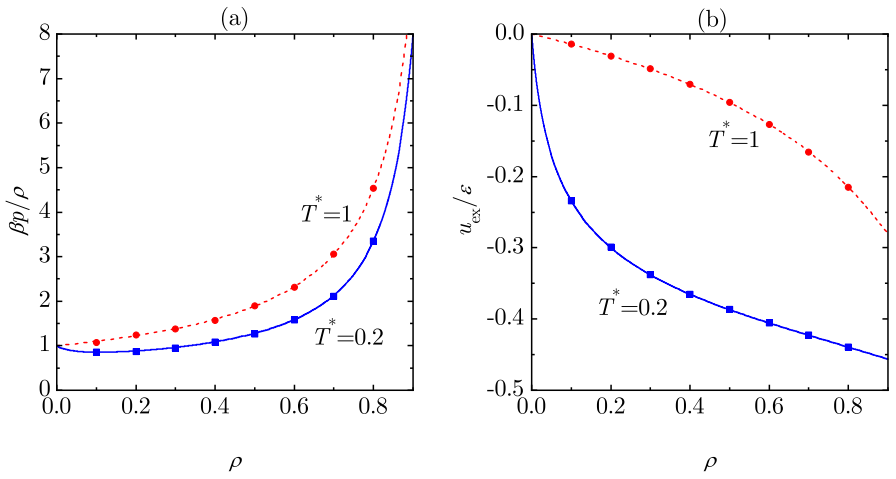

FIGURE 2.11: Plot of (a) the compressibility factor $\beta p/\rho$ and (b) the excess internal energy per particle $u_{\rm ex}/\epsilon$ versus density at temperatures $T^* = 0.2$ and 1 for a Janus fluid with $\lambda = 1.2$. Lines represent the exact solution for the quenched system (equimolar binary mixture), while symbols are MC results for the annealed system (unbiased one-component fluid).

the arguments in Sec. 2.5 can be extended to the biased/nonequimolar scenario, it is important to validate this expectation also in that case. A biased annealed system can be simulated by choosing a value different from $\frac{1}{2}$ for the parameter q_1 introduced above. In such a case, the fraction of particles with the orientation labeled as 1 fluctuates around a value $x_1 \neq \frac{1}{2}$. One might intuitively expect that $x_1 = q_1$ after thermalization. However, we have observed that this is not the case but instead $x_1 < q_1$ if $q_1 > \frac{1}{2}$. This means that there are more rejections in the attempts to assign the majority orientation than in the attempts to assign the minority one.

In particular, we have studied biased systems with $\lambda = 1.2$, $\rho = 0.5$, and $T^* = 1$, observing that the choices $q_1 = 0.60$, 0.70, and 0.80 lead to average fractions $x_1 = 0.5883$, 0.6789, and 0.7748, respectively. As an illustrative example, Fig. 2.12 compares the four correlation functions $g_{ij}(r)$ obtained in our MC simulations with $q_1 = 0.80$ against the exact solution for the quenched system with $x_1 = 0.7748$. Again, an excellent agreement is apparent. The simulation points in the case of $g_{22}(r)$ are a bit noisier because in that case the 2–2 pairs represent about 5% of the total number of pairs. The simulation (theoretical) values of the excess internal

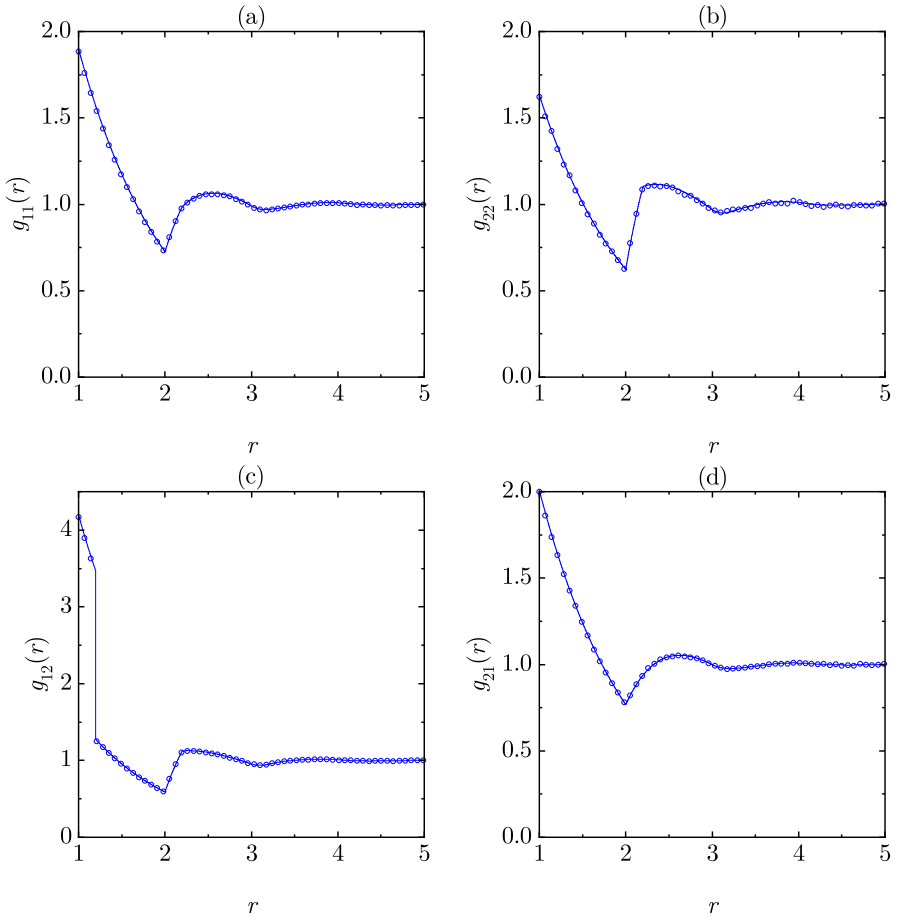

FIGURE 2.12: Plot of (a) $g_{11}(r)$, (b) $g_{22}(r)$, (c) $g_{12}(r)$, and (d) $g_{21}(r)$ at density $\rho = 0.5$ and temperature $T^* = 1$ for a Janus fluid with $\lambda = 1.2$ and a mole fraction $x_1 = 0.7748$. Lines represent the exact solution for the quenched system (nonequimolar binary mixture), while symbols are MC results for the annealed system (biased one-component fluid).

energy per particle are $|u_{\text{ex}}|/\epsilon = 0.09313$ (0.09307), 0.08364 (0.08357), and 0.06654 (0.06662) for $x_1 = 0.5883$, 0.6789, and 0.7748, respectively.

Therefore, Figs. 2.9–2.12 confirm that, as argued in Sec. 2.5, the macroscopic properties of the quenched Janus fluid (where particles have a fixed orientation) are equivalent, in the thermodynamic limit, to those of the annealed Janus fluid (where particles are allowed to flip their orientation).

2.7 Summary and remarks

In this chapter we have extensively studied the statistical-mechanical properties of one-dimensional Janus fluids. First, we have considered a general m-component mixture with anisotropic interactions, such that the interaction potential between a particle α and its nearest neighbor $\gamma = \alpha \pm 1$ depends on whether the latter is located to the left ($\gamma = \alpha - 1$) or to the right ($\gamma = \alpha + 1$) of α. By carefully extending the method followed in the case of isotropic interactions [27], we have derived the exact solution in the isothermal-isobaric ensemble. By particularizing to a binary mixture ($m = 2$) with the Kern–Frenkel potential [14], as given by Eq. (2.42), the pair correlation functions $g_{ij}(r)$ and thermodynamic quantities (density and internal energy) are obtained as explicit functions of pressure, temperature, and composition. The mixture represents what we have called a *quenched* Janus fluid since the orientation of the active face of each particle is kept fixed.

In the final part of the first chapter we have addressed the question of whether the derived exact results for the quenched Janus fluid are applicable to the case of the *annealed* Janus fluid. In the latter, all the particles are identical, so that one is dealing with a one-component system in which the particles are allowed to flip their orientation and, as a consequence, the number of particles with either orientation fluctuates around a certain average value. In Sec. 2.5 we have presented compelling arguments in favor of the quenched↔annealed equivalence in the thermodynamic limit. This has been further supported by comparison between the theoretical results for quenched systems and MC simulations for annealed systems (both unbiased and biased). Structural as well as thermodynamic quantities are seen to exhibit an excellent agreement. This in turn validates the theoretical results derived in this chapter.

While most of the results presented in this chapter apply to fluids confined to one-dimensional geometries, they can contribute to a better understanding of some of the peculiar physical properties of Janus fluids and also serve as a benchmark to test theoretical approaches. Additionally, the equivalence between the quenched

and annealed systems gives support to the three-dimensional (quenched) up-down Janus mixture model considered in the following chapters.

3

Janus fluid with fixed patch orientations: Theory and simulations

3.1 Introduction

The thermophysical and structural properties of the three-dimensional Janus fluid have been investigated within the framework of the Kern–Frenkel model using numerical simulations [8, 15], thus rationalizing the cluster formation mechanism characteristic of the experiments [41]. The fluid-fluid transition was found to display an unconventional and particularly interesting phase diagram, with a re-entrant transition associated with the formation of a cluster phase at low temperatures and densities [8, 15]. While numerical evidence of this transition is quite

convincing, a minimal theory including all necessary ingredients for the onset of this anomalous behavior is still missing. Two previous attempts are however noteworthy. Reinhardt *et al.* [42] introduced a van der Waals theory for a suitable mixture of clusters and monomers that accounts for a re-entrant phase diagram, whereas Fantoni *et al.* [43, 44] developed a cluster theory explaining the appearance of some "magic numbers" in the cluster formation.

The aim of the present chapter is to attempt a new route in this direction. We will do this by considering a Janus fluid within the Kern–Frenkel model, where the orientations of the SW hemispheres are constrained to be along either North or South, in a spirit akin to Zwanzig model for the isotropic-nematic transition in liquid crystals [45] and reminiscent of the one-dimensional situation studied in Ch. 2.

Upon observing that under those conditions, one ends up with only four possible different interactions (North-North, North-South, South-North, and South-South), this constrained model will be further mapped onto a binary mixture interacting via a "quasi" isotropic potential. Here the term "quasi" refers to the fact that a certain memory of the original anisotropic Kern–Frenkel potential is left: after the mapping, one has to discriminate whether a particle with patch pointing North ("spin-up") is lying above or below that with a patch pointing South ("spin-down"). This will introduce an asymmetry in the unlike components of the binary mixture, as explained in detail below. In order to make the problem tractable from the analytical point of view, the particular limit of an infinitely narrow and deep square-well (sticky limit) will be considered. This limit was originally devised by Baxter and constitutes the celebrated one-component sticky-hard-sphere (SHS) or adhesive Baxter model [32]. By construction, our model reduces to it in the limit of fully isotropic attractive interactions. The latter model was studied within the Percus–Yevick (PY) closure [30] in the original Baxter work and in a subsequent work by Watts *et al.* [46] The extension of this model to a binary mixture was studied by several authors [47, 48, 49, 50, 51]. The SHS model with Kern–Frenkel potential was also studied in Ref. [52], via a virial expansion at low densities.

A methodology alternative to the one used in the above studies hinges on the so-called "rational-function approximation" (RFA) [53, 54, 55, 56, 57], and is known to be equivalent to the PY approximation for the one-component SHS Baxter model [32] and for its extension to symmetric SHS mixtures [47, 51, 53]. The advantage of this approach is that it can be readily extended to more general cases, and this is the reason why it will be employed in the present analysis to consider the case of asymmetric interactions. We will show that this approach provides a rather precise estimate of the thermodynamic and structural properties of the Janus fluids with up-down orientations by explicitly testing it against Monte Carlo (MC) simulations of the same Janus fluid.

The remaining part of the chapter is envisaged as follows. Section 3.2 describes our Janus model and its mapping onto a binary mixture with asymmetric interactions. It is shown in Sec. 3.3 that the thermophysical quantities do not require the knowledge of the full (anisotropic) pair correlation functions but only of the functions averaged over all possible North or South orientations. Section 3.4 is devoted to the sticky-limit version of the model, i.e., the limit in which the SW hemisphere has a vanishing well width but an infinite depth leading to a constant value of the Baxter parameter τ. The exact cavity functions to first order in density (and hence exact up to second and third virial coefficients) in the sticky limit are worked out in Appendix C. Up to that point all the equations are formally exact in the context of the model. Then, in Sec. 3.5 we present our approximate RFA theory, which hinges on a heuristic extension from the PY solution for mixtures with symmetric SHS interactions to the realm of asymmetric SHS interactions. Some technical aspects are relegated to Appendices D and E. The prediction of the resulting analytical theory are compared with MC simulations in Sec. 3.6, where a semi-quantitative agreement is found.

3.2 Mapping the Kern–Frenkel potential onto a binary mixture

3.2.1 The Kern–Frenkel potential for a Janus fluid

Consider a fluid of spheres with identical diameters σ where the surface of each sphere is divided into two parts. The first hemisphere (the green one in the color code given in Fig. 3.1) has a SW character, thus attracting another identical hemisphere via a SW potential of width $(\lambda - 1)\sigma$ and depth ϵ. The second hemisphere (the red one in the color code of Fig. 3.1) is instead a HS potential. The orientational dependent pair potential between two arbitrary particles μ and ν ($\mu, \nu = 1, \ldots, N$, where N is the total number of particles in the fluid) has then the form proposed by Kern and Frenkel [14]

$$\Phi\left(\mathbf{r}_{\mu\nu}, \widehat{\mathbf{n}}_{\mu}, \widehat{\mathbf{n}}_{\nu}\right) = \phi_{\mathrm{HS}}\left(r_{\mu\nu}\right) + \phi_{\mathrm{SW}}\left(r_{\mu\nu}\right) \Psi\left(\widehat{\mathbf{r}}_{\mu\nu}, \widehat{\mathbf{n}}_{\mu}, \widehat{\mathbf{n}}_{\nu}\right), \tag{3.1}$$

where the first term is the HS contribution

$$\phi_{\mathrm{HS}}\left(r\right) = \begin{cases} \infty, & 0 < r < \sigma, \\ 0, & \sigma < r, \end{cases} \tag{3.2}$$

and the second term is the orientation-dependent attractive part, which can be factorized into an isotropic SW tail

$$\phi_{\mathrm{SW}}\left(r\right) = \begin{cases} -\epsilon, & \sigma < r < \lambda\sigma, \\ 0, & \lambda\sigma < r, \end{cases} \tag{3.3}$$

multiplied by an angular dependent factor

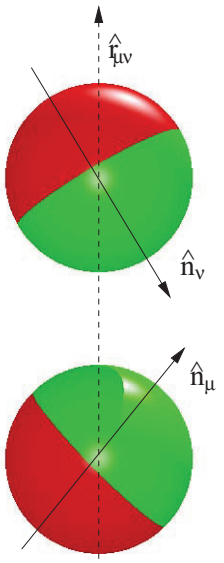

FIGURE 3.1: The Kern–Frenkel potential for Janus fluids.

$$\Psi\left(\widehat{\mathbf{r}}_{\mu\nu}, \widehat{\mathbf{n}}_\mu, \widehat{\mathbf{n}}_\nu\right) = \begin{cases} 1, & \text{if } \widehat{\mathbf{n}}_\mu \cdot \widehat{\mathbf{r}}_{\mu\nu} \geq 0 \text{ and } \widehat{\mathbf{n}}_\nu \cdot \widehat{\mathbf{r}}_{\mu\nu} \leq 0 \\ 0, & \text{otherwise.} \end{cases} \tag{3.4}$$

Here, $\widehat{\mathbf{r}}_{\mu\nu} = \mathbf{r}_{\mu\nu}/r_{\mu\nu}$, where $\mathbf{r}_{\mu\nu} = \mathbf{r}_\nu - \mathbf{r}_\mu$, is the unit vector pointing (by convention) from particle μ to particle ν and the unit vectors $\widehat{\mathbf{n}}_\mu$ and $\widehat{\mathbf{n}}_\nu$ are "spin" vectors associated with the orientation of the attractive hemispheres of particles μ and ν, respectively (see Fig. 3.1). An attractive interaction then exists only between the two SW portions of the surface sphere, provided that the two particles are within the range of the SW potential.

3.2.2 Asymmetric binary mixture

In analogy with the one-dimensional case (see Chap. 1), we now consider the particular case where the only possible orientations of particles are with attractive caps pointing only either North or South with equal probability, as obtained by Fig. 3.1 in the limit $\widehat{\mathbf{n}}_\mu = \widehat{\mathbf{z}}$, $\widehat{\mathbf{n}}_\nu = -\widehat{\mathbf{z}}$, and with $\widehat{\mathbf{z}}$ pointing North.

Under these conditions, one then notes that the Kern–Frenkel potential (3.1)–(3.4) can be simplified by associating a spin $i = 1$ (up) to particles with SW

hemispheres pointing in the North $\widehat{\mathbf{z}}$ direction and a spin $j = 2$ (down) to particles with SW hemispheres pointing in the South $-\widehat{\mathbf{z}}$ direction, so one is left with only four possible configurations depending on whether particles of type 1 lie above or below particles of type 2, as illustrated in Fig. 3.2. The relationship between the genuine Janus model (see Fig. 3.1) and the up-down model (see Fig. 3.2) is reminiscent to the relationship between the Heisenberg and the Ising model of ferromagnetism. From that point of view, our model can be seen as an Ising-like version of the original Janus model. A similar spirit was also adopted in the Zwanzig model for the isotropic-nematic transition in liquid crystals [45].

The advantage of this mapping is that one can disregard the original anisotropic Janus-like nature of the interactions and recast the problem in the form of a binary mixture such that the interaction potential between a particle of species i located at $\mathbf{r}_1$ and a particle of species j located at $\mathbf{r}_2$ has the *asymmetric* form

$$\begin{aligned} \phi_{ij}(\mathbf{r}_1, \mathbf{r}_2) &= \phi_{ij}(\mathbf{r}_{12}) \\ &= \varphi_{ij}(r_{12})\Theta(\cos\theta_{12}) + \varphi_{ji}(r_{12})\Theta(-\cos\theta_{12}), \end{aligned} \tag{3.5}$$

where $\cos\theta_{12} = \widehat{\mathbf{r}}_{12} \cdot \widehat{\mathbf{z}}$ (recall our convention $\mathbf{r}_{12} = \mathbf{r}_2 - \mathbf{r}_1$) and

$$\varphi_{ij}(r) = \phi_{\mathrm{HS}}(r) + \begin{cases} \phi_{\mathrm{SW}}(r), & \text{if } i = 1 \text{ and } j = 2, \\ 0, & \text{otherwise.} \end{cases} \tag{3.6}$$

We recall that the Heaviside function is defined as $\Theta(x) = 1$ and 0 for $x > 0$ and $x < 0$, respectively.

It is important to remark that, in general, $\varphi_{12}(r) \neq \varphi_{21}(r)$, as evident from Eq. (3.6). Thus, the binary mixture is not necessarily symmetric [unless $\epsilon = 0$ or $\lambda = 1$ in Eq. (3.3)], unlike standard binary mixtures where this symmetry condition is ensured by construction. In the potential (3.5), there however is still a "memory" of the original anisotropy since the potential energy of a pair of particles of species i and j separated a distance r_{12} depends on whether particle j is

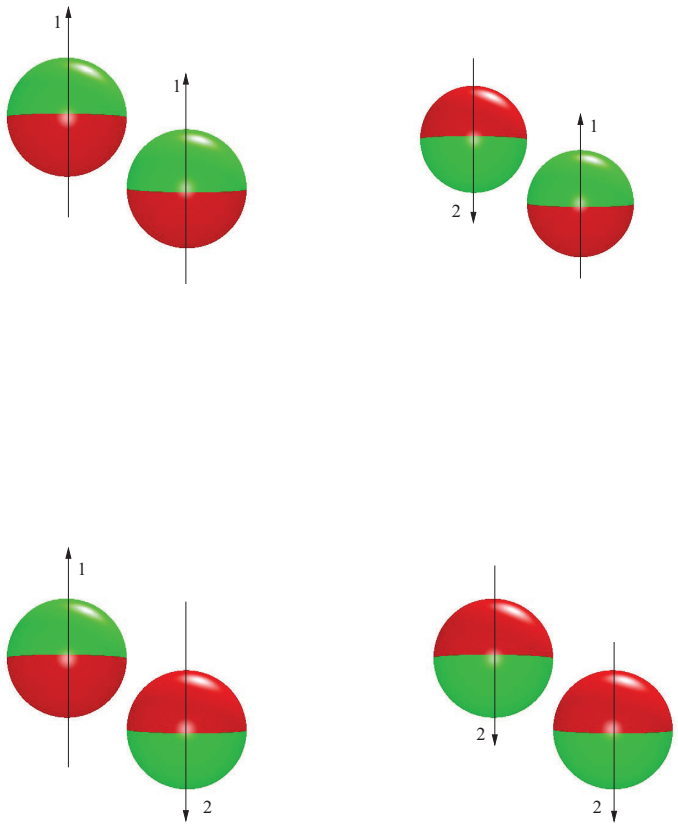

FIGURE 3.2: (Top-left) A particle of type 1 is "below" another particle of type 1 providing SW/HS=HS interactions. (Top-right) A particle of type 1 is "below" a particle of type 2 leading to SW/SW=SW interactions. (Bottom-left) A particle of type 2 is "below" a particle of type 1 yielding HS/HS=HS interactions. (Bottom-right) A particle of type 2 is "below" another particle of type 2 thus leading again to HS/SW=HS interactions.

"above" ($\cos\theta_{12} > 0$) or "below" ($\cos\theta_{12} < 0$) particle i. In this sense, the binary mixture obtained in this way is "quasi", and not "fully", spherically symmetric.

Another important point to be stressed is that, while the *sign* of $\cos\theta_{12}$ represents the only source of anisotropy in the above potential $\phi_{ij}(\mathbf{r}_{12})$, this is *not* the case for the corresponding correlation functions, which will explicitly depend upon the relative orientation $\cos\theta_{12}$ and not only upon its sign. This applies, for instance, to the pair correlation functions $g_{ij}(\mathbf{r}) = g_{ij}(r;\theta)$, as shown in Appendix

C to first order in density in the sticky limit (see Sec. 3.4). As an illustration, Fig. 3.3 shows the first-order pair correlation functions $g_{11}^{(1)}(\mathbf{r})$ and $g_{12}^{(1)}(\mathbf{r})$ as functions of the radial distance r for several orientations θ. Since in the one dimensional case either $\theta = 0$ or $\theta = \pi$, a true dependence on the orientation angle θ was absent.

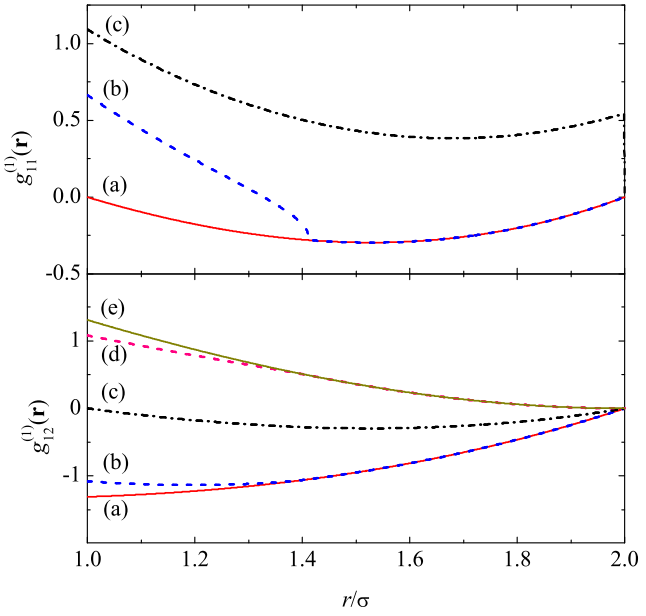

FIGURE 3.3: (Top) Plot of $g_{11}^{(1)}(\mathbf{r})$ as a function of r for (a) $\theta = 0$ and π, (b) $\theta = \frac{\pi}{4}$ and $\frac{3\pi}{4}$, and (c) $\theta = \frac{\pi}{2}$. (Bottom) Plot of the regular part of $g_{12}^{(1)}(\mathbf{r})$ as a function of r for (a) $\theta = 0$, (b) $\theta = \frac{\pi}{4}$, (c) $\theta = \frac{\pi}{2}$, (d) $\theta = \frac{3\pi}{4}$, and (e) $\theta = \pi$. The interaction potential is given by Eq. (3.6) (sketched in Fig. 3.2), except that the sticky limit with Baxter's temperature $\tau = 0.1$ has been taken (see Sec. 3.4).

As our aim is to remove the orientational dependence in the original potential altogether, a further simplification is required to reduce the problem to a simple binary mixture having *asymmetric* correlation functions dependent only on distances and not on orientations of spheres. This will be the orientational average discussed in Sec. 3.3.

3.3 Orientational average and thermodynamics

3.3.1 Orientational average

Most of the content of this section applies to a mixture (with any number of components) characterized by any anisotropic potential $\phi_{ij}(\mathbf{r}) = \phi_{ji}(-\mathbf{r})$ exhibiting the quasi-isotropic form (3.5), where, in general $\varphi_{ij}(r) \neq \varphi_{ji}(r)$ if $i \neq j$. In that case, we note that the thermodynamic quantities will generally involve integrals of the general form

$$I_{ij} = \int d\mathbf{r}\, g_{ij}(\mathbf{r}) \mathcal{F}_{ij}(\mathbf{r}) \tag{3.7}$$

with

$$\mathcal{F}_{ij}(\mathbf{r}) = F_{ij}(r)\Theta(\cos\theta) + F_{ji}(r)\Theta(-\cos\theta), \tag{3.8}$$

where in general $F_{ij}(r) \neq F_{ji}(r)$ if $i \neq j$. This strongly suggests that one can define the two orientational *averages* $g_{ij}^{+}(r)$ and $g_{ij}^{-}(r)$ as

$$g_{ij}^{+}(r) \equiv \overline{g}_{ij}(r) = \int_0^1 d(\cos\theta)\, g_{ij}(\mathbf{r}), \tag{3.9a}$$

$$g_{ij}^{-}(r) \equiv \overline{g}_{ji}(r) = \int_{-1}^0 d(\cos\theta)\, g_{ij}(\mathbf{r}). \tag{3.9b}$$

Note that $g_{ij}^{-}(r) = g_{ji}^{+}(r)$, and this suggests the use of the notation $\overline{g}_{ij}(r)$ and $\overline{g}_{ji}(r)$ instead of $g_{ij}^{+}(r)$ and $g_{ij}^{-}(r)$, respectively. Taking into account Eqs. (3.8)–(3.9b), Eq. (3.7) becomes

$$I_{ij} = \frac{1}{2}\int d\mathbf{r}\, \left[\overline{g}_{ij}(r)F_{ij}(r) + \overline{g}_{ji}(r)F_{ji}(r)\right]. \tag{3.10}$$

In the case of a double summation over i and j,

$$\sum_{i,j} x_i x_j I_{ij} = \sum_{i,j} x_i x_j \int d\mathbf{r}\, \overline{g}_{ij}(r)F_{ij}(r), \tag{3.11}$$

where x_i denotes the mole fraction of species i.

3.3.2 Thermodynamics of the mixture: energy, virial, and compressibility routes

We can now particularize the general result (3.11) to specific cases.

In the case of the internal energy, $\mathcal{F}_{ij}(\mathbf{r}) = \phi_{ij}(\mathbf{r})$ and so the energy equation of state can be written as [30, 56]

$$\begin{aligned} u_{\text{ex}} &= \frac{1}{2}\rho \sum_{i,j} x_i x_j \int d\mathbf{r}\, g_{ij}(\mathbf{r})\, \phi_{ij}(\mathbf{r}) \\ &= \frac{1}{2}\rho \sum_{i,j} x_i x_j \int d\mathbf{r}\, \overline{y}_{ij}(r)\, \varphi_{ij}(r) e^{-\beta\varphi_{ij}(r)}, \end{aligned} \tag{3.12}$$

where, as defined in Ch. 2, u_{ex} is the excess internal energy per particle, ρ is the number density, $\beta = 1/k_B T$ (k_B and T being the Boltzmann constant and the temperature, respectively), and $\overline{y}_{ij}(r) \equiv \overline{g}_{ij}(r) e^{\beta\varphi_{ij}(r)}$ is the orientational average of the cavity function $y_{ij}(\mathbf{r}) \equiv g_{ij}(\mathbf{r}) e^{\beta\phi_{ij}(\mathbf{r})}$.

A similar result holds for the virial route to the equation of state,

$$\begin{aligned} Z &\equiv \frac{p}{\rho k_B T} \\ &= 1 + \frac{1}{6}\rho \sum_{i,j} x_i x_j \int d\mathbf{r}\, y_{ij}(\mathbf{r})\, \mathbf{r}\cdot\nabla e^{-\beta\phi_{ij}(\mathbf{r})}, \end{aligned} \tag{3.13}$$

where p is the pressure. First, note that

$$\begin{aligned} \nabla\phi_{ij}(\mathbf{r}) &= \left[\frac{d\varphi_{ij}(r)}{dr}\Theta(\cos\theta) + \frac{d\varphi_{ji}(r)}{dr}\Theta(-\cos\theta)\right]\widehat{\mathbf{r}} \\ &\quad -\delta(z)\left[\varphi_{ij}(r) - \varphi_{ji}(r)\right]\widehat{\mathbf{z}}. \end{aligned} \tag{3.14}$$

Therefore,

$$\mathbf{r}\cdot\nabla\phi_{ij}(\mathbf{r}) = r\left[\frac{d\varphi_{ij}(r)}{dr}\Theta(\cos\theta) + \frac{d\varphi_{ji}(r)}{dr}\Theta(-\cos\theta)\right], \tag{3.15}$$

and thus

$$Z = 1 + \frac{1}{6}\rho \sum_{i,j} x_i x_j \int d\mathbf{r}\, \overline{y}_{ij}(r)\, r \frac{d}{dr} e^{-\beta\varphi_{ij}(r)}. \tag{3.16}$$

Finally, let us consider the compressibility route. In a mixture, the (dimensionless) isothermal compressibility χ_T is in general given by

$$\begin{aligned} \chi_T^{-1} &= \frac{1}{k_B T}\left(\frac{\partial p}{\partial \rho}\right)_{T,\{x_j\}} \\ &= \sum_{i,j} \sqrt{x_i x_j}\left[\mathsf{I} + \widehat{\mathsf{h}}(0)\right]^{-1}_{ij}, \end{aligned} \tag{3.17}$$

where $\widehat{h}_{ij}(0)$ is proportional to the zero wavenumber limit of the Fourier transform of the total correlation function $h_{ij}(\mathbf{r}) = g_{ij}(\mathbf{r}) - 1$, namely

$$\begin{aligned} \widehat{h}_{ij}(0) &= \rho\sqrt{x_i x_j} \int d\mathbf{r}\, h_{ij}(\mathbf{r}) \\ &= \frac{\rho\sqrt{x_i x_j}}{2} \int d\mathbf{r}\, \left[\overline{h}_{ij}(r) + \overline{h}_{ji}(r)\right]. \end{aligned} \tag{3.18}$$

In the specific case of a binary mixture considered here, Eq. (3.17) becomes

$$\chi_T^{-1} = \frac{1 + x_2\widehat{h}_{11}(0) + x_1\widehat{h}_{22}(0) - 2\sqrt{x_1 x_2}\widehat{h}_{12}(0)}{\left[1 + \widehat{h}_{11}(0)\right]\left[1 + \widehat{h}_{22}(0)\right] - \widehat{h}_{12}^2(0)}. \tag{3.19}$$

Equations (3.12), (3.16), (3.17), and (3.18) confirm that the knowledge of the two average quantities $\overline{g}_{ij}(r)$ and $\overline{g}_{ji}(r)$ for each pair ij suffices to determine the thermodynamic quantities. In fact, Eqs. (3.12), (3.16), (3.17), and (3.18) are formally indistinguishable from those corresponding to mixtures with standard isotropic interactions, except that in our case one generally has $\varphi_{ij}(r) \neq \varphi_{ji}(r)$ and, consequently, $\overline{g}_{ij}(r) \neq \overline{g}_{ji}(r)$.

For future convenience, it is expedient to introduce the Laplace transform of $r\overline{g}_{ij}(r)$:

$$G_{ij}(s) \;=\; \int_0^\infty dr\, e^{-sr} r\overline{g}_{ij}(r). \tag{3.20}$$

Its small-s behavior is of the form [54]

$$s^2 G_{ij}(s) \;=\; 1 + H_{ij}^{(0)} s^2 + H_{ij}^{(1)} s^3 + \cdots, \tag{3.21}$$

where

$$H_{ij}^{(n)} \equiv \int_0^\infty dr\, (-r)^n r\overline{h}_{ij}(r). \tag{3.22}$$

Thus, Eq. (3.18) becomes

$$\widehat{h}_{ij}(0) = -2\pi\rho\sqrt{x_i x_j}\left[H_{ij}^{(1)} + H_{ji}^{(1)}\right]. \tag{3.23}$$

Note that Eq. (3.21) implies

$$\lim_{s\to 0} s^2 G_{ij}(s) = 1, \qquad \lim_{s\to 0} \frac{s^2 G_{ij}(s) - 1}{s} = 0. \tag{3.24}$$

3.4 The sticky limit

The mapping of the Kern–Frenkel potential with fixed patch orientation along the $\pm\widehat{\mathbf{z}}$ axis onto a binary mixture represents a considerable simplification. On the other hand, no approximation is involved in this mapping.

The presence of the original SW interactions for the radial part [see Eq. (3.3)] makes the analytical treatment of the problem a formidable task. Progresses can however be made by considering the Baxter SHS limit, for which a well defined approximate scheme of solution is available in the *isotropic* case for both one-component [32] and multi-component [47, 48, 49, 50, 51] fluids. The discussion

reported below closely follows the analogue for Baxter symmetric mixtures [48, 49].

Let us start by rewriting Eq. (3.6) as

$$\varphi_{ij}(r) = \begin{cases} \infty, & r < \sigma, \\ -\epsilon_{ij}, & \sigma < r < \lambda\sigma, \\ 0, & r > \lambda\sigma, \end{cases} \tag{3.25}$$

where $\epsilon_{11} = \epsilon_{22} = \epsilon_{21} = 0$ and $\epsilon_{12} = \epsilon > 0$. However, in this section we will assume generic energy scales ϵ_{ij}. In that case, the virial equation of state (3.16) becomes

$$Z = 1 + 4\eta\overline{y}(\sigma) - 12\eta \sum_{i,j} x_i x_j t_{ij} \frac{\lambda^3 \overline{y}_{ij}(\lambda\sigma) - \overline{y}_{ij}(\sigma)}{\lambda^3 - 1}, \tag{3.26}$$

where $\eta \equiv \frac{\pi}{6}\rho\sigma^3$ is the packing fraction,

$$\overline{y}(r) = \sum_{i,j} x_i x_j \overline{y}_{ij}(r) \tag{3.27}$$

is the orientational average *global* cavity function, and

$$t_{ij} \equiv \frac{1}{12\tau_{ij}} \equiv \frac{1}{3}\left(\lambda^3 - 1\right)\left(e^{\beta\epsilon_{ij}} - 1\right) \tag{3.28}$$

is a parameter measuring the degree of "stickiness" of the SW interaction $\varphi_{ij}(r)$. This parameter will be used later on to connect results from numerical simulations of the actual Janus fluid with analytical results derived for asymmetric SHS mixtures. Although Baxter's temperature parameters τ_{ij} are commonly used in the literature, we will employ the inverse temperature parameters $t_{ij} = 1/12\tau_{ij}$ in most of the mathematical expressions.

In the case of the interaction potential (3.25), the energy equation of state (3.12) reduces to

$$u_{\text{ex}} = -12\frac{\eta}{\sigma^3} \sum_{i,j} x_i x_j \epsilon_{ij} e^{\beta\epsilon_{ij}} \int_{\sigma}^{\lambda\sigma} dr\, r^2 \overline{y}_{ij}(r). \tag{3.29}$$

The compressibility equation of state (3.17) does not simplify for the SW interaction.

Since the (orientational average) cavity function $\overline{y}_{ij}(r)$ must be continuous, it follows that

$$\overline{g}_{ij}(r) = \overline{y}_{ij}(r)\left[e^{\beta\epsilon_{ij}}\Theta(r-\sigma) - \left(e^{\beta\epsilon_{ij}}-1\right)\Theta(r-\lambda\sigma)\right]. \tag{3.30}$$

Following Baxter's prescription [32], we now consider the SHS limit

$$\lambda \to 1, \quad \epsilon_{ij} \to \infty, \quad t_{ij} \equiv \frac{1}{12\tau_{ij}} \to (\lambda-1)e^{\beta\epsilon_{ij}} = \text{finite}, \tag{3.31}$$

so that the well (3.25) becomes infinitely deep and narrow and can be described by a single (inverse) stickiness parameter τ_{ij}. Note that in the present Janus case ($\epsilon_{11} = \epsilon_{22} = \epsilon_{21} = 0$, $\epsilon_{12} = \epsilon > 0$) one actually has $t_{11} = t_{22} = t_{21} = 0$ and $t_{12} = t = 1/12\tau$.

In the SHS limit (3.31), Eqs. (3.26), (3.29), and (3.30) become, respectively,

$$Z = 1 + 4\eta\overline{y}(\sigma) - 4\eta\sum_{i,j} x_i x_j t_{ij}\left[3\overline{y}_{ij}(\sigma) + \sigma\overline{y}'_{ij}(\sigma)\right], \tag{3.32a}$$

$$u_{\text{ex}} = -12\eta\sum_{i,j} x_i x_j \epsilon_{ij} t_{ij}\overline{y}_{ij}(\sigma), \tag{3.32b}$$

$$\overline{g}_{ij}(r) = \overline{y}_{ij}(r)\left[\Theta(r-\sigma) + t_{ij}\sigma\delta_+(r-\sigma)\right]. \tag{3.32c}$$

In Eq. (3.32a), $\overline{y}'_{ij}(\sigma)$ must be interpreted as $\lim_{\lambda\to 1}\frac{d}{dr}\overline{y}_{ij}(r)\big|_{r=\sigma}$, which in principle differs from $\frac{d}{dr}\lim_{\lambda\to 1}\overline{y}_{ij}(r)\big|_{r=\sigma}$ [58]. However, both quantities coincide in the one-dimensional case [58] and are expected to coincide in the three-dimensional case as well. This is just a consequence of the expected continuity of $\frac{d}{dr}\overline{y}_{ij}(r)$ at $r = \lambda\sigma$ in the SW case [59].

Thermodynamic consistency between the virial and energy routes implies

$$\rho\frac{\partial u_{\rm ex}}{\partial\rho}=\frac{\partial Z}{\partial\beta}=\sum_{i,j}\epsilon_{ij}t_{ij}\frac{\partial Z}{\partial t_{ij}}. \tag{3.33}$$

Using Eqs. (3.32a) and (3.32b) and equating the coefficients of ϵ_{ij} in both sides, the consistency condition (3.33) yields

$$\begin{aligned} x_ix_j\left[\sigma\overline{y}'_{ij}(\sigma)-3\eta\frac{\partial\overline{y}_{ij}(\sigma)}{\partial\eta}\right] &= \sum_{k,\ell}x_kx_\ell\left\{\frac{\partial\overline{y}_{k\ell}(\sigma)}{\partial t_{ij}}\right. \\ &\left.-t_{k\ell}\frac{\partial}{\partial t_{ij}}\left[3\overline{y}_{k\ell}(\sigma)+\sigma\overline{y}'_{k\ell}(\sigma)\right]\right\}. \end{aligned} \tag{3.34}$$

For distances $r\gtrsim\sigma$, the orientational averages of the cavity functions can be Taylor expanded as

$$\Theta(r-\sigma)\overline{y}_{ij}(r)=\Theta(r-\sigma)\left[\overline{y}_{ij}(\sigma)+\overline{y}'_{ij}(\sigma)(r-\sigma)+\cdots\right]. \tag{3.35}$$

Hence, if we denote by $Y_{ij}(s)$ the Laplace transform of $\Theta(r-\sigma)r\overline{y}_{ij}(r)$, Eq. (3.35) yields for large s

$$e^{\sigma s}sY_{ij}(s)=\sigma\overline{y}_{ij}(\sigma)+\left[\overline{y}_{ij}(\sigma)+\sigma\overline{y}'_{ij}(\sigma)\right]s^{-1}+\cdots. \tag{3.36}$$

According to Eqs. (3.20) and (3.32c), the relationship between the Laplace function $G_{ij}(s)$ and $Y_{ij}(s)$ is

$$G_{ij}(s) = Y_{ij}(s)+\sigma^2t_{ij}\overline{y}_{ij}(\sigma)e^{-\sigma s}. \tag{3.37}$$

Inserting Eq. (3.36) into Eq. (3.37), we obtain the following large-s behavior of $G_{ij}(s)$:

$$e^{\sigma s}G_{ij}(s)=\sigma^2t_{ij}\overline{y}_{ij}(\sigma)+\sigma\overline{y}_{ij}(\sigma)s^{-1}+\left[\overline{y}_{ij}(\sigma)+\sigma\overline{y}'_{ij}(\sigma)\right]s^{-2}+\mathcal{O}(s^{-3}). \tag{3.38}$$

A consequence of this is

$$\frac{\lim_{s\to\infty} e^{\sigma s} G_{ij}(s)}{\lim_{s\to\infty} s\left[e^{\sigma s} G_{ij}(s) - \lim_{s\to\infty} e^{\sigma s} G_{ij}(s)\right]} = \sigma t_{ij}. \tag{3.39}$$

3.5 A heuristic, non-perturbative analytical theory

3.5.1 A simple approximate scheme within the Percus–Yevick closure

The Ornstein–Zernike (OZ) equation for an anisotropic mixture reads [30]

$$\begin{aligned} h_{ij}(\mathbf{r}_{12}) &= c_{ij}(\mathbf{r}_{12}) + \rho \sum_k x_k \int d\mathbf{r}_3\, h_{ik}(\mathbf{r}_{13}) c_{kj}(\mathbf{r}_{32}) \\ &= c_{ij}(\mathbf{r}_{12}) + \rho \sum_k x_k \int d\mathbf{r}_3\, c_{ik}(\mathbf{r}_{13}) h_{kj}(\mathbf{r}_{32}), \end{aligned} \tag{3.40}$$

where $c_{ij}(\mathbf{r})$ is the direct correlation function. The PY closure reads

$$c_{ij}(\mathbf{r}) = g_{ij}(\mathbf{r})\left[1 - e^{\beta\phi_{ij}(\mathbf{r})}\right]. \tag{3.41}$$

Introducing the averages $c_{ij}^{+}(r) = \overline{c}_{ij}(r)$ and $c_{ij}^{-}(r) = \overline{c}_{ji}(r)$ for $c_{ij}(\mathbf{r})$ in a way similar to Eqs. (3.9a) and (3.9b), Eq. (3.41) yields

$$\overline{c}_{ij}(r) = \overline{g}_{ij}(r)\left[1 - e^{\beta\varphi_{ij}(r)}\right]. \tag{3.42}$$

Thus, the PY closure for the full correlation functions $c_{ij}(\mathbf{r})$ and $g_{ij}(\mathbf{r})$ translates into an equivalent relation for the orientational average functions $\overline{c}_{ij}(r)$ and $\overline{g}_{ij}(r)$. A similar reasoning, on the other hand, is not valid for the OZ relation. Multiplying both sides of the first equality in Eq. (3.40) by $\Theta(\cos\theta_{12})$ and integrating over

$\cos\theta_{12}$ one gets

$$\overline{h}_{ij}(r_{12}) \;=\; \overline{c}_{ij}(r_{12}) + \rho \sum_k x_k \int d\mathbf{r}_3 \int_0^1 d\,(\cos\theta_{12}) h_{ik}(\mathbf{r}_{13}) c_{kj}(\mathbf{r}_{32}). \quad (3.43)$$

The same result is obtained if we start from the second equality in Eq. (3.40), multiply by $\Theta(-\cos\theta_{12})$, integrate over $\cos\theta_{12}$, and make the changes $\mathbf{r}_{12} \to -\mathbf{r}_{12}$, $\mathbf{r}_{13} \to -\mathbf{r}_{13}$, and $i \leftrightarrow j$. Equation (3.43) shows that in the case of anisotropic potentials of the form (3.5) the OZ equation does not reduce to a closed equation involving the averages $\overline{h}_{ij}(r)$ and $\overline{c}_{ij}(r)$ only, as remarked.

In order to obtain a closed theory, we adopt the *heuristic* mean-field decoupling approximation

$$\int d\mathbf{r}_3 \int_0^1 d\,(\cos\theta_{12})\; h_{ik}(\mathbf{r}_{13}) c_{kj}(\mathbf{r}_{32}) \to \int d\mathbf{r}_3\, \overline{h}_{ik}\,(r_{13}) \overline{c}_{kj}\,(r_{32}). \quad (3.44)$$

Under these conditions, the true OZ relation (3.43) is replaced by the pseudo-OZ relation

$$\overline{h}_{ij}(r_{12}) = \overline{c}_{ij}(r_{12}) + \rho \sum_k x_k \int d\mathbf{r}_3\, \overline{h}_{ik}(r_{13}) \overline{c}_{kj}(r_{32}). \quad (3.45)$$

This can then be closed by the PY equation (3.42) and standard theory applies. An alternative and equivalent view is to consider $\overline{c}_{ij}(r)$ not as the orientational average of the true direct correlation function $c_{ij}(\mathbf{r})$ but as exactly defined by Eq. (3.45). Within this interpretation, Eq. (3.42) then represents a pseudo-PY closure not derivable from the true PY closure (3.41).

Within the above interpretation, it is then important to bear in mind that the functions $\overline{g}_{ij}(r)$ obtained from the solution of a combination of Eqs. (3.42) and (3.45) are *not* equivalent to the orientational averages of the functions $g_{ij}(\mathbf{r})$ obtained from the solution of the true PY problem posed by Eqs. (3.40) and complemented by the PY condition (3.41). As a consequence, the solutions to Eqs. (3.42) and (3.45) are *not* expected to provide the exact $\overline{g}_{ij}(r)$ to first order in ρ, in contrast to the true PY problem. This is an interesting nuance that will be further discussed in Sec. 3.5.3.3.

The main advantage of the approximate OZ relation (3.45) in the case of anisotropic interactions of the form (3.5) is that it allows to transform the obtention of an *anisotropic* function $g_{ij}(\mathbf{r})$, but *symmetric* in the sense that $g_{ij}(\mathbf{r}) = g_{ji}(-\mathbf{r})$, into the obtention of an *isotropic* function $\overline{g}_{ij}(r)$, but *asymmetric* since $\overline{g}_{ij}(r) \neq \overline{g}_{ji}(r)$. In the case of the anisotropic SHS potential defined above, we can exploit the known solution of the PY equation for *isotropic* SHS mixtures to construct the solution of the set made of Eqs. (3.42) and (3.45). This is done in Sec. 3.5.2 by following the RFA methodology.

3.5.2 RFA method for SHS

Henceforth, for the sake of simplicity, we take $\sigma = 1$ as length unit. The aim of this section is to extend the RFA approximation proposed for symmetric SHS mixtures [53, 54] to the asymmetric case.

We start with the one-component case [58]. Let us introduce an auxiliary function $F(s)$ related to the Laplace transform $G(s)$ of $rg(r)$ by

$$G(s) = \frac{1}{2\pi} \frac{se^{-s}}{F(s) + \rho e^{-s}}. \tag{3.46}$$

The next step is to approximate $F(s)$ by a *rational function*,

$$F(s) = \frac{S(s)}{L(s)}, \tag{3.47}$$

with $S(s) = S^{(0)} + S^{(1)}s + S^{(2)}s^2 + s^3$ and

$$L(s) = L^{(0)} + L^{(1)}s + L^{(2)}s^2. \tag{3.48}$$

Note that $\lim_{s\to\infty} F(s)/s = 1/L^{(2)} =$ finite, so that $\lim_{s\to\infty} e^s G(s) =$ finite, in agreement with Eq. (3.38). Furthermore, Eq. (3.24) requires $F(s) + \rho e^{-s} = \mathcal{O}(s^3)$, so that $S^{(0)} = -\rho L^{(0)}$, $S^{(1)} = \rho\left(L^{(0)} - L^{(1)}\right)$, $S^{(2)} = \rho\left(L^{(1)} - \frac{1}{2}L^{(0)} - L^{(2)}\right)$.

Taking all of this into account, Eq. (3.46) can be rewritten as

$$G(s) = \frac{e^{-s}}{2\pi s^2}\frac{L(s)}{1-A(s)}, \tag{3.49}$$

where

$$A(s) = \frac{\rho}{s^3}\left[(1-e^{-s})L(s) - L^{(0)}s + \left(\frac{1}{2}L^{(0)} - L^{(1)}\right)s^2\right]. \tag{3.50}$$

In the case of a mixture, $G(s)$, $L(s)$, and $A(s)$ become matrices and Eq. (3.49) is generalized as

$$G_{ij}(s) \;=\; \frac{e^{-s}}{2\pi s^2}\left(\mathsf{L}(s)\cdot[\mathsf{I}-\mathsf{A}(s)]^{-1}\right)_{ij}, \tag{3.51}$$

where I is the identity matrix and

$$L_{ij}(s) = L_{ij}^{(0)} + L_{ij}^{(1)}s + L_{ij}^{(2)}s^2, \tag{3.52a}$$

$$A_{ij}(s) = \rho\frac{x_i}{s^3}\left[(1-e^{-s})L_{ij}(s) - L_{ij}^{(0)}s + \left(\frac{1}{2}L_{ij}^{(0)} - L_{ij}^{(1)}\right)s^2\right]. \tag{3.52b}$$

Note that $\lim_{s\to 0} A_{ij}(s) = \text{finite}$, so that $\lim_{s\to 0} s^2 G_{ij}(s) = \text{finite} \neq 0$ by construction. Analogously, $\lim_{s\to\infty} e^s G_{ij}(s) = \text{finite}$ also by construction.

The coefficients $L_{ij}^{(0)}$, $L_{ij}^{(1)}$, and $L_{ij}^{(2)}$ are determined by enforcing the exact conditions (3.24) and (3.39). The details of the derivation are presented in Appendix D and here we present the final results. The coefficients $L_{ij}^{(0)}$ and $L_{ij}^{(1)}$ do not depend upon the first index i and can be expressed as linear functions of the coefficients $\{L_{kj}^{(2)}\}$:

$$L_{ij}^{(0)} \;=\; 2\pi\frac{1+2\eta}{(1-\eta)^2} - \frac{12\eta}{1-\eta}\sum_k x_k L_{kj}^{(2)}, \tag{3.53a}$$

$$L_{ij}^{(1)} \;=\; 2\pi\frac{1+\eta/2}{(1-\eta)^2} - \frac{6\eta}{1-\eta}\sum_k x_k L_{kj}^{(2)}, \tag{3.53b}$$

and the coefficients $L_{ij}^{(2)}$ obey the closed set of quadratic equations

$$\frac{L_{ij}^{(2)}}{t_{ij}} = 2\pi\frac{1+\eta/2}{(1-\eta)^2} - \frac{6\eta}{1-\eta}\sum_k x_k\left(L_{ik}^{(2)}+L_{kj}^{(2)}\right) + \frac{6}{\pi}\eta\sum_k x_k L_{ik}^{(2)}L_{kj}^{(2)}. \quad (3.54)$$

This closes the problem. Once $L_{ij}^{(2)}$ are known, the contact values are given by

$$\overline{y}_{ij}(1) = \frac{L_{ij}^{(2)}}{2\pi t_{ij}}. \quad (3.55)$$

Although here we have taken into account that all the diameters are equal ($\sigma_{ij}=\sigma=1$), the above scheme can be easily generalized to the case of different diameters with the additive rule $\sigma_{ij}=(\sigma_i+\sigma_j)/2$. For symmetric interactions (i.e., $t_{ij}=t_{ji}$) one recovers the PY solution of SHS mixtures for any number of components [51, 53]. It is shown in Appendix E that the pair correlation functions $\overline{g}_{ij}(r)$ derived here are indeed the solution to the PY-like problem posed by Eqs. (3.42) and (3.45).

3.5.3 Case of interest: $t_{11}=t_{22}=t_{21}=0$

In the general scheme described by Eqs. (3.51)–(3.55), four different stickiness parameters (t_{11}, t_{12}, t_{21}, and t_{22}) are in principle possible. With the convention that in t_{ij} the particle of species i is always located *below* the particle of species j, we might consider the simplest possibility of having only one SHS interaction $t_{12}=t=1/12\tau$ and all other HS interactions ($t_{11}=t_{22}=t_{21}=0$), as illustrated in Fig. 3.2. This is clearly an intermediate case between a full SHS model ($t_{ij}=t=1/12\tau$) and a full HS model ($t_{ij}=0$), with a predominance of repulsive HS interactions with respect to attractive SHS interactions. This is meant to model the intermediate nature of the original anisotropic Kern–Frenkel potential that interpolates between a SW and a HS isotropic potentials upon decreasing the coverage, that is, the fraction of the SW surface patch with respect to the full surface of the sphere.

3.5.3.1 Structural properties

If $t_{11} = t_{22} = t_{21} = 0$, Eq. (3.54) implies $L_{11}^{(2)} = L_{22}^{(2)} = L_{21}^{(2)} = 0$. As a consequence, Eq. (3.54) for $i = 1$ and $j = 2$ yields a *linear* equation for $L_{12}^{(2)}$ whose solution is

$$L_{12}^{(2)} = 2\pi \frac{1+\eta/2}{1-\eta} \frac{t}{1-\eta+6\eta t}. \tag{3.56}$$

According to Eq. (3.55),

$$\overline{y}_{12}(1) = \frac{1+\eta/2}{(1-\eta)^2} \left(1 - \frac{6\eta t}{1-\eta+6\eta t}\right). \tag{3.57}$$

Next, Eqs. (3.53a) and (3.53b) yield

$$\frac{L_{11}^{(0)}}{2\pi} = \frac{L_{21}^{(0)}}{2\pi} = \frac{1+2\eta}{(1-\eta)^2}, \tag{3.58a}$$

$$\frac{L_{12}^{(0)}}{2\pi} = \frac{L_{22}^{(0)}}{2\pi} = \frac{1+2\eta}{(1-\eta)^2} - \frac{12\eta t}{1-\eta} x_1 \overline{y}_{12}(1), \tag{3.58b}$$

$$\frac{L_{11}^{(1)}}{2\pi} = \frac{L_{21}^{(1)}}{2\pi} = \frac{1+\eta/2}{(1-\eta)^2}, \tag{3.58c}$$

$$\frac{L_{12}^{(1)}}{2\pi} = \frac{L_{22}^{(1)}}{2\pi} = \frac{1+\eta/2}{(1-\eta)^2} - \frac{6\eta t}{1-\eta} x_1 \overline{y}_{12}(1). \tag{3.58d}$$

Once the functions $L_{ij}(s)$ are fully determined, Eq. (3.51) provides the Laplace transforms $G_{ij}(s)$. From Eq. (3.37) it follows that $Y_{11}(s) = G_{11}(s)$, $Y_{22}(s) = G_{22}(s)$, $Y_{21}(s) = G_{21}(s)$, and

$$Y_{12}(s) = G_{12}(s) - t\overline{y}_{12}(1) e^{-s}. \tag{3.59}$$

A numerical inverse Laplace transform [60] allows one to obtain $\overline{g}_{11}(r)$, $\overline{g}_{22}(r)$, $\overline{g}_{21}(r)$, and $\overline{y}_{12}(r)$ for any packing fraction η, stickiness parameter $t = 1/12\tau$, and mole fraction x_1. In what follows, we will omit explicit expressions related to $\overline{g}_{22}(r)$ since they can be readily obtained from $\overline{g}_{11}(r)$ by the exchange $x_1 \leftrightarrow x_2$.

The contact values $\overline{g}_{ij}(1^+) = \overline{y}_{ij}(1)$ with $(i,j) \neq (1,2)$ cannot be obtained from Eq. (3.55), unless the associated t_{ij} are first assumed to be nonzero and then the limit $t_{ij} \to 0$ is taken. A more direct method is to realize that, if $t_{ij} = 0$, Eq. (3.38) gives

$$\overline{g}_{ij}(1^+) = \lim_{s\to\infty} e^s s G_{ij}(s), \quad (i,j) \neq (1,2). \tag{3.60}$$

The results are

$$\overline{g}_{11}(1^+) = \overline{y}_{11}(1) = \frac{1+\eta/2}{(1-\eta)^2} - x_2 \frac{6\eta t}{1-\eta} \overline{y}_{12}(1), \tag{3.61a}$$

$$\overline{g}_{21}(1^+) = \overline{y}_{21}(1) = \frac{1+\eta/2}{(1-\eta)^2}, \tag{3.61b}$$

$$\overline{y}(1) = \frac{1+\eta/2}{(1-\eta)^2} \left(1 - x_1 x_2 \frac{12\eta t}{1-\eta+6\eta t}\right). \tag{3.61c}$$

It is interesting to note the property $\overline{g}_{11}(1^+) + \overline{g}_{22}(1^+) = \overline{y}_{12}(1) + \overline{g}_{21}(1^+)$.

To obtain the equation of state from the virial route we will need the derivative $\overline{y}'_{12}(1)$. Expanding $e^s G_{12}(s)$ in powers of s^{-1} and using Eq. (3.38), one gets

$$\frac{\overline{y}'_{12}(1)}{\overline{y}_{12}(1)} = \frac{\eta}{(1-\eta)^2} \left[3t \left(\frac{2-4\eta-7\eta^2}{1+\eta/2} + 12 x_1 x_2 \eta\right) - \frac{9}{2} \frac{1-\eta^2}{1+\eta/2}\right]. \tag{3.62}$$

3.5.3.2 Thermodynamic properties

Virial route. According to Eq. (3.32a),

$$\begin{aligned} Z^v &= 1 + 4\eta \overline{y}(1) - 4 x_1 x_2 \eta t \left[3\overline{y}_{12}(1) + \overline{y}'_{12}(1)\right] \\ &= Z^v_{\text{HS}} - 4 x_1 x_2 \eta t \left[3 \frac{1+3\eta}{1-\eta} \overline{y}_{12}(1) + \overline{y}'_{12}(1)\right], \end{aligned} \tag{3.63}$$

where the superscript v denotes the virial route and

$$Z^v_{\text{HS}} = \frac{1+2\eta+3\eta^2}{(1-\eta)^2} \tag{3.64}$$

is the HS compressibility factor predicted by the virial route in the PY approximation.

Energy route. From Eq. (3.32b) we have

$$\frac{u_{\rm ex}}{\epsilon} = -12x_1x_2\eta t\overline{y}_{12}(1). \tag{3.65}$$

The compressibility factor can be obtained from $u_{\rm ex}$ via the thermodynamic relation (3.33), which in our case reads

$$\eta\frac{\partial u_{\rm ex}/\epsilon}{\partial\eta} = \frac{1}{\epsilon}\frac{\partial Z}{\partial\beta} = t\frac{\partial Z}{\partial t}. \tag{3.66}$$

Thus, the compressibility factor derived from the energy route is

$$\begin{aligned} Z^u &= Z^u_{\rm HS} + \eta\frac{\partial}{\partial\eta}\int_0^t dt'\frac{u_{\rm ex}(\eta,t')/\epsilon}{t'} \\ &= Z^u_{\rm HS} - 3x_1x_2\frac{\eta}{1-\eta}\left[4t\overline{y}_{12}(1) + \frac{\ln\left(1+\frac{6\eta t}{1-\eta}\right)}{1-\eta}\right], \end{aligned} \tag{3.67}$$

where $Z^u_{\rm HS}$ plays the role of an integration constant and thus it can be chosen arbitrarily. It can be shown [61, 62] that the energy and the virial routes coincide when the HS system is the limit of a square-shoulder interaction with vanishing shoulder width. From that point of view one should take $Z^u_{\rm HS} = Z^v_{\rm HS}$ in Eq. (3.67). On the other hand, a better description is expected from the Carnahan–Starling (CS) equation of state [63]

$$Z^{\rm CS}_{\rm HS} = \frac{1+\eta+\eta^2-\eta^3}{(1-\eta)^3} \tag{3.68}$$

Henceforth we will take $Z^u_{\rm HS} = Z^{\rm CS}_{\rm HS}$.

Compressibility route. Expanding $s^2G_{ij}(s)$ in powers of s it is straightforward to obtain $H^{(1)}_{ij}$ from Eq. (3.21). This allows one to use Eqs. (3.19) and (3.23) to get the inverse susceptibility χ_T^{-1} as

$$\chi_T^{-1} = \frac{1+2\eta}{(1-\eta)^4}\frac{1+2\eta-24x_1x_2t\eta(1-\eta)\overline{y}_{12}(1)}{1-x_1x_2\left[\frac{12t\eta(1+\eta/2)\overline{y}_{12}(1)}{1+2\eta+36x_1x_2t\eta^2\overline{y}_{12}(1)}\right]^2}, \tag{3.69}$$

that, for an equimolar mixture ($x_1 = x_2 = \frac{1}{2}$), reduces to

$$\chi_T^{-1} = \frac{\left[(1-\eta)^2(1+2\eta) + 3\eta t\left(2 + 5\eta - \frac{5}{2}\eta^2\right)\right]^2}{(1-\eta)^5(1-\eta+6\eta t)\left[(1-\eta)^2 + 3\eta t(4-\eta)\right]}. \tag{3.70}$$

The associated compressibility factor is then

$$Z^c = \frac{1}{\eta}\int_0^\eta d\eta'\, \chi_T^{-1}(\eta'). \tag{3.71}$$

The above integral has an analytical solution, but it is too cumbersome to be displayed here.

3.5.3.3 Low-density expansion

In the standard case of SHS mixtures with symmetric coefficients in the potential parameters, the PY closure is known to reproduce the exact cavity functions to first order in density and thus the third virial coefficient (see Appendix C.2). However, this needs not be the case in the RFA description for the present asymmetric case, as further discussed below. Note that here, "exact" still refers to the simplified problem (orientational average+sticky limit) of Secs. 3.3 and 3.4.

The expansion to first order in density of the Laplace transforms $Y_{ij}(s)$ obtained from Eqs. (3.37), (3.51)–(3.52b), and (3.56)–(3.58d) is

$$Y_{ij}(s) = e^{-s}\left(s^{-1} + s^{-2}\right) + Y_{ij}^{(1)}(s)\rho + \cdots, \tag{3.72}$$

where the expressions of the first-order coefficients $Y_{ij}^{(1)}(s)$ will be omitted here. Laplace inversion yields

$$\overline{y}_{ij}^{(1)}(r) = \overline{y}_{ij}^{(1)}(r)\Big|_{\text{exact}} - \Delta\overline{y}_{ij}^{(1)}(r), \tag{3.73}$$

where $y_{ij}^{(1)}(r)\Big|_{\text{exact}}$ are the exact first-order functions given by Eqs. (C.20c)–(C.20e) and the deviations $\Delta y_{ij}^{(1)}(r)$ are

$$\Delta\overline{y}_{11}^{(1)}(r) = \Theta(2-r)x_2\frac{2t^2}{r}\cos^{-1}\frac{r}{2}, \tag{3.74a}$$

$$\Delta\overline{y}_{12}^{(1)}(r) = \Theta(2-r)t\left(2\sqrt{1-r^2/4} - r\cos^{-1}\frac{r}{2}\right), \tag{3.74b}$$

$$\Delta\overline{y}_{21}^{(1)}(r) = -\Delta\overline{y}_{12}^{(1)}(r). \tag{3.74c}$$

In the case of the global quantity $\overline{y}^{(1)}(r)$ the result is

$$\overline{y}^{(1)}(r) = \overline{y}^{(1)}(r)\big|_{\text{exact}} - \Delta\overline{y}^{(1)}(r), \tag{3.75}$$

where $\overline{y}^{(1)}(r)\big|_{\text{exact}}$ is given by Eq. (C.20f) and

$$\Delta\overline{y}^{(1)}(r) = \Theta(2-r)x_1x_2\frac{2t^2}{r}\cos^{-1}\frac{r}{2}. \tag{3.76}$$

While the main qualitative features of the exact cavity function are preserved, there exist quantitative differences. The first-order functions $\overline{y}_{11}^{(1)}(r)$, $\overline{y}_{22}^{(1)}(r)$, and $\overline{y}^{(1)}(r)$ predicted by the RFA account for the exact coefficient of t but do not include the exact term of order t^2 proportional to $r^{-1}\cos^{-1}(r/2)$. In the case of $\overline{y}_{12}^{(1)}(r)$ and $\overline{y}_{21}^{(1)}(r)$ the exact term of order t proportional to $2\sqrt{1-r^2/4} - r\cos^{-1}(r/2)$ is lacking. Also, while the combination $\overline{y}_{11}^{(1)}(r) + \overline{y}_{22}^{(1)}(r) - \overline{y}_{12}^{(1)}(r) - \overline{y}_{21}^{(1)}(r)$ vanishes in the RFA, the exact result is proportional to $t^2r^{-1}\cos^{-1}(r/2)$. In short, the RFA correctly accounts for the polynomial terms in $y_{ij}^{(1)}(r)\Big|_{\text{exact}}$ but misses the non-polynomial terms.

As for the thermodynamic quantities, expansion of Eqs. (3.63), (3.67), and (3.71) gives

$$Z^v = 1 + 4\left(1 - 3x_1x_2t\right)\eta + 10\left[1 - 6x_1x_2t\left(1 - \frac{4}{5}t\right)\right]\eta^2 + \mathcal{O}(\eta^3), \tag{3.77a}$$

$$Z^u = 1 + 4\left(1 - 3x_1x_2t\right)\eta + 10\left[1 - 6x_1x_2t\left(1 - \frac{6}{5}t\right)\right]\eta^2 + \mathcal{O}(\eta^3), \tag{3.77b}$$

$$Z^c = 1 + 4\,(1 - 3x_1x_2t)\,\eta + 10\left[1 - 6x_1x_2t\left(1 - \frac{8}{5}t\right)\right]\eta^2 + \mathcal{O}(\eta^3). \quad (3.77c)$$

Comparison with the exact third virial coefficient, Eq. (C.20p), shows that the coefficient of t^2 is not correct, with the exact factor $4 - 3\sqrt{3}/\pi \simeq 2.35$ replaced by 2, 3, and 4 in Eqs. (3.77a)–(3.77c), respectively. One consequence is that the virial and energy routes predict the third virial coefficient much better than the compressibility route. A possible improvement is through the interpolation formula

$$Z^{v,u} = \alpha\left(Z^v + Z^{\rm CS}_{\rm HS} - Z^v_{\rm HS}\right) + (1 - \alpha)Z^u, \quad (3.78)$$

where

$$\alpha \equiv \frac{3\sqrt{3}}{\pi} - 1 \simeq 0.65 \quad (3.79)$$

with the proviso that $Z^u_{\rm HS} = Z^{\rm CS}_{\rm HS}$ in Eq. (3.67). Equation (3.78) then reduces to the CS equation of state if $t = 0$ and reproduces the exact third virial coefficient when $t \neq 0$.

3.5.3.4 Phase transition and critical point

In the limit of isotropic interaction ($t_{ij} = t$), our model reduces to the usual SHS Baxter adhesive one-component model. In spite of the fact that the model is, strictly speaking, known to be pathological [64], it displays a critical behavior that was numerically studied in some details by MC techniques [65, 66]. The corresponding binary mixture also displays well defined critical properties that, interestingly, are even free from any pathological behavior [50].

Moreover, the mechanism behind the pathology of the isotropic Baxter model hinges crucially on the geometry of certain close-packed clusters involving 12 or more equal-sized spheres [64]. On the other hand, our Janus model, having frozen orientations, cannot sustain those pathological configurations.

Within the PY approximation, the critical behavior of the original one-component Baxter SHS model was studied using the compressibility and virial routes [32], as well as the energy route [46], in the latter case with the implicit assumption

TABLE 3.1: Location of the critical point in the RFA, according to different routes.

Route	τ_c	η_c	Z_c
virial, Eq. (3.63)	0.02050	0.1941	0.3685
energy, Eq. (3.67)	0.0008606	0.2779	0.2906
hybrid virial-energy, Eq. (3.78)	0.01504	0.1878	0.3441

$Z^u_{\rm HS} = Z^{\rm CS}_{\rm HS}$. Numerical simulations indicate that the critical point found through the energy route is the closest to numerical simulation results [65, 66].

As the present specific model (with, $t_{ij} = t\delta_{i1}\delta_{j2}$) is, in some sense, intermediate between the fully isotropic Baxter SHS one-component model (that has a full, albeit peculiar, gas-liquid transition) and the equally isotropic HS model (that, lacking any attractive part in the potential, cannot have any gas-liquid transition), it is then interesting to ask whether in the equimolar case ($x_1 = x_2 = \frac{1}{2}$) it still presents a critical gas-liquid transition.

The answer depends on the route followed to obtain the pressure. As seen from Eq. (3.70), the compressibility route yields a positive definite χ_T^{-1}, so that no critical point is predicted by this route. On the other hand, an analysis of the virial [Eq. (3.63)], energy [Eq. (3.67) with $Z^u_{\rm HS} = Z^{\rm CS}_{\rm HS}$], and hybrid virial-energy [Eq. (3.78)] equations of state reveals the existence of van der Waals loops with the respective critical points shown in Table 3.1. The energy route predicts a critical value τ_c about twenty times smaller than the values predicted by the other two routes.

As an illustration, Fig. 3.4 shows the binodal and a few isotherms, as obtained from the virial route.

3.5.3.5 A modified approximation

The failure of the RFA to reproduce the exact cavity functions to first order in density (and hence the third virial coefficient) for asymmetric interactions ($t_{ij} \neq t_{ji}$) reveals the price paid for using the orientationally averaged quantities $\overline{g}_{ij}(r)$ instead of the true pair correlation functions $g_{ij}(\mathbf{r})$.

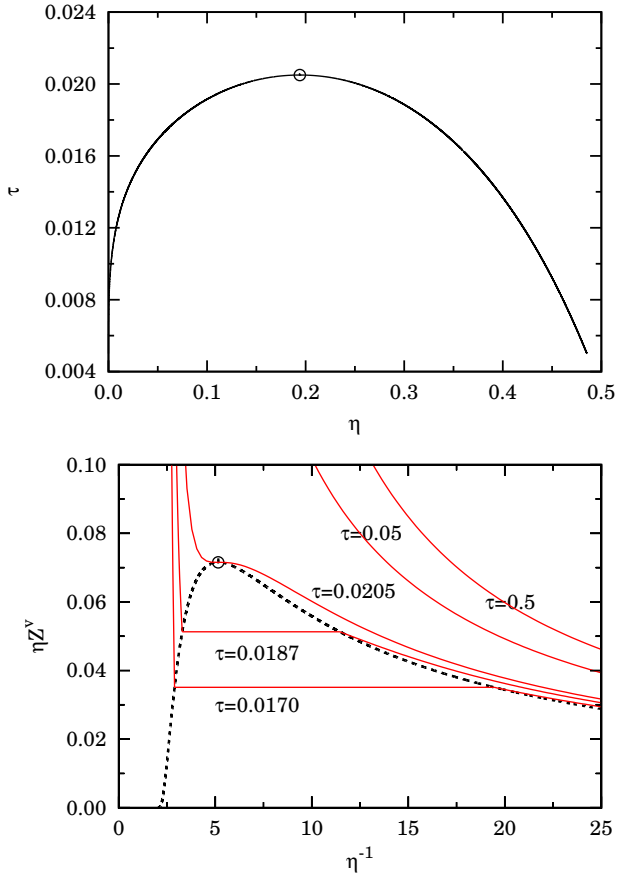

FIGURE 3.4: Binodals from the RFA virial route in the equimolar $x_1 = \frac{1}{2}$ case. The phase diagram is depicted in the (η, τ) plane (solid line, top panel) and in the $(\eta^{-1}, \eta Z^v)$ plane (dashed line, bottom panel). A few characteristic isotherms are plotted in the bottom panel. The critical point is found at $\eta_c \simeq 0.1941$, $\tau_c \simeq 0.02050$, and $\eta_c Z_c \simeq 0.07153$ (indicated by a circle in both panels).

A simple way of getting around this drawback for sufficiently low values of both η and t consists in modifying the RFA as follows:

$$\overline{y}_{ij}(r) \to \overline{y}_{ij}(r) + \Delta\overline{y}_{ij}^{(1)}(r)\rho, \tag{3.80}$$

where the functions $\Delta\overline{y}_{ij}^{(1)}(r)$ are given by Eqs. (3.74a)–(3.74c). We will refer to this as the *modified* rational-function approximation (mRFA). Note that Eq. (3.80) implies that $\overline{g}_{ij}(r) \to \overline{g}_{ij}(r) + \Delta\overline{y}_{ij}^{(1)}(r)\rho$, except if $(i,j) = (1,2)$, in which case $\overline{g}_{12}(r) \to \overline{g}_{12}(r) + \Delta\overline{y}_{12}^{(1)}(r)\rho + \Delta\overline{y}_{12}^{(1)}(1)\delta_+(r-1)\rho t$.

Since the extra terms in Eq. (3.80) are proportional to t or t^2, this modification can produce poor results for sufficiently large stickiness (say, $t \gtrsim 1$) as, for

instance, near the critical point.

3.6 Numerical calculations

3.6.1 Details of the simulations

In order to check the theoretical predictions previously reported, NVT (isochoric-isothermal) MC simulations have been performed using the Kern–Frenkel potential defined in Eqs. (3.1)–(3.4) with a single attractive SW patch (green in the color code of Fig. 3.1) covering one of the two hemispheres, and with up-down symmetry as depicted in Fig. 3.2. Particles are then not allowed to rotate around but only to translate rigidly.

The model is completely defined by specifying the relative width $\lambda - 1$, the concentration of one species (mole fraction) $x_1 = 1 - x_2$, the reduced density $\rho^* = \rho\sigma^3$, and the reduced temperature $T^* = k_B T/\epsilon$.

In order to make sensible comparison with the RFA theoretical predictions, we have selected the value $\lambda - 1 = 0.05$ as a well width, which is known to be well represented by the SHS limit [67], and use Baxter's temperature parameter $\tau = \left[4(\lambda^3 - 1)\left(e^{1/T^*} - 1\right)\right]^{-1}$ [see Eq. (3.28)] instead of T^*. It is interesting to note that, while the unconventional phase diagram found in the simulations of Ref. [15] corresponded to a larger well width ($\lambda = 1.5$), the value $\lambda = 1.05$ is in fact closer to the experimental conditions of Ref. [41].

During the simulations, the orientational averaged pair correlation functions defined by Eqs. (3.9a) and (3.9b) have been computed, accumulating separate histograms when $z_2 - z_1 > 0$ or $z_1 - z_2 > 0$ in order to distinguish between functions $\overline{g}_{12}(r) = g_{12}^{+}(r)$ and $\overline{g}_{21}(r) = g_{12}^{-}(r)$.

The compressibility factor $Z = \beta P/\rho$ has been evaluated from the values of $\overline{y}_{ij}(r)$ at $r = \sigma$ and $r = \lambda\sigma$ by following Eq. (3.26) with $t_{ij} = (12\tau)^{-1}\delta_{i1}\delta_{j2}$, and

the reduced excess internal energy per particle $u^*_{\rm ex} = u_{\rm ex}/\epsilon$ has been evaluated directly from simulations.

In all the simulations, $N = 500$ particles, periodic boundary conditions, an equilibration time of around 10^5 MC steps (where a MC step corresponds to a single particle displacement), and a production time of about 10^8 MC steps for the structure calculations and up to 5×10^8 MC steps for the thermophysical calculations were used. The maximum particle displacement was determined during the first stage of the equilibration run in such a way as to ensure an average acceptance ratio of 50% at production time.

3.6.2 Results for non-equimolar binary mixtures

As a preliminary attempt, we consider a binary mixture under non-equimolar conditions, to avoid possible pathologies arising from the symmetry of the two components akin to those occurring in ionic systems. As we shall see below, no such pathologies are found.

In the present case, we consider a system with $x_1 = 1/5$ and $x_2 = 1 - x_1 = 4/5$, so that the majority of the spheres have (green) attractive patches pointing in the direction of $-\widehat{\mathbf{z}}$.

A snapshot of an equilibrated configuration is shown in Fig. 3.5. This configuration was obtained using $N = 500$ particles at $\rho^* = 0.3$ and Baxter temperature $\tau = 0.1$ (corresponding to $T^* \simeq 0.354$). Note that the above chosen state point ($\rho^* = 0.3$ and $\tau = 0.1$) lies well inside the critical region of the full Baxter SHS adhesive model as obtained from direct MC simulations [65, 66], although of course the present case is expected to display a different behavior as only a fraction of about $x_1 x_2 = 4/25$ of the pair contacts are attractive.

A good insight on the structural properties of the system can be obtained from the computation of the radial distribution functions $\overline{g}_{11}(r)$, $g^+_{12}(r) = \overline{g}_{12}(r)$, $g^-_{12}(r) = \overline{g}_{21}(r)$, and $\overline{g}_{22}(r)$. This is reported in Fig. 3.6 for a state point at density

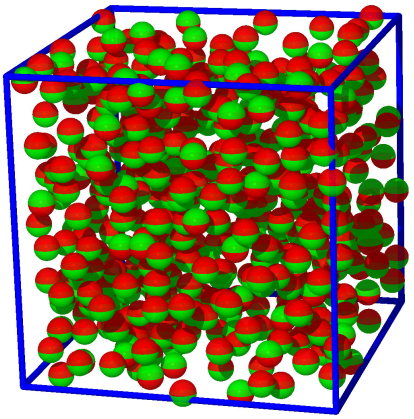

FIGURE 3.5: Snapshot of an equilibrated MC simulation under non-equimolar conditions ($x_1 = 1/5$) with Baxter temperature $\tau = 0.1$ and density $\rho^* = 0.3$. In the simulations, the total number of particles was $N = 500$.

$\rho^* = 0.5$ and Baxter temperature $\tau = 0.2$ (corresponding to $T^* \simeq 0.457$). Note that in the case of the pair $(1, 2)$ what is actually plotted is the cavity function $\overline{y}_{12}(r)$ rather than $\overline{g}_{12}(r)$, as explained in the caption of Fig. 3.6.

The relatively low value $\tau = 0.2$ gives rise to clearly distinct features of the four MC functions $\overline{g}_{ij}(r)$ (which would collapse to a common HS distribution function in the high-temperature limit $\tau \to \infty$). We observe that $\overline{g}_{22}(r) \simeq \overline{g}_{21}(r) > \overline{g}_{11}(r) > \overline{y}_{12}(r)$ in the region $1 \leq r \lesssim 1.5$. Moreover, $\overline{g}_{11}(r)$ and $\overline{g}_{12}(r)$ exhibit a rapid change around $r = 2$. This is because when a pair $(1, 1)$ is separated a distance $r \approx 2$ there is enough room to fit a particle of species 2 in between and that particle will interact attractively with the particle of the pair $(1, 1)$ below it. In the case of the pair $(1, 2)$ separated a distance $r \approx 2$, the intermediate particle can be either of species 1 (interacting attractively with the particle of species 2 above it) or of species 2 (interacting attractively with the particle of species 1 below it). The same argument applies to a pair $(2, 2)$ separated a distance $r \approx 2$, but in that case the intermediate particle must be of species 1 to produce an attractive interaction; since the concentration of species 1 is four times smaller than that of species 2, the rapid change of $\overline{g}_{22}(r)$ around $r = 2$ is much less apparent than that of $\overline{g}_{11}(r)$ and $\overline{g}_{12}(r)$ in Fig. 3.6. On the other hand, in a pair $(2, 1)$ separated a distance $r \approx 2$ an intermediate particle of either species 1 or of species 2 does not

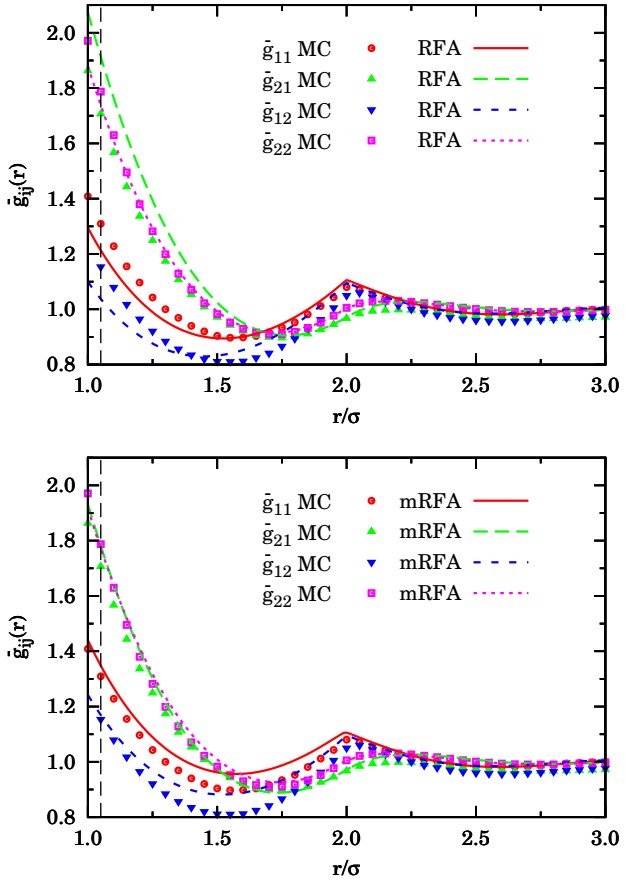

FIGURE 3.6: Comparison between MC simulations and the theoretical predictions from RFA (top) and mRFA (bottom) for the orientational averaged distribution functions $\overline{g}_{11}(r)$, $\overline{y}_{12}(r)$, $\overline{g}_{21}(r)$, and $\overline{g}_{22}(r)$ under non-equimolar conditions ($x_1 = 1/5$) at density $\rho^* = 0.5$ and Baxter temperature $\tau = 0.2$. The dashed vertical line indicates the range $r = \lambda = 1.05$ of the $(1, 2)$ SW interaction used in the simulations. Note that the radial distribution function $\overline{g}_{12}(r)$ is obtained in the MC case by multiplying $\overline{y}_{12}(r)$ in the region $1 \leq r \leq \lambda = 1.05$ by the factor $e^{1/T^*} \simeq 8.93$; in the theoretical cases (SHS limit) $\overline{g}_{12}(r)$ is obtained by adding the singular term $(12\tau)^{-1}\overline{y}_{12}(1)\delta_+(r-1)$ to $\overline{y}_{12}(r)$. The error bars on the MC data are within the size of the symbols used.

create any attraction and thus $\overline{g}_{21}(r)$ is rather smooth at $r = 2$. In short, the pair correlation function $\overline{g}_{21}(r)$ exhibits HS-like features, $\overline{g}_{12}(r)$ exhibits SW-like features (very high values in the region $1 \leq r \leq \lambda$ and discontinuity at $r = \lambda$ due to the direct SW interaction; rapid change around $r = 2$ due to indirect SW interaction), while $\overline{g}_{11}(r)$ and $\overline{g}_{22}(r)$ exhibit intermediate features (rapid change around $r = 2$ due to indirect SW interaction).

It is rewarding to notice how well the MC results are reproduced at a semi-quantitative level by the RFA theory (top panel of Fig. 3.6), in spite of the various approximations involved. In this respect, it is worth recalling that while MC simulations deal with the real Kern–Frenkel potential, albeit with constrained angular orientations, the RFA theory deals with the asymmetric binary mixture resulting from the mapping described in Section 3.2, and this represents an indirect test of the correctness of the procedure. In addition, the RFA does not attempt to describe the true SW interaction (i.e., finite $\lambda - 1$ and T^*) but the SHS limit ($\lambda - 1 \to 0$ and $T^* \to 0$ with finite τ). This limit replaces the high jump of $\overline{g}_{12}(r)$ in the region $1 \leq r \leq \lambda$ by a Dirac's delta at $r = 1^+$ and the rapid change of $\overline{g}_{12}(r)$, $\overline{g}_{11}(r)$, and $\overline{g}_{22}(r)$ around $r = 2$ by a kink. Finally, the RFA worked out in Sec. 3.5.2 results from a heuristic generalization to asymmetric mixtures ($\tau_{ij} \neq \tau_{ji}$) of the PY exact solution for SHS symmetric mixtures ($\tau_{ij} = \tau_{ji}$) [47, 48, 49, 50, 51, 53], but it is not the solution of the PY theory for the asymmetric problem, as discussed in Sec. 3.5.1. As a matter of fact, the top panel of Fig. 3.6 shows that some of the drawbacks of the RFA observed to first order in density in Sec. 3.5.3.3 [see Eqs. (3.73)–(3.74c)] remain at finite density: in the region $1 \leq r \lesssim 1.5$ the RFA underestimates $\overline{y}_{12}(r)$, $\overline{g}_{11}(r)$, and $\overline{g}_{22}(r)$, while it overestimates $\overline{g}_{21}(r)$. These discrepancies are widely remedied, at least in the region $1 \leq r \lesssim 1.25$, by the mRFA approach [see Eq. (3.80)], as shown in the bottom panel of Fig. 3.6. In particular, the contact values are well accounted for by the mRFA, as well as the property $\overline{g}_{22}(r) \simeq \overline{g}_{21}(r)$. We have observed that the limitations of the correlation functions $\overline{g}_{ij}(r)$ predicted by the RFA become more important as the density and, especially, the stickiness increase and in those cases the mRFA version does not help much since the correction terms $\Delta\overline{y}_{ij}^{(1)}(r)\rho$, being proportional to ρ and to t or t^2, become too large.

Next we consider thermodynamic quantities, as represented by the compressibility factor $Z = \beta p/\rho$ and the excess internal energy per particle u_{ex}/ϵ, both directly accessible from NVT numerical MC simulations. These quantities are depicted in Fig. 3.7 as functions of the reduced density ρ^* and for a Baxter temperature $\tau = 0.1$. In both cases, the results for the RFA theory are also included. In

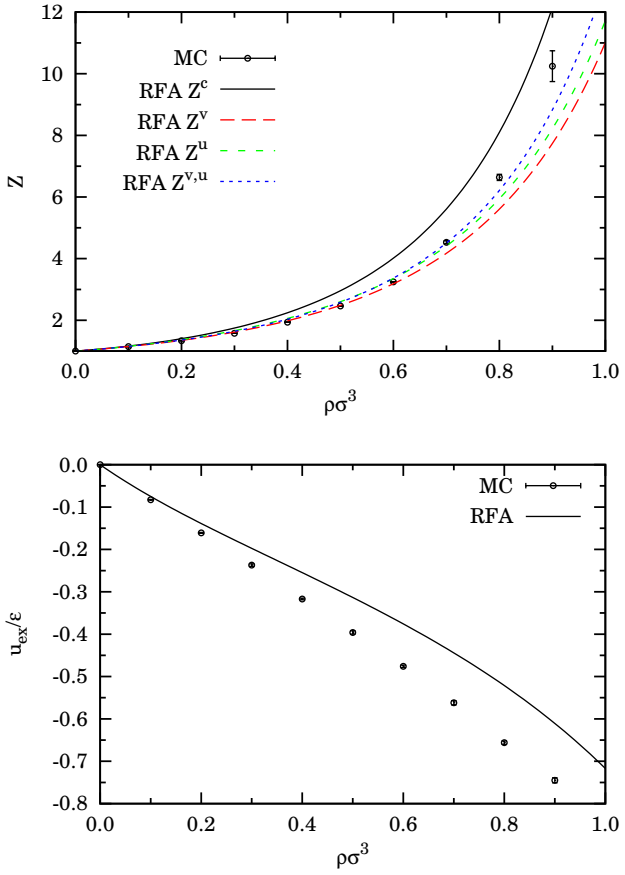

FIGURE 3.7: Comparison of MC simulations and RFA theory for the thermodynamics. Both the compressibility factor $Z = \beta p/\rho$ (top) and the excess internal energy per particle $u_{\rm ex}/\epsilon$ (bottom) are displayed as functions of density for the non-equimolar case $x_1 = 1/5$ and for Baxter temperature $\tau = 0.1$. In the case of the compressibility factor (top), results for all four routes (compressibility, virial, energy, and hybrid virial-energy) are reported.

the case of the compressibility factor, all four routes are displayed: compressibility [Eqs. (3.57), (3.69), and (3.71)], virial [Eqs. (3.57), (3.62), and (3.63)], energy [Eq. (3.57) and (3.67) with $Z^u_{\rm HS} = Z^{\rm CS}_{\rm HS}$], and hybrid virial-energy [Eq. (3.78)]. In the case of $u_{\rm ex}/\epsilon$, only the genuine energy route, Eq. (3.65), is considered. Note that all RFA thermodynamic quantities, including Eq. (3.71), have explicit analytical expressions.

The top panel of Fig. 3.7 shows that up to $\rho^* \approx 0.7$ the MC data for the compressibility factor are well predicted by the theoretical Z^v and, especially, Z^u and $Z^{v,u}$. Beyond that point, the numerical results are bracketed by the compressibility route, that overestimates the pressure, and the hybrid virial-energy route, that on

the contrary underestimates it. It is interesting to note that, while $Z^v < Z^{v,u} < Z^u$ to second order in density [cf. Eqs. (3.77a), (3.77b), and (3.78)], the difference $Z^v - Z^v_{\rm HS}$ grows with density more rapidly than the difference $Z^u - Z^u_{\rm HS}$ and so both quantities cross at a certain density ($\rho^* \simeq 0.567$ if $x_1 = 1/5$ and $\tau = 0.1$). Therefore, even though $Z^v < Z^u$ (because $Z^v_{\rm HS} < Z^{\rm CS}_{\rm HS}$), $Z^{v,u}$ is no longer bracketed by Z^v and Z^u beyond that density ($\rho^* \simeq 0.567$ in the case of Fig. 3.7). On balance, the virial-energy route appears to be the most effective one in reproducing the numerical simulations results of the pressure at $x_1 = 1/5$ and $\tau = 0.1$.

As for the internal energy, the bottom panel of Fig. 3.7 shows that the RFA underestimates its magnitude as a direct consequence of the underestimation of the contact value $\overline{y}_{12}(1)$ [see Eq. (3.65)]. Although not shown in Fig. 3.7, we have checked that the internal energy per particle obtained from the virial equation of state (3.63) via the thermodynamic relation (3.66) exhibits a better agreement with the simulation data than the direct energy route.

3.6.3 Results for equimolar binary mixtures

Having rationalized the non-equimolar case, the equimolar ($x_1 = x_2 = 1/2$) case can now be safely tackled. The equimolarity condition makes the system be more akin to the original Janus model (see Fig. 3.1) since both spin orientations are equally represented.

We start with the snapshot of an equilibrated configuration at density $\rho^* = 0.3$ and Baxter temperature $\tau = 0.1$, that are the same values used in the non-equimolar case. From Fig. 3.8 it can be visually inspected that, in contrast to the non-equimolar case of Fig. 3.5, the number of particles with spin up matches that with spin down. This equimolar condition then facilitates the interpretation of the corresponding structural properties, as illustrated by the radial distribution function $\overline{g}_{ij}(r)$ given in Fig. 3.9.

This was obtained at a Baxter temperature $\tau = 0.2$ and a density $\rho^* = 0.5$, a state point that is expected to be outside the coexistence curve (see below), but

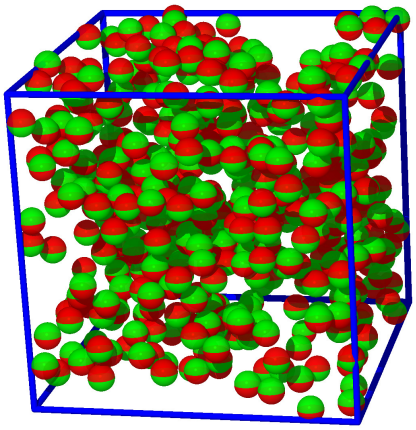

FIGURE 3.8: Same as in Fig. 3.5, but for an equimolar mixture ($x_1 = x_2 = 1/2$).

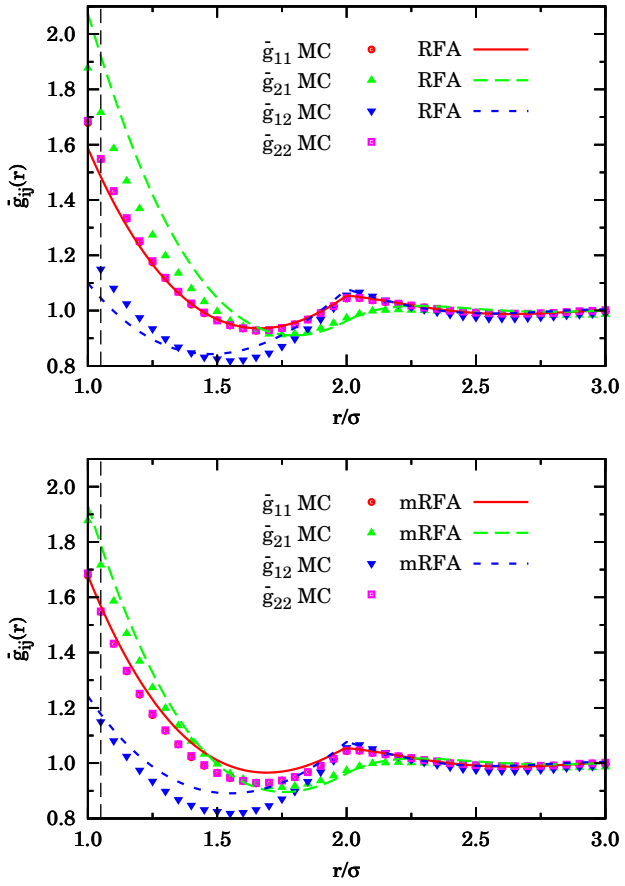

FIGURE 3.9: Same as in Fig. 3.6, but for an equimolar mixture ($x_1 = x_2 = 1/2$).

inside the liquid region. Again, this is the same state point as the non-equimolar case previously discussed. Now $\overline{g}_{11}(r) = \overline{g}_{22}(r)$ (independently computed) as it should. Notice that the main features commented before in connection with Fig. 3.6 persist. In particular, $\overline{g}_{21}(r) > \overline{g}_{11}(r) = \overline{g}_{22}(r) > \overline{y}_{12}(r)$ in the region $1 \leq r \lesssim 1.5$, $\overline{g}_{11}(r) = \overline{g}_{22}(r)$ and $\overline{g}_{12}(r)$ present rapid changes around $r = 2$, and $\overline{g}_{21}(r)$ exhibits a HS-like shape. Also, as before, the RFA captures quite well the behaviors of the correlation functions (especially noteworthy in the case of $\overline{g}_{11} = \overline{g}_{22}$). On the other hand, the RFA tends to underestimate $\overline{y}_{12}(r)$ and $\overline{g}_{11}(r) = \overline{g}_{22}(r)$ and to overestimate $\overline{g}_{21}(r)$ in the region $1 \leq r \lesssim 1.5$. The use of the modified version (mRFA) partially corrects those discrepancies near contact, although the general behavior only improves in the case of $\overline{g}_{21}(r)$.

Comparison between Figs. 3.6 and 3.9 shows that $\overline{y}_{12}(r)$ and $\overline{g}_{21}(r)$ are very weakly affected by the change in composition. In fact, the spatial correlations between particles of species 1 and 2 mediated by a third particle (i.e., to first order in density) depend strongly on which particle (1 or 2) is above o below the other one but not on the nature of the third intermediate particle, as made explicit by Eqs. (C.20d) and (C.20e). Of course, higher-order terms (i.e., two or more intermediate particles) create a composition-dependence on $\overline{y}_{12}(r)$ and $\overline{g}_{21}(r)$, but this effect seems to be rather weak. On the contrary, the minority pair increases its correlation function $\overline{g}_{11}(r)$, while the majority pair decreases its correlation function $\overline{g}_{22}(r)$ in the region $1 \leq r \lesssim 1.5$ when the composition becomes more balanced. Again, this can be qualitatively understood by the exact results to first order in density [see Eq. (C.20c)].

3.6.4 Preliminary results on the critical behavior

One of the most interesting and intriguing predictions of the RFA is the existence of a gas-liquid transition in the equimolar model, despite the fact that only one of the four classes of interactions is attractive (see Sec. 3.5.3.4). The elusiveness of this prediction is reflected by the fact that the compressibility route does not account for a critical point and, although the virial and energy routes do, they

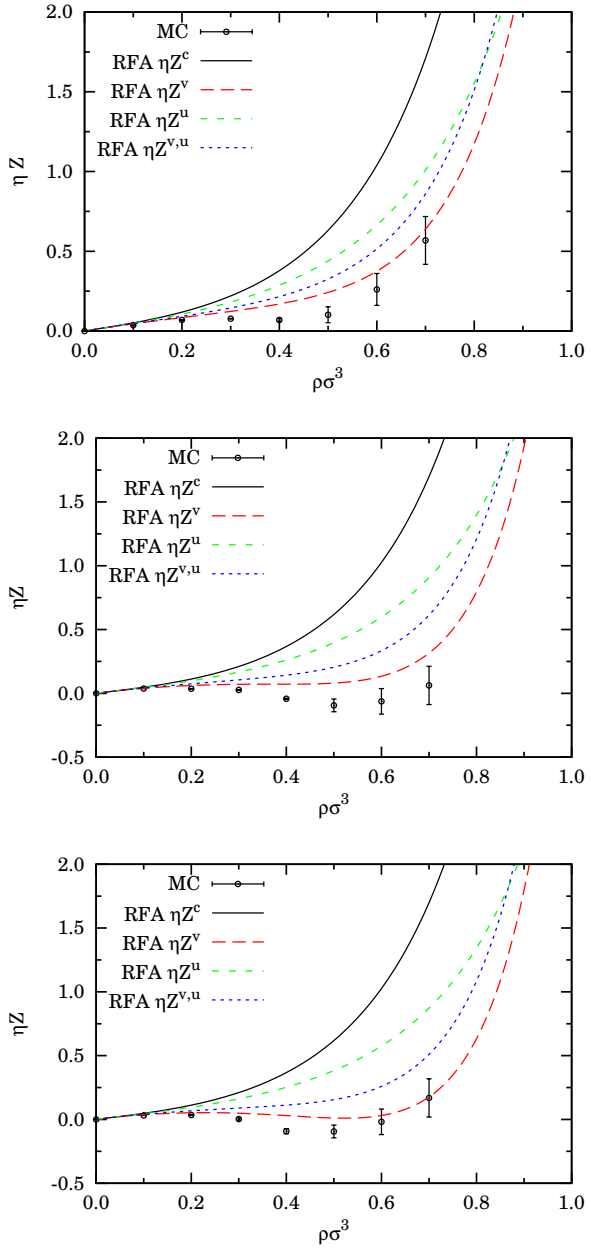

FIGURE 3.10: MC simulation data for the scaled pressure $\eta Z = \frac{\pi}{6}\sigma^3\beta p$ as a function of ρ^* at $\tau = 0.030$ (top panel), 0.0205 (middle panel), and $\tau = 0.018$ (bottom panel) in an equimolar mixture. Densities higher than $\rho^* = 0.7$ are not shown because at these very low temperatures the particles tend to overlap their SW shells and then the calculations slow down considerably. Also shown are the theoretical results for the four routes of the RFA.

widely differ in its location, as seen in Table 3.1. In this region of very low values of τ the hybrid virial-energy equation of state is dominated by the virial one and thus the corresponding critical point is not far from the virial value.

A simple heuristic argument can be used to support the existence of a true critical point in our model. According to the Noro–Frenkel (NF) generalized principle of corresponding states [68], the critical temperatures of different systems of particles interacting via a hard-core potential plus a short-range attraction are such that the reduced second virial coefficient $B_2^* = B_2/B_2^{\rm HS}$ has a *common* value $B_2^{*c} \simeq -1.21$. In our model, the reduced second virial coefficient is $B_2^* = 1 - 3t/4 = 1 - 1/16\tau$ [see Eq. (C.20o)]. Thus, assuming the NF ansatz, the critical point would correspond to $\tau_c^{\rm NF} \simeq 0.028$, a value higher than but comparable to that listed in Table 3.1 from the virial route.

From the computational point of view, a direct assessment on the existence of a gas-liquid transition in the present model is not a straightforward task and will be postponed to Ch. 4. Unlike the original SHS Baxter model, a Gibbs ensemble MC (GEMC) calculation for a binary mixture is required to find the coexistence lines. As a preliminary study, we here report NVT results with values of the Baxter temperature close to the critical value $\tau_c^{\rm NF} \simeq 0.028$ expected on the basis of the NF conjecture. More specifically, we have considered $\tau = 0.030$, 0.0205, and 0.018 (corresponding to $T^* \simeq 0.251$, 0.229, and 0.223, respectively). The numerical results for the pressure, along with the RFA theoretical predictions, are displayed in Fig. 3.10.

We observe that at $\tau = 0.030$ (top panel) the four theoretical routes clearly indicate a single-phase gas-like behavior with a monotonic increase of the pressure as a function of the density, in consistence with the value $\tau_c \simeq 0.0205$ obtained from the RFA virial route. On the other hand, the MC data show a practically constant pressure between $\rho^* = 0.2$ and $\rho^* = 0.4$, which is suggestive of $\tau = 0.030$ being close to the critical isotherm (remember that $\tau_c^{\rm NF} \simeq 0.028$). The middle panel has been chosen to represent the critical isotherm predicted by the RFA-virial equation of state. In that case, the simulation data present a clear van der

Waals loop with even negative pressures around the minimum. A similar behavior is observed at $\tau = 0.018$ (bottom panel), except that now the RFA-virial isotherm also presents a visible van der Waals loop. Whereas the observation of negative values of isothermal compressibility in the MC simulations can be attributed to finite-size effects and are expected to disappear in the thermodynamic limit, these preliminary results are highly supportive of the existence of a gas-liquid phase transition in our model with a critical (Baxter) temperature $\tau_c \approx 0.03$. Further results will be presented in Ch. 4.

In view of the extremely short-range nature of the potential, the stability of the above liquid phases with respect to the corresponding solid ones may be rightfully questioned [15]. This is a general issue—present even in the original Baxter model, as well as in the spherically symmetric SW or Yukawa potentials with sufficiently small interaction range [69, 70, 71, 72]—that is outside the scope of the present thesis. In any case, it seems reasonable to expect that at sufficiently low temperature and high density the stable phase will consist of an fcc crystal made of layers of alternating species (1-2-1-2-$\cdots$) along the z direction.

3.7 Summary and remarks

Along this chapter, we have studied thermophysical and structural properties of a three-dimensional Janus fluid having constrained orientations for the attractive hemisphere. The Janus fluid has been modeled using a Kern–Frenkel potential with a single SW patch pointing either up or down, and studied using numerical NVT MC simulations.

The above model has been mapped onto an asymmetric binary mixture where the only memory of the original anisotropic potential stems from the relative position along the z-axis of particles of the two species 1 and 2. In this way, only one [$(1, 2)$ with our choice of labels] out of the four possible interactions is attractive, the other ones [$(1, 1)$, $(2, 1)$, and $(2, 2)$] being simply HS interactions.

In the limit of infinitely short and deep SW interactions (sticky limit), we discussed how a full analytical theory is possible. We developed a new formulation for asymmetric mixtures of the rational-function approximation (RFA), that is equivalent to the PY approximation in the case of symmetric SHS interactions, but differs from it in the asymmetric case. Results from this theory were shown to be in nice agreement with MC simulations using SW interactions of sufficiently short width (5% of particle size), both for the structural and the thermodynamic properties.

The above agreement is rather remarkable in view of the rather severe approximations involved in the RFA analysis—that are however largely compensated by the possibility of a full analytical treatment—and, more importantly, by the fact that simulations deal with the one-component Kern–Frenkel potential with up-down constrained orientations of the patches and SW attractions, while the RFA theory deals with the corresponding asymmetric binary mixture and SHS interactions. This agreement can be regarded as an important indication on the correctness of the mapping.

The work presented in this chapter seems to lead toward an analytical theory of the anomalous phase diagram revealed by numerical simulations of the unconstrained one-component Janus fluid, where the responsible inert clusters (micelles and vesicles) formed at low temperatures may be probably reproduced at the cost of modeling the fluid by a multi-component asymmetric mixture with each component corresponding to a differently oriented attractive hemisphere. An interesting question would be to ask how many components, how many directions, we would need to observe the formation of micelles or of vesicles. In the next chapter we will deal with the extension of the present model allowing for more general interactions where the red hemispheres in Fig. 3.2 also present a certain adhesion (e.g., $\tau_{12} < \tau_{11} = \tau_{22} = \tau_{21} < \infty$). This more general model (to which the theory presented in Sec. 3.5.2 still applies) can be continuously tuned from isotropic SHS ($\tau_{ij} = \tau$) to isotropic HS interactions ($\tau_{ij} \to \infty$). The increase in the (Baxter) critical temperatures and densities moving towards the full isotropic SHS fluid model would then mimic the corresponding displacement of the location of the

critical point upon an increase of the patch coverage observed in the unconstrained one-component Kern–Frenkel model [15].

4

Phase diagrams of Janus fluids with up-down constrained orientations

4.1 Introduction

In the present chapter, we generalize the Janus fluid model presented in Ch. 3 by assuming arbitrary values for the energy scales ϵ_{ij} of the attractive interactions associated with the four possible pair configurations (see Fig. 4.1), which allows for a free tuning of the strength of the patch-patch attraction. In some cases this can effectively mimic the reduction of the coverage in the original Kern–Frenkel model.

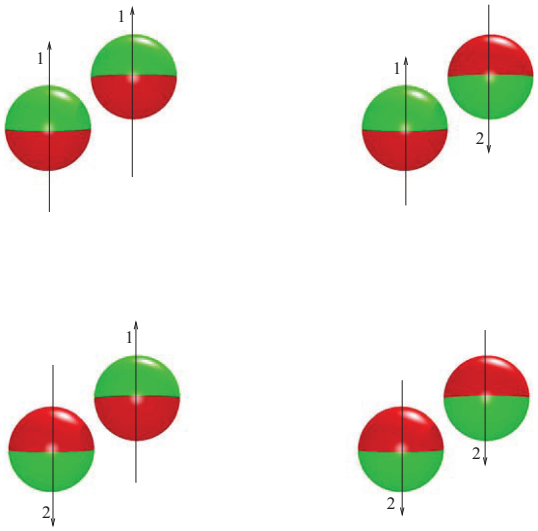

FIGURE 4.1: Sketch of a binary-mixture Janus fluid with up-down constrained orientations. The energy scales of the attractive interactions are (from left to right and from top to bottom) ϵ_{11}, ϵ_{12}, ϵ_{21}, and $\epsilon_{22} = \epsilon_{11}$, respectively. Here we have adopted the convention that ϵ_{ij} is the energy scale when a particle of species i is "below" a particle of species j.

Note that, in Fig. 4.1, ϵ_{ij} is the energy associated with the (attractive) interaction between a particle of species i (at the left) and a particle of species j (at the right) when the former is below the latter, with the arrow always indicating the hydrophobic (i.e. attractive) patch. The original Kern–Frenkel model then corresponds to $\epsilon_{12} > 0$ and $\epsilon_{11} = \epsilon_{22} = \epsilon_{21} = 0$, whereas the full coverage limit is equivalent to $\epsilon_{11} = \epsilon_{22} = \epsilon_{12} = \epsilon_{21} > 0$. On the other hand, the effect of reducing the coverage from the full to the Janus limit, can be effectively mimicked by fixing $\epsilon_{12} > 0$ and progressively decreasing ϵ_{21} and $\epsilon_{11} = \epsilon_{22}$. Moreover, the class of models depicted in Fig. 4.1 allows for an interpretation more general and flexible than the hydrophobic-hydrophilic one. For instance, one may assume that attraction is only possible when patches of *different* type are facing one another (i.e., $\epsilon_{11} = \epsilon_{22} > 0$ and $\epsilon_{12} = \epsilon_{21} = 0$). As shown below, this will provide a rich scenario of intermediate cases with a number of interesting features in the phase diagram of both the gas-liquid and the demixing transitions.

We emphasize the fact that in the simulation part of this chapter we will always assume "global" equimolarity, that is, the combined number of particles of species 1 (N_1) is always equal to the combined number of particles of species 2

(N_2), so that $N_1 = N_2 = N/2$, where N is the total number of particles. On the other hand, the equimolarity condition is not imposed on each coexisting phase.

This chapter opens with a brief definition of the models in Sec. 4.2, just to go with Gibbs ensemble Monte Carlo (GEMC) results for the gas-liquid and demixing transitions. The complementary theoretical approach is presented in Sec. 4.4.

4.2 Description of the models

In our class of binary-mixture Janus models, particles of species 1 (with a mole fraction x_1) and 2 (with a mole fraction $x_2 = 1 - x_1$) are dressed with two up-down hemispheres with different attraction properties, as sketched in Fig. 4.1. The pair potential between a particle of species i at $\mathbf{r}_1$ and a particle of species j at $\mathbf{r}_2$ is [see Eq. (3.5)]

$$\phi_{ij}(\mathbf{r}_{12}) = \varphi_{ij}(r_{12})\Theta(z_{12}) + \varphi_{ji}(r_{12})\Theta(-z_{12}), \tag{4.1}$$

where, as before, $\Theta(z)$ is the Heaviside step function, $\mathbf{r}_{12} = \mathbf{r}_2 - \mathbf{r}_1$, $z_{12} = z_2 - z_1$, and [see Eq. (3.25)]

$$\varphi_{ij}(r) = \begin{cases} \infty, & 0 \le r < \sigma, \\ -\epsilon_{ij}, & \sigma \le r < \sigma + \Delta, \\ 0, & \sigma + \Delta \le r, \end{cases} \tag{4.2}$$

is a standard square-well (SW) potential of diameter σ, width Δ, and energy depth ϵ_{ij}, except that, in general, $\epsilon_{12} \neq \epsilon_{21}$. By symmetry, one must have $\epsilon_{22} = \epsilon_{11}$ (see Fig. 4.1), so that (for given values of σ and Δ) the space parameter of the interaction potential becomes three-dimensional, as displayed in Fig. 4.2. Except in the case of the hard-sphere (HS) model ($\epsilon_{ij} = 0$), one can freely choose one of the non-zero ϵ_{ij} to fix the energy scale. Thus, we call $\epsilon = \max_{i,j}\{\epsilon_{ij}\}$ and use the three independent ratios ϵ_{ij}/ϵ as axes in Fig. 4.2. The model represented by the coordinates $(1, 1, 1)$ is the fully isotropic SW fluid, where species 1 and 2 become indistinguishable. Next, without loss of generality, we choose $\epsilon_{12} \ge \epsilon_{21}$.

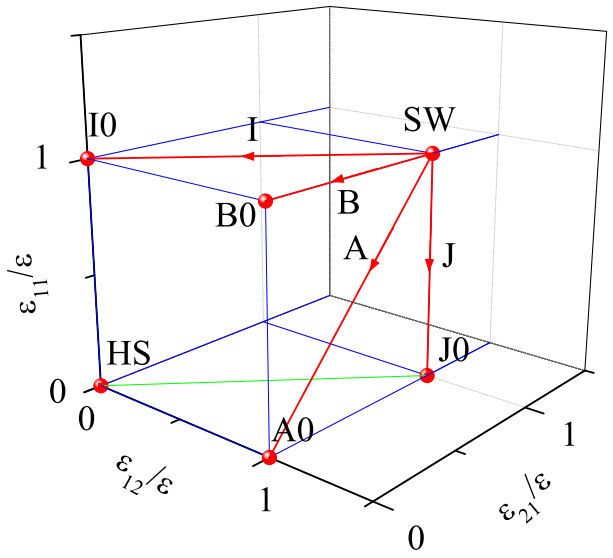

FIGURE 4.2: Parameter space of the class of Janus models defined in this chapter.

TABLE 4.1: Definition of the models.

Model	ϵ_{11}	ϵ_{12}	ϵ_{21}	ϵ_{22}
HS	0	0	0	0
A0	0	ϵ	0	0
I0	ϵ	0	0	ϵ
J0	0	ϵ	ϵ	0
B0	ϵ	ϵ	0	ϵ
SW	ϵ	ϵ	ϵ	ϵ

With those criteria, all possible models of the class lie either inside the triangle SW-I0-B0-SW or inside the square SW-B0-A0-J0-SW. One could argue that any point *inside* the cube displayed in Fig. 4.2 may represent a distinct model, but this is not so. First, the choice $\epsilon = \max_{i,j}\{\epsilon_{ij}\}$ restricts the models to those lying on one of the three faces $\epsilon_{11}/\epsilon = 1$, $\epsilon_{12}/\epsilon = 1$, or $\epsilon_{21}/\epsilon = 1$. Second, the choice $\epsilon_{12} \geq \epsilon_{21}$ reduces the face $\epsilon_{21}/\epsilon = 1$ to the line SW-J0 and the face $\epsilon_{11}/\epsilon = 1$ to the half-face SW-I0-B0-SW. The vertices SW, I0, B0, A0, and J0 define the five distinguished models we will specifically study. Those models, together with the HS one, are summarized in Table 4.1.

The rationale behind our nomenclature for the models goes as follows. Models with $\epsilon_{12} = \epsilon_{21}$ are isotropic and so we use the letter I to denote the isotropic models with $0 \leq \epsilon_{12}/\epsilon = \epsilon_{21}/\epsilon \leq 1$ and $\epsilon_{11}/\epsilon = 1$. Apart from them, the only additional

isotropic models are those with $\epsilon_{12}/\epsilon = \epsilon_{21}/\epsilon = 1$ and $0 \leq \epsilon_{11}/\epsilon \leq 1$, and we denote them with the letter (J) next to I. All the remaining models are anisotropic (i.e., $\epsilon_{12} \neq \epsilon_{21}$). Out of them, we use the letter A to denote the particular subclass of anisotropic models ($0 \leq \epsilon_{11}/\epsilon = \epsilon_{21}/\epsilon \leq 1$ and $\epsilon_{12}/\epsilon = 1$) which can be viewed as the anisotropic counterpart of the isotropic subclass I. Analogously, we employ the letter (B) next to A to refer to the anisotropic counterpart ($\epsilon_{11}/\epsilon = \epsilon_{12}/\epsilon = 1$ and $0 \leq \epsilon_{21}/\epsilon \leq 1$) of the isotropic models J. Finally, the number 0 is used to emphasize that the corresponding models are the extreme cases of the subclasses I, J, A, and B, respectively.

Model A0 is the one more directly related to the original Kern–Frenkel potential and was the one analyzed in Ch. 3. Also related to that potential is model B0, where only the interaction between the two hydrophilic patches is purely repulsive. On the other hand, in models I0 and J0 (where $\epsilon_{12} = \epsilon_{21}$) the interaction becomes isotropic and the Janus character of the model is blurred. In model I0 the fluid reduces to a binary mixture with attractive interactions between like components and HS repulsions between unlike ones. This model was previously studied by Zaccarelli et al. [73] using integral equation techniques. In the complementary model J0 attraction exists only between unlike particles. The points A0, B0, I0, and J0 can be reached from the one-component SW fluid along models represented by the lines A, B, I, and J, respectively. Of course, other intermediate models are possible inside the triangle SW-I0-B0-SW or inside the square SW-B0-A0-J0-SW.

In addition to the energy parameters ϵ_{ij}, the number density ρ, and the temperature T, each particular system is specified by the mixture composition (i.e., the mole fraction x_1). In fact, in Ch. 3 the thermodynamic and structural properties of model A0 were studied both under non-equimolar (see Sec. 3.6.2) and equimolar (see Sec. 3.6.3) conditions.

4.3 Gibbs ensemble Monte Carlo simulations

In this chapter, GEMC techniques [74, 75, 76] are used to study the gas-liquid condensation process of models SW, A0, B0, I0, and J0 and the demixing transition of models I0 and B0. We have chosen the width of the active attractive patch as in the experiment of Hong et al. [41] ($\Delta/\sigma = 0.05$). Given the very small width of the attractive wells, we expect the liquid phase to be metastable with respect to the corresponding solid one [65, 77, 78]. As usual, reduced densities $\rho^* = \rho\sigma^3$ and temperatures $T^* = k_B T/\epsilon$ will be employed throughout.

4.3.1 Technical details

The GEMC method is widely adopted as a standard method for calculating phase equilibria from molecular simulations. According to this method, the simulation is performed in two boxes (I and II) containing the coexisting phases. Equilibration in each phase is guaranteed by moving particles. Equality of pressures is satisfied in a statistical sense by expanding the volume of one of the boxes and contracting the volume of the other one, keeping the total volume constant. Chemical potentials are equalized by transferring particles from one box to the other one.

In the GEMC run we have on each step a probability $a_p/(a_p+a_v+a_s)$, $a_v/(a_p+a_v+a_s)$, and $a_s/(a_p+a_v+a_s)$ for a particle random displacement, a volume change, and a particle swap move between both boxes, respectively. In the results presented in this chapter, the relative weights $a_p = 1$, $a_v = 1/10$, and $a_s = 20$ have been generally used. To preserve the up-down fixed patch orientation, rotation of particles was not allowed. The maximum particle displacement was kept equal to $10^{-3}L^{(\gamma)}$ where $L^{(\gamma)}$ is the side of the (cubic) box γ =I, II. Regarding the volume changes, following Ref. [38] a random walk in $\ln(V^{(\mathrm{I})}/V^{(\mathrm{II})})$ is performed with $V^{(\gamma)}$ the volume of the box γ, choosing a maximum volume displacement of 1%. The volume move is computationally the most expensive one. This is because, after each volume move, it is necessary, in order to determine the next acceptance probability, to perform a full potential energy calculation since *all* the

particle coordinates are rescaled by the factor associated with the enlargement or reduction of the boxes. However, this is not necessary for the other two moves since in those cases only the coordinates of a single particle change.

Both in the condensation and in the demixing problems, the Monte Carlo swap move consisted in moving a particle selected randomly in one box into the other box, so that the number of particles of each species in both boxes ($N_1^{(\mathrm{I})}$, $N_2^{(\mathrm{I})}$, $N_1^{(\mathrm{II})}$, and $N_2^{(\mathrm{II})}$) were fluctuating quantities. The only constraint was that the *total* number of particles was the same for both species, i.e., $N_1 \equiv N_1^{(\mathrm{I})} + N_1^{(\mathrm{II})} = N_2^{(\mathrm{I})} + N_2^{(\mathrm{II})} \equiv N_2 = N/2$. In the condensation problem the *global* density $\rho = N/(V^{(\mathrm{I})} + V^{(\mathrm{II})})$ was fixed (in all the cases $\rho^* = 0.3$, a value slightly below the expected critical density) and then varied the temperature T (below the critical temperature). The measured output quantities were the partial densities $\rho^{(\mathrm{I})} = N^{(\mathrm{I})}/V^{(\mathrm{I})}$ and $\rho^{(\mathrm{II})} = N^{(\mathrm{II})}/V^{(\mathrm{II})}$, where $N^{(\gamma)} = N_1^{(\gamma)} + N_2^{(\gamma)}$ is the total number of particles in box γ =I, II. Note that $(\rho^{(\mathrm{II})} - \rho)/(\rho - \rho^{(\mathrm{I})}) = V^{(\mathrm{I})}/V^{(\mathrm{II})}$. In contrast, in the demixing problem T (above the critical temperature) was fixed and ρ was varied, the output observables being the local mole fractions $x_1^{(\mathrm{I})} = N_1^{(\mathrm{I})}/N^{(\mathrm{I})}$ and $x_1^{(\mathrm{II})} = N_1^{(\mathrm{II})}/N^{(\mathrm{II})}$. In this case, the lever rule is $(x_1^{(\mathrm{II})} - \frac{1}{2})/(\frac{1}{2} - x_1^{(\mathrm{I})}) = N^{(\mathrm{I})}/N^{(\mathrm{II})}$.

The total number of particles of each species was $N_1 = N_2 = 250$, what was checked to be sufficient for our purposes. The number of MC steps used was 50–100$\times 10^6$ for the equilibration (longer near the critical point) and 100–200$\times 10^6$ for the production.

4.3.2 Gas-liquid coexistence

Results for the gas-liquid transition are depicted in Fig. 4.3 in the temperature-density plane. Some representative numerical values for models A0, B0, I0, and J0 are tabulated in Table 4.2. In this case, one of the two simulation boxes (I=g) contains the gas phase and the other one (II=l) contains the liquid phase. Since $\rho_g < \rho < \rho_l$, the choice of the global density ρ establishes a natural bound as to how close to the critical point the measured binodal curve can be. In fact,

TABLE 4.2: Gas-liquid coexistence properties for models A0, B0, I0, and J0, as obtained from GEMC simulations. T^* is the reduced temperature, ρ^*_γ is the reduced density of the gas ($\gamma = g$) and liquid ($\gamma = l$) phases, $N^{(g)}$ is the average number of particles in the gas box, and $U_{\rm ex}^{(\gamma)}/N^{(\gamma)}$ is the excess internal energy per particle in box γ.

Model	T^*	ρ^*_g	ρ^*_l	$N^{(g)}/N$	$-U_{\rm ex}^{(g)}/\epsilon N^{(g)}$	$-U_{\rm ex}^{(l)}/\epsilon N^{(l)}$
A0	0.075	0.1994(6)	0.590(1)	0.493(2)	1.69(1)	1.796(7)
	0.1	0.214(2)	0.559(5)	0.535(4)	1.785(4)	1.780(8)
	0.125	0.223(1)	0.530(6)	0.556(3)	1.63(9)	1.71(5)
	0.15	0.231(1)	0.503(4)	0.574(4)	1.60(1)	1.78(1)
	0.175	0.250(2)	0.455(8)	0.630(6)	1.42(1)	1.632(9)
B0	0.3	0.112(2)	0.887(5)	0.284(5)	1.6(1)	3.27(1)
	0.325	0.128(1)	0.839(3)	0.324(3)	0.761(1)	3.239(7)
	0.328	0.145(5)	0.771(5)	0.363(9)	0.88(2)	2.99(1)
	0.33	0.15(1)	0.73(1)	0.380(1)	0.95(1)	3.016(9)
	0.335	0.18(3)	0.65(3)	0.45(1)	1.0(7)	2.83(2)
	0.337	0.23(5)	0.54(5)	0.59(1)	1.273(4)	2.36(4)
I0	0.3	0.202(3)	0.61(1)	0.5146(7)	2.48(6)	3.04(1)
	0.325	0.211(5)	0.58(2)	0.5371(6)	1.76(4)	2.765(8)
	0.35	0.24(1)	0.50(3)	0.612(3)	1.24(3)	2.30(1)
	0.36	0.25(2)	0.45(4)	0.657(5)	1.01(1)	1.85(5)
	0.365	0.28(3)	0.42(5)	0.71(1)	0.96(2)	1.6(1)
J0	0.2	0.10(1)	0.93(3)	0.249(5)	1.67(2)	2.48(3)
	0.25	0.14(1)	0.83(5)	0.34(1)	0.82(2)	2.25(3)
	0.255	0.17(2)	0.70(5)	0.433(9)	0.90(2)	1.99(2)
	0.257	0.19(3)	0.60(6)	0.62(6)	1.10(7)	1.5(2)

TABLE 4.3: Mole fractions in the gas and liquid boxes in model I0 at different temperatures and with a global density $\rho^* = 0.3$. For the gas and liquid densities, see Table 4.2. Because of the symmetry under label exchange $1 \leftrightarrow 2$, we have adopted the criterion $x_1^{(g)} \leq x_2^{(g)}$ without loss of generality.

T^*	$x_1^{(g)}$	$x_1^{(l)}$
0.3	0.03(1)	0.992(6)
0.325	0.09(2)	0.98(1)
0.35	0.18(3)	0.955(15)
0.36	0.26(3)	0.93(3)
0.365	0.34(3)	0.89(4)

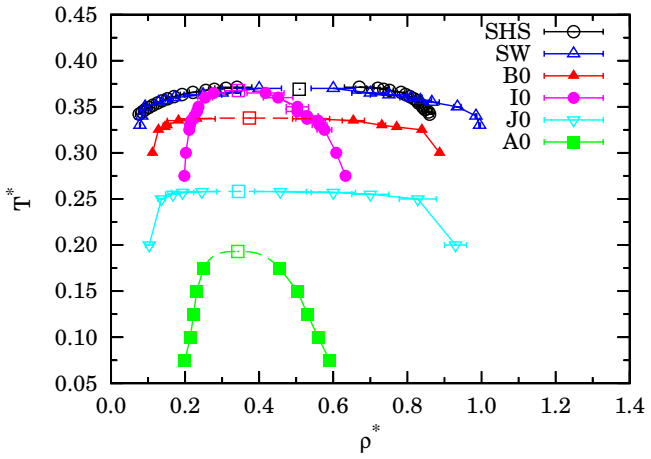

FIGURE 4.3: Gas-liquid binodals for models SW, B0, I0, J0, and A0. The points indicated as SHS in the legend are grand canonical MC (GCMC) results taken from Ref. [66], where the actual one-component SHS model was studied. The remaining results are those obtained in this work from GEMC simulations. In each case, the solid line is a guide to the eye, while the dashed line is the result of the extrapolation to the critical point, which is represented by a square.

$N^{(g)} \to 0$ if $\rho_l \to \rho$, while $N^{(g)} \to N$ if $\rho_g \to \rho$. As is apparent from the values of $N^{(g)}/N$ in Table 4.2, the latter scenario seems to take place in our case $\rho^* = 0.3$.

Although not strictly enforced, we observed that $N_1^{(g)} \simeq N_2^{(g)}$ and $N_1^{(l)} \simeq N_2^{(l)}$ (so both boxes were practically equimolar) in models A0, B0, and J0. On the other hand, in the case of model I0 the final equilibrium state was non-equimolar (despite the fact that, as said before, $N_1 = N_2$ globally), the low-density box having a more disparate composition than the high-density box. The mole fraction values are shown in Table 4.3. Thus, in contrast to models A0, B0, and J0, the GEMC simulations at fixed temperature and global density $\rho^* = 0.3$ spontaneously drove the system I0 into two coexisting boxes differing both in density and composition. This *spontaneous demixing* phenomenon means that in model I0 the equimolar binodal curve must be metastable with respect to demixing and so it was not observed in simulations. It is important to remark that, while the equimolar binodal must be robust with respect to changes in the global density ρ (except for the bound $\rho_g < \rho < \rho_l$ mentioned above), the non-equimolar binodal depends on the value of ρ.

In addition to cases SW, B0, I0, J0, and A0, we have also included in Fig.

4.3, for completeness, numerical results obtained by Miller and Frenkel [66] on the one-component Baxter's sticky-hard-sphere (SHS) model [32]. As expected, they agree quite well with our short-range SW results, the only qualitative difference being a liquid branch at slightly larger densities.

In order to determine the critical point (T_c^*, ρ_c^*) we empirically extrapolated the GEMC binodals using the law of rectilinear "diameters" [79], $\frac{1}{2}\left(\rho_g^* + \rho_l^*\right) = \rho_c^* + A|T^* - T_c^*|$, and the Wegner expansion [79, 80] for the width of the coexistence curve, $\rho_l^* - \rho_g^* = B|T^* - T_c^*|^{\beta_I}$. The critical coordinates (T_c^*, ρ_c^*) and the coefficients A and B are taken as fitting parameters. The four points corresponding to the two highest temperatures were used for the extrapolation in each case. We remark that data do not extend sufficiently close to the critical region to allow for quantitative estimates of critical exponents and non-universal quantities. However, assuming that the models belong to the three-dimensional Ising universality class, we chose $\beta_I = 0.325$. The numerical values obtained by this extrapolation procedure will be presented in Table 4.5 below.

The decrease in the critical temperatures and densities in going from the one-component SW fluid to model B0 and then to model A0 is strongly reminiscent of an analogous trend present in the unconstrained one-patch Kern–Frenkel model upon decrease of the coverage [15].

It is interesting to remark that, even though the influence of attraction in model A0 is strongly inhibited by the up-down constrained orientation ($\epsilon_{ij} = \epsilon\delta_{i1}\delta_{j2}$), this model exhibits a gas-liquid transition. This surprising result was preliminarily supported by canonical NVT MC simulations in Sec. 3.6.4, but now it is confirmed by the new and more appropriate GEMC simulations presented in this chapter. Given the patch geometry and interactions in model A0, one might expect the formation of a lamellar-like liquid phase (approximately) made of alternating layers (up-down-up-down-$\cdots$) of particles with the same orientation. This scenario is confirmed by snapshots of the liquid-phase box, as illustrated by Fig. 4.4.

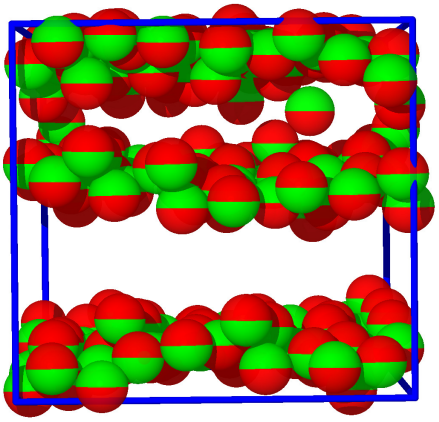

FIGURE 4.4: Snapshot of the liquid-phase box in model A0 at $T^* = 0.15$.

The Kern–Frenkel analogy is not applicable to the isotropic models I0 and J0. Model J0 presents a critical point intermediate between those of models B0 and A0, as expected. However, while the decrease in the total average attractive strength is certainly one of the main mechanisms dictating the location of the gas-liquid coexistence curves, it cannot be the only discriminating factor, as shown by the results for the isotropic model I0, where the critical temperature is higher and the binodal curve is narrower than that corresponding to the anisotropic model B0. This may be due to the fact that, as said before, the binodal curve in model I0 is not equimolar and this lack of equimolarity is expected to extend to the critical point, as can be guessed from the trends observed in Table 4.3. In other words, two demixed phases can be made to coexist at a higher temperature and with a smaller density difference than two mixed phases.

4.3.3 Demixing transition

The bi-component nature of the systems raises the question of a possible demixing transition in which a rich-1 phase coexists with a rich-2 phase at a given temperature T, provided the density is larger than a certain critical consolute density $\rho_{cc}(T)$. The points $\rho_{cc}(T)$ or, reciprocally, $T_{cc}(\rho)$ define the so-called λ-line [81].

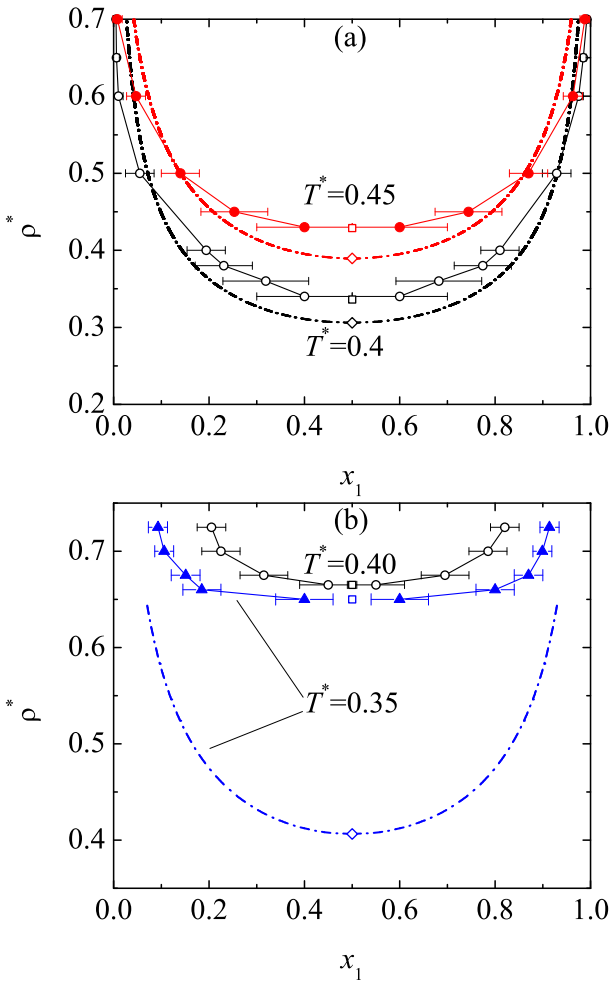

FIGURE 4.5: Demixing curves for models (a) I0 and (b) B0 at two temperatures, as obtained from GEMC simulations, in the density-mole fraction plane. In each case, the solid line is a guide to the eye, while the critical consolute point is represented by a square. For model I0 we found $\rho^*_{cc}(T^* = 0.4) = 0.336$ and $\rho^*_{cc}(T^* = 0.45) = 0.429$; for model B0 the results are $\rho^*_{cc}(T^* = 0.35) = 0.650$ and $\rho^*_{cc}(T^* = 0.4) = 0.665$. The dashed-dotted lines are the theoretical predictions (see Sec. 4.4.3).

The interplay between the gas-liquid and demixing transitions is a very interesting issue and was discussed in a general framework by Wilding et al. [82].

Since all the spheres have the same size, a necessary condition for demixing in the case of *isotropic* potentials is that the like attractions must be sufficiently stronger than the unlike attractions [82, 83]. Assuming the validity of this condition to anisotropic potentials and making a simple estimate based on the virial expansion, one finds that demixing requires the coefficient of x_1x_2 in the second virial coefficient to be positive, i.e., $2e^{\epsilon_{11}/k_BT} > e^{\epsilon_{12}/k_BT} + e^{\epsilon_{21}/k_BT}$. While this

TABLE 4.4: Demixing coexistence properties for models I0 and B0, as obtained from GEMC simulations. T^* is the reduced temperature, ρ^* is the reduced density, and $x_1^{(\gamma)}$ is the mole fraction of species 1 in each one of the two coexisting phases γ =I, II.

Model	T^*	ρ^*	$x_1^{(\mathrm{I})}$	$x_1^{(\mathrm{II})}$
I0	0.4	0.7	0.005(5)	0.992(5)
		0.65	0.006(6)	0.985(6)
		0.6	0.01(1)	0.97(1)
		0.5	0.05(3)	0.93(3)
		0.4	0.19(4)	0.81(4)
		0.38	0.23(6)	0.77(6)
		0.36	0.32(9)	0.68(9)
		0.34	0.4(1)	0.6(1)
	0.45	0.7	0.01(1)	0.99(1)
		0.6	0.05(2)	0.96(2)
		0.5	0.14(4)	0.87(4)
		0.45	0.25(7)	0.74(7)
		0.43	0.4(1)	0.6(1)
B0	0.35	0.725	0.09(2)	0.91(2)
		0.7	0.11(2)	0.90(2)
		0.675	0.15(3)	0.87(3)
		0.66	0.18(4)	0.80(4)
		0.65	0.40(6)	0.60(6)
	0.4	0.725	0.20(3)	0.82(3)
		0.7	0.22(4)	0.78(4)
		0.675	0.31(5)	0.69(5)
		0.665	0.45(6)	0.55(6)

demixing criterion is only approximate, it suggests that, out of the five models considered, only models B0 and I0 are expected to display demixing transitions. As a matter of fact, we have already discussed the spontaneous demixing phenomenon taking place in model I0 when a low-density phase and a high-density phase are in mutual equilibrium. In this section, however, we are interested in the segregation of the system, at a given T and for $\rho > \rho_{cc}(T)$, into a rich-2 phase I with $x_1^{(\mathrm{I})} = x_d(\rho) < \frac{1}{2}$ and a *symmetric* rich-1 phase II with $x_1^{(\mathrm{II})} = 1 - x_d(\rho) > \frac{1}{2}$, both phases at the *same* density.

GEMC simulation results are presented in Fig. 4.5 and Table 4.4. We observe that, as expected, $x_1^{(\mathrm{I})} = 1 - x_1^{(\mathrm{II})}$ within statistical fluctuations. We have also

checked that $\rho^{(\mathrm{I})} \simeq \rho^{(\mathrm{II})}$, even though this equality is not artificially enforced in the simulations. Such equality is also equivalent to $\rho^{(\mathrm{I})} \simeq \rho$ and we checked that it was satisfied within a standard deviation of $0.02\sigma^{-3}$ in all cases considered in Table 4.4. To obtain the critical consolute density ρ_{cc}^{*} for each temperature, we extrapolated the data again according to the Ising scaling relation $\frac{1}{2} - x_d(\rho) = C(\rho - \rho_{cc})^{\beta_I}$.

It is interesting to note that just the absence of attraction when a particle of species 2 is below a particle of species 1 ($\epsilon_{21} = 0$) in model B0 is sufficient to drive a demixing transition. However, as expected, at a common temperature (see $T^* = 0.4$ in Fig. 4.5), demixing requires higher densities in model B0 than in model I0.

As said above, the interplay of condensation and demixing is an interesting problem by itself [82, 84]. Three alternative scenarios are in principle possible for the intersection of the λ-line and the binodal curve: a critical end point, a triple point, or a tricritical point [82]. Elucidation of these scenarios would require grand canonical simulations (rather than GEMC simulations), what is beyond the scope of this thesis.

4.4 Simple analytical theories

Let us now compare the above numerical results with simple theoretical predictions. The solution of integral equation theories for anisotropic interactions and/or multicomponent systems requires formidable numerical efforts, with the absence of explicit expressions often hampering physical insight. Here we want to deal with simple, purely analytical theories that yet include the basic ingredients of the models.

First, as already done in Ch. 3, we take advantage of the short-range of the

attractive well ($\Delta/\sigma = 0.05$) to map the different SW interactions into SHS interactions parameterized by the "stickiness" parameters

$$t_{ij} \equiv \frac{1}{12\tau_{ij}} \equiv \frac{\Delta}{\sigma}\left(1+\frac{\Delta}{\sigma}+\frac{\Delta^2}{3\sigma^2}\right)\left(e^{\epsilon_{ij}/k_BT}-1\right), \tag{4.3}$$

which combine the energy and length scales. This mapping preserves the exact second virial coefficient of the genuine SW systems, namely

$$\frac{B_2}{B_2^{\rm HS}} = 1 - 3t_{11} + 3x_1x_2(2t_{11} - t_{12} - t_{21}), \tag{4.4}$$

where $B_2^{\rm HS} = 2\pi\sigma^3/3$ is the HS coefficient. The exact expression of the third virial coefficient B_3 in the SHS limit for arbitrary t_{ij} is (see Appendix C)

$$\begin{aligned}\frac{B_3}{B_3^{\rm HS}} &= 1 - 6t_{11} + \frac{72}{5}t_{11}^2 - \frac{48}{5}t_{11}^3 - \frac{6}{5}x_1x_2\Big[(12t_{11}-5)\\ &\times(2t_{11}-t_{12}-t_{21}) - 8t_{11}\left(t_{11}^2 - t_{12}t_{21}\right)\\ &-2(4t_{11}-3)\left(2t_{11}^2 - t_{12}^2 - t_{21}^2\right) + 2\alpha\left(t_{12}-t_{21}\right)^2\Big],\end{aligned} \tag{4.5}$$

where $B_3^{\rm HS} = 5\pi^2\sigma^6/18$ and α is given by Ec. (3.79).

4.4.1 Equations of state

One advantage of the SW $\to$ SHS mapping is that the Percus–Yevick (PY) integral equation is exactly solvable for SHS mixtures with *isotropic* interactions ($t_{12} = t_{21}$) [47, 48]. In principle, that solution can be applied to the models SW, I0, and J0 represented in Fig. 4.2. On the other hand, if $t_{11} \neq 0$ (models SW and I0), the PY solutions are related to algebraic equations of second (SW) or fourth (I0) degrees, what creates the problem of disappearance of the physical solution for large enough densities or stickiness. In particular, we have observed that the breakdown of the solution preempts the existence of a critical point in model I0. However, in the case of model J0 ($t_{11} = 0$, $t_{12} = t_{21} = t$), the PY solution reduces to a *linear* equation whose solution is straightforward. Following the virial (v) and the energy (u) routes, the respective expressions for the compressibility factor $Z \equiv p/\rho k_BT$ have

the form

$$Z^v(\eta,t,x_1) = Z^v_{\rm HS}(\eta) - x_1x_2Z^v_{(1)}(\eta,t) - x_1^2x_2^2Z^v_{(2)}(\eta,t), \tag{4.6a}$$

$$Z^u(\eta,t,x_1) = Z^u_{\rm HS}(\eta) - x_1x_2Z^u_{(1)}(\eta,t), \tag{4.6b}$$

where

$$Z^v_{\rm HS}(\eta) = \frac{1+2\eta+3\eta^2}{(1-\eta)^2} \tag{4.7}$$

is the HS compressibility factor derived from the PY equation via the virial route, $Z^u_{\rm HS}$ is an indeterminate integration constant, and the explicit expressions for $Z^v_{(1)}$, $Z^v_{(2)}$, and $Z^u_{(1)}$ are

$$Z^v_{(1)}(\eta,t) = \frac{24\eta t}{(1-\eta+6\eta t)^2}\left[\frac{1+2\eta}{1-\eta} + 3\eta t\frac{2+2\eta-5\eta^2/2}{(1-\eta)^2} + 6\eta^2t^2\frac{2-4\eta-7\eta^2}{(1-\eta)^3}\right], \tag{4.8a}$$

$$Z^v_{(2)}(\eta,t) = \frac{288\eta^3t^2(2+\eta)}{(1-\eta+6\eta t)^3}\left[\frac{1}{1-\eta} - t\frac{2-11\eta}{(1-\eta)^2} + t^2\frac{2-10\eta+61\eta^2/2}{(1-\eta)^3}\right], \tag{4.8b}$$

$$Z^u_{(1)}(\eta,t) = \frac{6\eta}{(1-\eta)^2}\left[\frac{2t(2+\eta)}{1-\eta+6\eta t} + \ln\frac{1-\eta+6\eta t}{1-\eta}\right]. \tag{4.8c}$$

As apparent from Fig. 4.2, model A0 is a close relative of model J0. However, the fact that $\epsilon_{12} \neq \epsilon_{21} = 0$ (or $t_{12} \neq t_{21} = 0$) makes the interaction anisotropic and prevents the PY equation from being exactly solvable in this case. On the other hand, the RFA worked out in Ch. 3 applies to models with $t_{12} \neq t_{21}$ and reduces to the PY solution in the case of isotropic models ($t_{12} = t_{21}$). The RFA solution for model A0 yields once more a linear equation. The virial and energy equations of state are again of the forms (4.6a) and (4.6b), respectively, with expressions for $Z_1^{(v)}$, $Z_2^{(v)}$, and $Z_1^{(u)}$ given by [see Eqs. (3.63) and (3.67)]

$$Z^v_{(1)}(\eta,t) = \frac{12\eta t}{1-\eta+6\eta t}\left[\frac{1+2\eta}{(1-\eta)^2} + 2\eta t\frac{1-2\eta-7\eta^2/2}{(1-\eta)^3}\right], \tag{4.9a}$$

$$Z^v_{(2)}(\eta,t) = \frac{72\eta^3t^2(2+\eta)}{(1-\eta)^3(1-\eta+6\eta t)}, \tag{4.9b}$$

$$Z^u_{(1)}(\eta,t) = \frac{3\eta}{(1-\eta)^2}\left[\frac{2t(2+\eta)}{1-\eta+6\eta t} + \ln\frac{1-\eta+6\eta t}{1-\eta}\right]. \tag{4.9c}$$

In the RFA solution for model A0 the exact third virial coefficient (4.5) is recovered by the interpolation relations [see Eq. (3.79)]

$$\begin{aligned} Z &= Z_{\rm HS}^{\rm CS} + \alpha \left(Z^v - Z_{\rm HS}^v\right) + (1-\alpha)\left(Z^u - Z_{\rm HS}^u\right) \\ &= Z_{\rm HS}^{\rm CS} - x_1 x_2 \left[\alpha Z_{(1)}^v + (1-\alpha) Z_{(1)}^u\right] - x_1^2 x_2^2 \alpha Z_{(2)}^v, \end{aligned} \tag{4.10}$$

where $Z_{\rm HS}^{\rm CS}$ is given by Eq. (3.68) and the interpolation weight α is given by Eq. (3.79). By consistency, Eq. (4.10) will also be employed in the PY solution of model J0.

In the cases of models with $\epsilon_{11} \neq 0$ (i.e., SW, B0, and I0), the PY and RFA theories fail to have physical solutions in regions of the temperature-density plane overlapping with the gas-liquid transition. In order to circumvent this problem, we adopt here a simple perturbative approach:

$$Z = Z_{\rm ref} + \left(B_2 - B_2^{\rm ref}\right)\rho + \left(B_3 - B_3^{\rm ref}\right)\rho^2, \tag{4.11}$$

where $Z_{\rm ref}$ is the compressibility factor of a reference model and $B_2^{\rm ref}$ and and $B_3^{\rm ref}$ are the associated virial coefficients. As a natural choice (see Fig. 4.2), we take the models J0, A0, and HS (which lie on the plane $\epsilon_{11}/\epsilon = 0$) as reference systems for the models SW, B0, and I0 (which lie on the plane $\epsilon_{11}/\epsilon = 1$), respectively. More specifically,

$$Z_{\rm SW} = Z_{\rm J0} + \left(B_2^{\rm SW} - B_2^{\rm J0}\right)\rho + \left(B_3^{\rm SW} - B_3^{\rm J0}\right)\rho^2, \tag{4.12a}$$

$$Z_{\rm B0} = Z_{\rm A0} + \left(B_2^{\rm B0} - B_2^{\rm A0}\right)\rho + \left(B_3^{\rm B0} - B_3^{\rm A0}\right)\rho^2, \tag{4.12b}$$

$$Z_{\rm I0} = Z_{\rm HS}^{\rm CS} + \left(B_2^{\rm I0} - B_2^{\rm HS}\right)\rho + \left(B_3^{\rm I0} - B_3^{\rm HS}\right)\rho^2. \tag{4.12c}$$

Here, $Z_{\rm J0}$ and $Z_{\rm A0}$ are given by Eq. (4.10) (with the corresponding expressions of $Z_{(1)}^v$, $Z_{(2)}^v$, and $Z_{(1)}^u$) and the virial coefficients are obtained in each case from Eqs. (4.4) and (4.5) with the appropriate values of t_{11}, t_{12}, and t_{21}.

From the explicit knowledge of $Z(\eta, t, x_1)$, standard thermodynamic relations

allow one to obtain the free energy per particle $a(\eta, t, x_1)$ and the chemical potentials $\mu_i(\eta, t, x_1)$ as

$$\beta a(\eta, t, x_1) = \int_0^\eta d\eta' \, \frac{Z(\eta', t, x_1) - 1}{\eta'} + x_1 \ln(x_1 \eta) + (1 - x_1) \ln[(1 - x_1)\eta] + \text{const}, \tag{4.13a}$$

$$\beta \mu_1(\eta, t, x_1) = \beta a(\eta, t, x_1) + Z(\eta, t, x_1) + (1 - x_1) \frac{\partial \beta a(\eta, t, x_1)}{\partial x_1}, \tag{4.13b}$$

$$\mu_2(\eta, t, x_1) = \mu_1(\eta, t, 1 - x_1). \tag{4.13c}$$

4.4.2 Gas-liquid coexistence

The critical point (η_c, t_c) of the gas-liquid transition is obtained from the well-known condition that the critical isotherm in the pressure-density plane presents an inflection point with horizontal slope at the critical density [30]. In terms of the compressibility factor Z, this implies

$$\left. \frac{\partial \left[\eta Z(\eta, t_c, 1/2)\right]}{\partial \eta} \right|_{\eta=\eta_c} = \left. \frac{\partial^2 \left[\eta Z(\eta, t_c, 1/2)\right]}{\partial \eta^2} \right|_{\eta=\eta_c} = 0, \tag{4.14}$$

where equimolarity ($x_1 = \frac{1}{2}$) has been assumed. For temperatures below the critical temperature (i.e., $t > t_c$) the packing fractions η_g and η_l of the gas and liquid coexisting phases are obtained from the conditions of equal pressure (mechanical equilibrium) and equal chemical potential (chemical equilibrium) [30], i.e.,

$$\eta_g Z(\eta_g, t, 1/2) = \eta_l Z(\eta_l, t, 1/2), \tag{4.15a}$$

$$\mu_1(\eta_g, t, 1/2) = \mu_1(\eta_l, t, 1/2). \tag{4.15b}$$

In order to make contact with the GEMC results, the theoretical values of t_c have been mapped onto those of T_c^* by inverting Eq. (4.3), namely

$$\frac{1}{T^*} = \ln \left[1 + \frac{t}{(\Delta/\sigma)\,(1 + \Delta/\sigma + \Delta^2/3\sigma^2)} \right] \tag{4.16}$$

with $\Delta/\sigma = 0.05$.

TABLE 4.5: Comparison between the critical points measured in simulations with those obtained from theoretical approaches.

Method	SW	B0	I0	J0	A0
		T_c^*			
Simulation	0.369[1]	0.338[2]	0.368[2]	0.258[2]	0.193[2]
Our theory	0.377	0.341	0.331	0.278	0.214
Noro–Frenkel	0.369	0.335	0.297	0.297	0.247
		ρ_c^*			
Simulation	0.508[1]	0.373[2]	0.344[2]	0.344[2]	0.342[2]
Our theory	0.356	0.330	0.366	0.376	0.359

[1] GCMC results for the one-component SHS fluid From Ref. [66]
[2] Our GEMC simulation results

Table 4.5 compares the critical points obtained in simulations for the one-component SW fluid (in the SHS limit) and for models B0, I0, J0, and A0 (see Fig. 4.2) with those stemming from our simple theoretical method. Results from the Noro–Frenkel (NF) corresponding-state criterion [68], according to which $B_2/B_2^{\mathrm{HS}} = -1.21$ at the critical temperature, are also included. We observe that, despite its simplicity and the lack of fitting parameters, our fully analytical theory predicts quite well the location of the critical point, especially in the case of T_c^*. It improves the estimates obtained from the NF criterion, except in the SW case, where, by construction, the NF rule gives the correct value. In what concerns the gas-liquid binodals, Fig. 4.6 shows that the theoretical curves agree fairly well with the GEMC data, except in the cases of models I0 and A0, where the theoretical curves are much flatter than the simulation ones. The lack of agreement with the binodal curve of model I0 can be partially due to the fact that in the theoretical treatment the two coexisting phases are supposed to be equimolar, while this is not the case in the actual simulations (see Table 4.3).

4.4.3 Demixing transition

In the case of the demixing transition, the critical consolute density η_{cc} at a given temperature is obtained from

$$\left.\frac{\partial^2 a(\eta_{cc}, t, x_1)}{\partial x_1^2}\right|_{x_1=\frac{1}{2}} = 0. \tag{4.17}$$

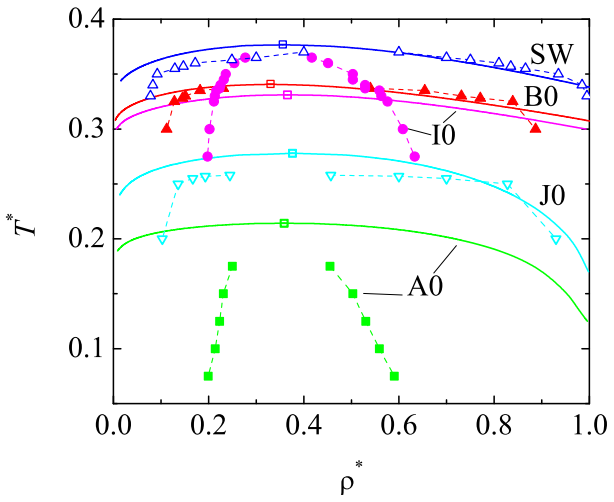

FIGURE 4.6: Gas-liquid binodals for models SW, A0, B0, I0, and J0, as obtained from our theoretical method (solid lines). The critical points are represented by open squares. The symbols joined by dashed lines correspond to GEMC data (see Fig. 4.3).

For $\eta > \eta_{cc}$, the demixing mole fraction $x_1 = x_d(\eta)$ is the solution to

$$\mu_1(\eta, t, x_d) = \mu_1(\eta, t, 1 - x_d). \tag{4.18}$$

In terms of the compressibility factor Z, Eqs. (4.17) and (4.18) can be rewritten as

$$\int_0^{\eta_{cc}} d\eta \, \frac{\partial^2 Z(\eta, t, x_1)/\partial x_1^2|_{x_1=\frac{1}{2}}}{\eta} = -4, \tag{4.19a}$$

$$\int_0^{\eta} d\eta' \, \frac{\partial Z(\eta', t, x_d)/\partial x_d}{\eta'} = \ln \frac{1 - x_d}{x_d}, \tag{4.19b}$$

respectively.

The perturbative approximations for models I0 and B0 succeed in predicting demixing transitions, even though their respective reference systems (HS and A0) do not demix. In the case of model I0, the critical consolute densities are $\rho_{cc}^*(T^* = 0.4) = 0.306$ and $\rho_{cc}^*(T^* = 0.45) = 0.390$, which are about 9% lower than the values obtained in GEMC simulations. In the case of model B0, our simple theory predicts a critical consolute point only if $t > 0.7667$, i.e., if $T^* < 0.364$, so no demixing is predicted at $T^* = 0.4$, in contrast to the results of the simulations. At $T^* = 0.35$ the theoretical prediction is $\rho_{cc}^* = 0.406$, a value about 39% smaller than the GEMC one. The theoretical demixing curves at $T^* = 0.4$ and $T^* = 0.45$

for model I0 and at $T^* = 0.35$ for model B0 are compared with the GEMC results in Fig. 4.5. We can observe a fairly good agreement in the case of model I0, but not for model B0. In the latter case, the theoretical curve spans a density range comparable to that of model I0, while simulations show a much flatter demixing curve.

4.5 Summary and remarks

In this chapter, we have proposed a class of binary-mixture Janus fluids with up-down constrained orientations. The class encompasses, as particular cases, the conventional one-component SW fluid, mixtures with isotropic attractive interactions only between like particles (model I0) or unlike particles (model J0), and genuine Janus fluids with anisotropic interactions and different patch-patch affinities (models A0 and B0). Both GEMC numerical simulations and simple theoretical approximations have been employed to analyze the gas-liquid transition under *global* equimolar conditions for the five models and the demixing transition for the two models (I0 and B0) where the attraction between like particles is stronger than between unlike ones. The theoretical analysis employed a mapping onto SHS interactions, that were then studied by means of the PY theory (model J0), the RFA (model A0), and low-density virial corrections (models SW, I0, and B0), with semi-quantitative agreement with numerical simulations.

5

Final outlook and conclusions

This thesis has studied various fluid systems of Janus particles. Our work started with the one-dimensional case, for which we defined a particular system hard of rods (Sec. 2.2), basically a general m-component mixture with anisotropic interactions. If we define $m = 2$ (binary mixture), we can easily get the radial distribution functions $g_{ij}(r)$ and the thermodynamic quantities, corresponding to the Kern–Frenkel case.

An interesting result is the absence of a Fisher–Widom transition between an oscillatory asymptotic decay of $h_{ij}(r) \equiv g_{ij}(r) - 1$ (if the repulsive part of the interaction dominates) and a monotonic asymptotic decay (if the attractive part of the interaction dominates), in contrast to what happens in the case of the one-dimensional isotropic SW fluid [23]. This is a consequence of the inhibition

of attractive forces, as they are restricted to pairs of particles with their active faces facing each other. However, a structural crossover exists between an oscillatory decay with a wavelength smaller than twice the hard-core diameter (at high temperatures) and an oscillatory decay with a larger wavelength (at low temperatures). The phase diagram representing this structural crossover presents a "critical" point, as illustrated by Fig. 2.4.

In the final part of the one-dimensional study we performed NVT MC simulations which results we compared with the ones from the exact solution derived previously. The simulations, carried out for annealed systems, exhibited an excellent agreement with the theory, even though this theoretical solution was developed for the quenched system.

In order to proceed with the study in three dimensions, we defined the proper model in Ch. 3, which turns out to be a binary mixture of Janus particles with two fixed orientations, with three interactions being HS and the remaining one being SW or SHS.

Within the RFA methodology, all three standard routes to thermodynamics (compressibility, virial, and energy) were considered. To them we added a weighted average of the virial and energy routes with a weight fixed as to reproduce the exact third virial coefficient. Somewhat surprisingly, our results indicate that only the compressibility route fails to display a full critical behavior with a well-defined critical point. The existence of a critical point and a (possibly metastable towards the solid formation) gas-liquid phase transition in our model (despite the fact that attractive interactions are partially inhibited) are supported by the NF generalized principle of corresponding states [68] and by NVT simulations results.

Finally in Ch. 4, we studied the phase diagram of three-dimensinal Janus particles with different classes of face-to-face interactions (see Figs. 4.1 and 4.2).

Interestingly, the presence of attraction in only one out of the four possible patch-patch interactions (model A0) turns out to be enough to make the gas-liquid transition possible. Reciprocally, the lack of attraction in only one of the two possible patch-patch interactions between unlike particles (model B0) is enough to produce a demixing transition. The exact simulation results show that the coexisting gas and liquid phase are close to the equimolar composition condition used in the approximate liquid state theories except for the I0 model. As the average attraction is gradually decreased, the gas-liquid critical point shifts to lower temperatures (except for an interesting inversion of tendency observed when going from the isotropic model I0 to the anisotropic model B0) and lower densities. Moreover, the coexistence region progressively shrinks, in analogy with what is observed in the unconstrained one-component Janus fluid [52, 85] and in the empty liquid scenario [86]. On the other hand, the imposed constraint in the orientation of the attractive patches does not allow for the formation of those inert clusters [8, 43, 44] which in the unconstrained one-component Janus fluid are responsible for a re-entrant gas branch [8, 15, 42].

A

Consistency tests of the exact solution for one-dimensional systems

A.1 Virial route

In a general one-dimensional mixture (with isotropic or anisotropic interactions), the virial equation of state reads

$$\frac{\beta p}{\rho} = 1 - \rho\beta \sum_{i,j} x_i x_j \int_0^\infty dr\, r g_{ij}(r) \frac{\partial \phi_{ij}(r)}{\partial r}. \tag{A.1}$$

Now, since the interaction $\phi_{ij}(r)$ does not extend beyond the nearest neighbors, we can replace $g_{ij}(r) \to \rho_j^{-1} p_{ij}^{(1,+)}(r) = \rho^{-1} K_{ij} e^{-\beta p r} e^{-\beta \phi_{ij}(r)}$ in Eq. (A.1), so that

$$\frac{\beta p}{\rho} = 1 + \sum_{i,j} x_i x_j K_{ij} \int_0^\infty dr\, r e^{-\beta p r} \frac{\partial e^{-\beta \phi_{ij}(r)}}{\partial r}. \tag{A.2}$$

Integrating by parts,

$$\frac{\beta p}{\rho} = 1 - \sum_{i,j} x_i x_j K_{ij} \int_0^\infty dr\, \left(1 + p \frac{\partial}{\partial p}\right) e^{-\beta p r} e^{-\beta \phi_{ij}(r)}. \tag{A.3}$$

This equation can be rewritten as

$$\frac{1}{\rho} = \frac{1}{\beta p} - \sum_{i,j} x_i x_j K_{ij} \left(\Omega'_{ij} + \frac{\Omega_{ij}}{\beta p}\right) = -\sum_{i,j} x_i x_j K_{ij} \Omega'_{ij}, \tag{A.4}$$

where in the last step we have taken into account the normalization condition (2.26). Equation (A.4) is the generalization of Eq. (2.35) to an arbitrary number of components.

A.2 Compressibility route

According to this route,

$$\begin{aligned} \chi &\equiv k_B T \left(\frac{\partial \rho}{\partial p}\right)_{T,x_1} \\ &= \frac{\left[1 + \rho x_1 \widetilde{h}_{11}(0)\right]\left[1 + \rho x_2 \widetilde{h}_{22}(0)\right] - \rho^2 x_1 x_2 \widetilde{h}_{12}(0) \widetilde{h}_{21}(0)}{1 + \rho x_1 x_2 \left[\widetilde{h}_{11}(0) + \widetilde{h}_{22}(0) - \widetilde{h}_{12}(0) - \widetilde{h}_{21}(0)\right]}, \end{aligned} \tag{A.5}$$

where $\widetilde{h}_{ij}(\mathbf{k}) = \int dr\, e^{\mathrm{i}\mathbf{k}\cdot\mathbf{r}} h_{ij}(\mathbf{r})$ is the Fourier transform of the total correlation function $h_{ij}(\mathbf{r})$, i being the imaginary unit. In the particular case of one-dimensional systems,

$$\widetilde{h}_{ij}(k_x) = \widetilde{h}_{ji}(-k_x) = \left[H_{ij}(s) + H_{ji}(-s)\right]_{s=\mathrm{i}k_x}, \tag{A.6}$$

so that the zero wavenumber limit is

$$\widetilde{h}_{ij}(0) = \widetilde{h}_{ji}(0) = \lim_{s\to 0} \left[G_{ij}(s) + G_{ji}(-s) \right], \tag{A.7}$$

where Eq. (2.17) has been taken into account. Making use of Eqs. (2.16), (2.23), and (2.31a)–(2.32), and after some algebra, one finds

$$\widetilde{h}_{11}(0) = \rho J - 2\frac{x_2 K_{22}\Omega'_{22}}{x_1 K_{12}\Omega_{12}} - \frac{2}{\rho x_1}, \quad \widetilde{h}_{22}(0) = \rho J - 2\frac{x_1 K_{11}\Omega'_{11}}{x_2 K_{12}\Omega_{12}} - \frac{2}{\rho x_2}, \tag{A.8a}$$

$$\widetilde{h}_{12}(0) = \widetilde{h}_{21}(0) = \rho J + \frac{\Omega'_{12}}{\Omega_{12}} + \frac{\Omega'_{21}}{\Omega_{21}}, \tag{A.8b}$$

where

$$J \equiv x_1^2 K_{11}\Omega''_{11} + x_2^2 K_{22}\Omega''_{22} + x_1 x_2 \left(K_{12}\Omega''_{12} + K_{21}\Omega''_{21} - 2K_{12}\frac{\Omega'_{11}\Omega'_{22} - \Omega'_{12}\Omega'_{21}}{\Omega_{21}} \right). \tag{A.9}$$

By inserting Eqs. (A.8a)–(A.9) into the right-hand side of Eq. (A.5), it can be verified that the resulting expression for the isothermal susceptibility χ indeed coincides with the one obtained as $(\partial\rho/\partial\beta p)_{\beta,x_1}$ from Eq. (2.35). Also, it can be checked that the denominator on the right-hand side of Eq. (A.5) reduces to

$$1 + \rho x_1 x_2 \left[\widetilde{h}_{11}(0) + \widetilde{h}_{22}(0) - \widetilde{h}_{12}(0) - \widetilde{h}_{21}(0) \right] = \sqrt{1 - 4x_1 x_2 R}. \tag{A.10}$$

Therefore, χ never diverges, what confirms the classical proof [87] by van Hove about the absence of phase transitions in one-dimensional nearest-neighbor models.

A.3 Energy route

In general, the excess internal energy per particle in a one-dimensional mixture is

$$u_{\text{ex}} = \rho \sum_{i,j} x_i x_j \int_0^\infty dr\, g_{ij}(r)\phi_{ij}(r). \tag{A.11}$$

As in the case of Eq. (A.1), we can replace $g_{ij}(r) \to \rho^{-1} K_{ij} e^{-\beta pr} e^{-\beta \phi_{ij}(r)}$ in Eq. (A.11). Additionally, taking into account Eq. (2.41), we obtain

$$u_{\text{ex}} = \sum_{i,j} x_i x_j K_{ij} \Omega_{ij} \Upsilon_{ij}. \tag{A.12}$$

Using the properties (2.29), it is straightforward to check that $u_{\text{ex}} = U/N - k_B T/2$, where U is given by Eq. (2.40). Note, however, that Eq. (A.12) applies to any number of components, while Eq. (2.40) refers to binary mixtures only.

B

Sticky-hard-sphere limit in one-dimensional Janus fluids

In the sticky-hard-sphere (SHS) limit, the SW depth ϵ goes to infinity (so that $\theta \to \infty$) while the width $\lambda - 1$ goes to zero by keeping the stickiness parameter $\tau^{-1} \equiv (\lambda - 1)\theta$ fixed. In that case, $\Omega_{12}(s)$ in Eq. (2.43) becomes

$$\Omega_{12}(s) = \Omega(s)\left\{1 - \tau^{-1}\left[1 + \frac{s\Omega'(s)}{\Omega(s)}\right]\right\} = \Omega(s)\left(1 + \tau^{-1}s\right). \tag{B.1}$$

The general equation of state (2.35) reduces to a quadratic equation for the pressure whose physical root is

$$\beta p = \frac{\rho}{1-\rho}\left[1 - F\left(\tau\frac{1-\rho}{\rho}\right)\right], \quad F(z) \equiv \frac{1 + z - \sqrt{(1+z)^2 - 4x_1x_2}}{2}. \tag{B.2}$$

The associated first few virial coefficients are

$$B_2 = 1 - x_1 x_2 \tau^{-1}, \quad B_3 = 1 - x_1 x_2 \tau^{-1} \left(2 - \tau^{-1}\right), \tag{B.3a}$$

$$B_4 = 1 - x_1 x_2 \tau^{-1} \left[3 - 3\tau^{-1} + \tau^{-2} \left(1 + x_1 x_2\right)\right]. \tag{B.3b}$$

Obviously, the same expressions are obtained by taking the SHS limit in Eqs. (2.45a) and (2.45b). In the high-temperature and low-temperature limits, Eq. (B.2) yields

$$\beta p = \frac{\rho}{1-\rho} \left[1 - \frac{\rho}{1-\rho} x_1 x_2 \tau^{-1}\right] + \mathcal{O}(\tau^{-2}), \tag{B.4a}$$

$$\lim_{\tau \to 0} \beta p = \max(x_1, x_2) \frac{\rho}{1-\rho}, \tag{B.4b}$$

where in Eq. (B.4b) we have taken into account that $1 - \sqrt{1 - 4x_1 x_2} = 2 \min(x_1, x_2)$. As expected, Eqs. (B.4a) and (B.4b) are fully consistent with Eqs. (2.46a) and (2.46b), respectively.

In terms of density, the amplitudes (2.29) and (2.30) become

$$K_{11} = \frac{e^{\beta p}}{x_1} \left[\beta p - \frac{\tau + \beta p}{x_1} F\left(\tau \frac{1-\rho}{\rho}\right)\right], \quad K_{22} = \frac{e^{\beta p}}{x_2} \left[\beta p - \frac{\tau + \beta p}{x_2} F\left(\tau \frac{1-\rho}{\rho}\right)\right], \tag{B.5a}$$

$$K_{12} = \frac{\tau e^{\beta p}}{x_1 x_2} F\left(\tau \frac{1-\rho}{\rho}\right), \quad K_{21} = \frac{(\tau + \beta p) e^{\beta p}}{x_1 x_2} F\left(\tau \frac{1-\rho}{\rho}\right). \tag{B.5b}$$

As a consequence, Eq. (2.47) simply reduces to

$$\frac{u_{\text{ex}}}{\epsilon} = -F\left(\tau \frac{1-\rho}{\rho}\right). \tag{B.6}$$

Therefore,

$$u_2 = -x_1 x_2 \tau^{-1}, \quad u_3 = -x_1 x_2 \tau^{-1} (1 - \tau^{-1}), \tag{B.7a}$$

$$u_4 = -x_1 x_2 \tau^{-1} \left[(1 - \tau^{-1})^2 + x_1 x_2 \tau^{-2}\right], \tag{B.7b}$$

$$\frac{u_{\text{ex}}}{\epsilon} = -x_1 x_2 \frac{\rho}{1-\rho} \tau^{-1} + \mathcal{O}(\tau^{-2}), \quad \lim_{\tau \to 0} \frac{u_{\text{ex}}}{\epsilon} = -\min(x_1, x_2). \tag{B.7c}$$

In what concerns the structural properties, we note that in the SHS limit

$$\Psi^{(k_1,k_2)}(s) \to \bar{\Psi}^{(k_1+k_2,0)}(s), \tag{B.8a}$$

$$\theta\left[\Psi^{(k_1,k_2)}(s) - \lambda\Psi^{(k_1-1,k_2+1)}(s)\right] \to \tau^{-1}\bar{\Psi}^{(k_1+k_2-1,1)}(s), \tag{B.8b}$$

where

$$\bar{\Psi}^{(k_1,k_2)}(s) \equiv \frac{[\Omega(s+\beta p)]^{k_1}\, e^{-k_2(s+\beta p)}}{D(s)}. \tag{B.9}$$

As a consequence, Eqs. (2.54a)–(2.54d) become

$$G_{11}(s) = \frac{K_{11}}{\rho}\bar{\Psi}^{(1,0)}(s) + \frac{x_2 K_{11} K_{22}\tau^{-1}}{\rho}\bar{\Psi}^{(1,1)}(s), \tag{B.10a}$$

$$G_{22}(s) = \frac{K_{22}}{\rho}\bar{\Psi}^{(1,0)}(s) + \frac{x_1 K_{11} K_{22}\tau^{-1}}{\rho}\bar{\Psi}^{(1,1)}(s), \tag{B.10b}$$

$$G_{12}(s) = \frac{K_{12}}{\rho}\bar{\Psi}^{(1,0)}(s) + \frac{K_{12}\tau^{-1}}{\rho}\bar{\Psi}^{(0,1)}(s), \tag{B.10c}$$

$$G_{21}(s) = \frac{K_{21}}{\rho}\bar{\Psi}^{(1,0)}(s), \tag{B.10d}$$

The determinant $D(s)$ can be written in this case as

$$D(s) = 1 - a\Omega(s+\beta p) - \bar{b}\Omega(s+\beta p)e^{-(s+\beta p)}, \tag{B.11}$$

where a is still given by Eq. (2.53) and $\bar{b} \equiv x_1 x_2 K_{11} K_{22}\tau^{-1}$. Using the mathematical identity

$$\left(1 - ax - \bar{b}xy\right)^{-1} = \sum_{n=0}^{\infty}\sum_{\ell=0}^{n}\bar{C}_{n,\ell}x^n y^\ell, \quad \bar{C}_{n,\ell} \equiv \frac{n!}{\ell!(n-\ell)!}a^{n-\ell}\bar{b}^\ell, \tag{B.12}$$

we have

$$\bar{\Psi}^{(k_1,k_2)}(s) = \sum_{n=0}^{\infty}\sum_{\ell=0}^{n}\bar{C}_{n,\ell}\frac{e^{-(n+\ell+k_1+k_2)(s+\beta p)}}{(s+\beta p)^{n+k_1}}. \tag{B.13}$$

Thus, the Laplace property (2.59) allows us to write the inverse Laplace transform of $\bar{\Psi}^{(k_1,k_2)}(s)$ as

$$\bar{\psi}^{(k_1,k_2)}(r) = e^{-\beta p r} \sum_{n=0}^{\infty} \sum_{\ell=0}^{n} \bar{C}_{n,\ell} \frac{(r-n-\ell-k_1-k_2)^{n+k_1-1}}{(n+k_1-1)!} \Theta(r-n-\ell-k_1-k_2). \tag{B.14}$$

This expression holds if $k_1 > 0$. On the other hand, if $k_1 = 0$,

$$\bar{\psi}^{(0,k_2)}(r) = e^{-\beta p r} \left[\delta(r-k_2) + \sum_{n=1}^{\infty} \sum_{\ell=0}^{n} \bar{C}_{n,\ell} \frac{(r-n-\ell-k_2)^{n-1}}{(n-1)!} \Theta(r-n-\ell-k_2) \right], \tag{B.15}$$

where use has been made of $\mathcal{L}^{-1}\left[e^{-n(s+\beta p)}\right] = e^{-\beta p r}\delta(r-n)$.

C

Exact low-density properties for anisotropic SHS mixtures

C.1 Cavity function to first order in density

To first order in density, the cavity function of an anisotropic mixture is

$$y_{ij}(\mathbf{r}) = 1 + y_{ij}^{(1)}(\mathbf{r})\rho + \mathcal{O}(\rho^2), \tag{C.1}$$

where

$$y_{ij}^{(1)}(\mathbf{r}) = \sum_k x_k y_{ij;k}^{(1)}(\mathbf{r}), \tag{C.2}$$

with

$$y^{(1)}_{ij;k}(\mathbf{r}) = \int d\mathbf{r}'\, f_{ik}(\mathbf{r}')f_{kj}(\mathbf{r}-\mathbf{r}'). \tag{C.3}$$

Here, $f_{ij}(\mathbf{r}) = e^{-\beta\phi_{ij}(\mathbf{r})} - 1$ is the Mayer function. In the particular case of the anisotropic SHS potential considered in this paper,

$$\begin{aligned} f_{ij}(\mathbf{r}) &= f_{\rm HS}(r) + \delta(r-1)\left[t_{ij}\Theta(\cos\theta) + t_{ji}\Theta(-\cos\theta)\right] \\ &= f^{\rm SHS}_{ji}(r) + t^{-}_{ij}\delta(r-1)\Theta(\cos\theta), \end{aligned} \tag{C.4}$$

where we have taken $\sigma = 1$, $t^{-}_{ij} \equiv t_{ij} - t_{ji}$, and

$$f_{\rm HS}(r) = -\Theta(1-r), \quad f^{\rm SHS}_{ji}(r) = f_{\rm HS}(r) + t_{ji}\delta(r-1). \tag{C.5}$$

Inserting Eq. (C.4) into Eq. (C.3), we get

$$\begin{aligned} y^{(1)}_{ij;k}(\mathbf{r}) &= \Theta(2-r)\left\{\frac{\pi}{12}(2-r)^2(4+r) - (t_{ki}+t_{jk})\pi(2-r)\right. \\ &\quad + t_{ki}t_{jk}2\pi\left[2\delta(r) + \frac{1}{r}\right] - (t^{-}_{ik}+t^{-}_{kj})\mathcal{A}(\mathbf{r}) \\ &\quad \left. + (t^{-}_{ik}t_{jk} + t^{-}_{kj}t_{ki})\mathcal{L}(\mathbf{r}) + t^{-}_{ik}t^{-}_{kj}\mathcal{L}_0(\mathbf{r})\right\}, \end{aligned} \tag{C.6}$$

where

$$\mathcal{A}(\mathbf{r}) \equiv \int d\mathbf{r}'\, \delta(r'-1)\Theta(1-|\mathbf{r}-\mathbf{r}'|)\Theta(z'), \tag{C.7a}$$

$$\mathcal{L}(\mathbf{r}) \equiv \int d\mathbf{r}'\, \delta(r'-1)\delta(|\mathbf{r}-\mathbf{r}'|-1)\Theta(z'), \tag{C.7b}$$

$$\mathcal{L}_0(\mathbf{r}) \equiv \int d\mathbf{r}'\, \delta(r'-1)\delta(|\mathbf{r}-\mathbf{r}'|-1)\Theta(z')\Theta(z-z'). \tag{C.7c}$$

It can be proved that

$$\mathcal{A}(\mathbf{r}) = \begin{cases} \pi(2-r), & \sqrt{1-r^2/4} \le \cos\theta \le 1, \\ A(r/2,\theta), & |\cos\theta| \le \sqrt{1-r^2/4}, \\ 0, & -1 \le \cos\theta \le -\sqrt{1-r^2/4}, \end{cases} \tag{C.8a}$$

$$\mathcal{L}(\mathbf{r}) = \begin{cases} 2\pi/r, & \sqrt{1-r^2/4} \le \cos\theta \le 1, \\ L(r/2,\theta), & |\cos\theta| \le \sqrt{1-r^2/4}, \\ 0, & -1 \le \cos\theta \le -\sqrt{1-r^2/4}, \end{cases} \tag{C.8b}$$

$$\mathcal{L}_0(\mathbf{r}) = \begin{cases} 2\pi/r, & \sqrt{1-r^2/4} \le \cos\theta \le 1, \\ L_0(r/2,\theta), & 0 \le \cos\theta \le \sqrt{1-r^2/4}, \\ 0, & \cos\theta \le 0, \end{cases} \tag{C.8c}$$

where

$$A(\ell,\theta) = 2\pi\Theta(\cos\theta) - \pi\ell - 2\ell\sin^{-1}\frac{\ell\cos\theta}{\sqrt{1-\ell^2}\sin\theta} - 2\tan^{-1}\frac{\sqrt{\sin^2\theta-\ell^2}}{\cos\theta}, \tag{C.9a}$$

$$\begin{aligned} L(\ell,\theta) &= -\frac{1}{2\ell}\frac{\partial}{\partial\ell}A(\ell,\theta) \\ &= \frac{1}{\ell}\left[\frac{\pi}{2} + \sin^{-1}\frac{\ell\cos\theta}{\sqrt{1-\ell^2}\sin\theta}\right], \end{aligned} \tag{C.9b}$$

$$\begin{aligned} L_0(\ell,\theta) &= L(\ell,\theta) - L(\ell,\pi-\theta) \\ &= \frac{2}{\ell}\sin^{-1}\frac{\ell\cos\theta}{\sin\theta\sqrt{1-\ell^2}}. \end{aligned} \tag{C.9c}$$

In Eqs. (C.8b) and (C.8c) we have omitted terms proportional to $\delta(r)$ since they will not contribute to $g_{ij}(\mathbf{r})$. Note the symmetry relations $\mathcal{A}(\mathbf{r})+\mathcal{A}(-\mathbf{r}) = \pi(2-r)$, $\mathcal{L}(\mathbf{r}) + \mathcal{L}(-\mathbf{r}) = 2\pi/r$, $\mathcal{L}(\mathbf{r}) - \mathcal{L}(-\mathbf{r}) = \mathcal{L}_0(\mathbf{r}) - \mathcal{L}_0(-\mathbf{r})$.

The orientational average

$$\overline{y}^{(1)}_{ij;k}(r) = \int_0^{\pi/2} d\theta\, \sin\theta y^{(1)}_{ij;k}(\mathbf{r}) \tag{C.10}$$

becomes

$$\begin{aligned}\overline{y}^{(1)}_{ij;k}(r) &= \Theta(2-r)\Big\{\frac{\pi}{12}(2-r)^2(4+r) - (t_{ki}+t_{jk})\pi(2-r) \\ &\quad + t_{ki}t_{jk}2\pi\left[2\delta(r)+\frac{1}{r}\right] - (t^-_{ik}+t^-_{kj})\overline{\mathcal{A}}(r) \\ &\quad + (t^-_{ik}t_{jk}+t^-_{kj}t_{ki})\overline{\mathcal{L}}(r) + t^-_{ik}t^-_{kj}\overline{\mathcal{L}}_0(r)\Big\}, \end{aligned} \tag{C.11}$$

where

$$\overline{\mathcal{A}}(r) = \pi(2-r)\left(1-\sqrt{1-r^2/4}\right) + \overline{A}(r/2), \tag{C.12a}$$

$$\overline{\mathcal{L}}(r) = \frac{2\pi}{r}\left(1-\sqrt{1-r^2/4}\right) + \overline{L}(r/2), \tag{C.12b}$$

$$\overline{\mathcal{L}}_0(r) = \frac{2\pi}{r}\left(1-\sqrt{1-r^2/4}\right) + \overline{L}_0(r/2), \tag{C.12c}$$

with

$$\begin{aligned}\overline{A}(\ell) &= \int_{\sin^{-1}\ell}^{\pi/2} d\theta\, \sin\theta A(\ell,\theta) \\ &= 2\sqrt{1-\ell^2}\,(\pi - \pi\ell - 1) + 2\ell\cos^{-1}\ell, \end{aligned} \tag{C.13a}$$

$$\begin{aligned}\overline{L}(\ell) &= \int_{\sin^{-1}\ell}^{\pi/2} d\theta\, \sin\theta L(\ell,\theta) \\ &= \frac{1}{\ell}\left(\pi\sqrt{1-\ell^2} - \cos^{-1}\ell\right), \end{aligned} \tag{C.13b}$$

$$\begin{aligned}\overline{L}_0(\ell) &= \int_{\sin^{-1}\ell}^{\pi/2} d\theta\, \sin\theta L_0(\ell,\theta) \\ &= \frac{1}{\ell}\left(\pi\sqrt{1-\ell^2} - 2\cos^{-1}\ell\right). \end{aligned} \tag{C.13c}$$

C.2 Second and third virial coefficients

The series expansion of the compressibility factor Z in powers of density defines the virial coefficients:

$$Z = 1 + B_2\rho + B_3\rho^2 + \cdots . \tag{C.14}$$

Using Eq. (C.1) in Eq. (3.32a), one can identify

$$B_2 = \frac{2\pi}{3}\left(1 - 3\sum_{i,j} x_i x_j t_{ij}\right), \tag{C.15a}$$

$$B_3 = \frac{2\pi}{3}\sum_{i,j,k} x_i x_j x_k \left[(1-3t_{ij})\overline{y}^{(1)}_{ij;k}(1) - t_{ij}\overline{y}^{(1)\,\prime}_{ij;k}(1)\right]. \tag{C.15b}$$

According to Eq. (C.11),

$$\begin{aligned}\overline{y}^{(1)}_{ij;k}(1) &= \frac{5\pi}{12} - (t_{ki}+t_{jk})\pi + t_{ki}t_{jk}2\pi - (t^-_{ik}+t^-_{kj})\overline{\mathcal{A}}(1) \\ &\quad +(t^-_{ik}t_{jk}+t^-_{kj}t_{ki})\overline{\mathcal{L}}(1) + t^-_{ik}t^-_{kj}\overline{\mathcal{L}}_0(1),\end{aligned} \tag{C.16a}$$

$$\begin{aligned}\overline{y}^{(1)\,\prime}_{ij;k}(1) &= -\frac{3}{4}\pi + (t_{ki}+t_{jk})\pi - t_{ki}t_{jk}2\pi - (t^-_{ik}+t^-_{kj})\overline{\mathcal{A}}'(1) \\ &\quad +(t^-_{ik}t_{jk}+t^-_{kj}t_{ki})\overline{\mathcal{L}}'(1) + t^-_{ik}t^-_{kj}\overline{\mathcal{L}}'_0(1),\end{aligned} \tag{C.16b}$$

where

$$\overline{\mathcal{A}}(1) = \frac{4\pi}{3} - \sqrt{3}, \quad \overline{\mathcal{A}}'(1) = -\frac{2\pi}{3}, \tag{C.17a}$$

$$\overline{\mathcal{L}}(1) = \frac{4\pi}{3}, \quad \overline{\mathcal{L}}'(1) = -\frac{2}{3}\left(2\pi - \sqrt{3}\right), \tag{C.17b}$$

$$\overline{\mathcal{L}}_0(1) = \frac{2\pi}{3}, \quad \overline{\mathcal{L}}'_0(1) = -\frac{2}{3}\left(\pi - 2\sqrt{3}\right). \tag{C.17c}$$

The second and third virial coefficients can also be obtained from the compressibility equation (3.19). To that end, note that

$$\widehat{h}_{ij}(0) = \widehat{h}^{(1)}_{ij}(0)\rho + \widehat{h}^{(2)}_{ij}(0)\rho^2 + \cdots, \tag{C.18}$$

where, according to Eq. (3.18),

$$\widehat{h}^{(1)}_{ij}(0) = \sqrt{x_i x_j}2\pi\left(-\frac{2}{3} + t_{ij} + t_{ji}\right), \tag{C.19a}$$

$$\widehat{h}^{(2)}_{ij}(0) = \sqrt{x_i x_j}2\pi\left\{t_{ij}\overline{y}^{(1)}_{ij}(1) + t_{ji}\overline{y}^{(1)}_{ji}(1) + \int_1^2 dr\, r^2\left[\overline{y}^{(1)}_{ij}(r) + \overline{y}^{(1)}_{ji}(r)\right]\right\}. \tag{C.19b}$$

Inserting this into Eq. (3.19) and making use of Eqs. (C.11)–(C.13c), one gets $\chi_T^{-1} = 1 + 2B_2\rho + 3B_3\rho^2 + \cdots$, with B_2 and B_3 given by Eqs. (C.15a) and (C.15b), respectively. Furthermore, it can be checked that the exact consistency condition (3.34) is satisfied by Eqs. (C.1), (C.2), (C.16a), and (C.16b). The verification of these two thermodynamic consistency conditions represent stringent tests on the correctness of the results derived in this Appendix.

C.3 Case $t_{11} = t_{22} = t_{21} = 0$

Thus far, we have assumed general values for the stickiness parameters t_{ij}. On the other hand, significant simplifications occur in our constrained Janus model, where $t_{ij} = t\delta_{i1}\delta_{j2}$. More specifically,

$$\begin{aligned} y_{11}^{(1)}(\mathbf{r}) &= \Theta(2-r)\Big\{\frac{\pi}{12}(2-r)^2(4+r) \\ &\quad -x_2 t\left[\pi(2-r) - t\mathcal{L}(\mathbf{r}) + t\mathcal{L}_0(\mathbf{r})\right]\Big\}, \end{aligned} \tag{C.20a}$$

$$y_{12}^{(1)}(\mathbf{r}) = \Theta(2-r)\left[\frac{\pi}{12}(2-r)^2(4+r) - t\mathcal{A}(\mathbf{r})\right], \tag{C.20b}$$

$$\overline{y}_{11}^{(1)}(r) = \Theta(2-r)\Big[\frac{\pi}{12}(2-r)^2(4+r) - x_2\pi t\Big(2 - r - \frac{2t}{\pi r}\cos^{-1}\frac{r}{2}\Big)\Big], \tag{C.20c}$$

$$\begin{aligned} \overline{y}_{12}^{(1)}(r) &= \Theta(2-r)\Big\{\frac{\pi}{12}(2-r)^2(4+r) \\ &\quad -t\Big[\pi(2-r) - 2\sqrt{1-r^2/4} + r\cos^{-1}\frac{r}{2}\Big]\Big\}, \end{aligned} \tag{C.20d}$$

$$\overline{y}_{21}^{(1)}(r) = \Theta(2-r)\Big\{\frac{\pi}{12}(2-r)^2(4+r) - t\Big[2\sqrt{1-r^2/4} - r\cos^{-1}\frac{r}{2}\Big]\Big\}, \tag{C.20e}$$

$$\overline{y}^{(1)}(r) = \Theta(2-r)\Big[\frac{\pi}{12}(2-r)^2(4+r) - x_1x_2 2\pi t\Big(2 - r - \frac{t}{\pi r}\cos^{-1}\frac{r}{2}\Big)\Big], \tag{C.20f}$$

$$\overline{y}_{11}^{(1)}(1) = \frac{5\pi}{12} - x_2\pi t\left(1 - \frac{2t}{3}\right), \tag{C.20g}$$

$$\overline{y}_{12}^{(1)}(1) = \frac{5\pi}{12} - t\left(\frac{4\pi}{3} - \sqrt{3}\right), \tag{C.20h}$$

$$\overline{y}_{21}^{(1)}(1) = \frac{5\pi}{12} - t\left(\sqrt{3} - \frac{\pi}{3}\right), \tag{C.20i}$$

$$\overline{y}_{11}^{(1)\prime}(1) = -\frac{3\pi}{4} + x_2 t\left[\pi - \frac{2t}{3}\left(\pi + \sqrt{3}\right)\right], \tag{C.20j}$$

$$\overline{y}_{12}^{(1)\prime}(1) = -\frac{3\pi}{4} + t\frac{2\pi}{3}, \tag{C.20k}$$

$$\overline{y}_{21}^{(1)\prime}(1) = -\frac{3\pi}{4} + t\frac{\pi}{3}, \tag{C.20l}$$

$$\overline{y}^{(1)}(1) = \frac{5\pi}{12} - x_1 x_2 2\pi t\left(1 - \frac{t}{3}\right), \tag{C.20m}$$

$$\overline{y}^{(1)\prime}(1) = -\frac{3\pi}{4} + x_1 x_2 2t\left[\pi - \frac{t}{3}\left(\pi + \sqrt{3}\right)\right], \tag{C.20n}$$

$$\frac{6}{\pi}B_2 = 4\left(1 - 3x_1 x_2 t\right), \tag{C.20o}$$

$$\left(\frac{6}{\pi}\right)^2 B_3 = 10\left\{1 - 6x_1 x_2 t\left[1 - \frac{2}{5}\left(4 - 3\frac{\sqrt{3}}{\pi}\right)t\right]\right\}, \tag{C.20p}$$

$$\frac{u_{\text{ex}}}{\epsilon} = -12\eta x_1 x_2 t\left\{1 + \frac{5}{2}\left[1 - \frac{4}{5}\left(4 - 3\frac{\sqrt{3}}{\pi}\right)t\right]\eta\right\} + \mathcal{O}(\eta^2). \tag{C.20q}$$

D

Evaluation of the coefficients $L_{ij}^{(0)}$, $L_{ij}^{(1)}$, and $L_{ij}^{(2)}$

In order to apply Eq. (3.24), it is convenient to rewrite Eq. (3.51) as

$$\frac{1}{2\pi}\mathsf{L}(s) \;=\; \mathsf{Q}(s)\cdot[\mathsf{I}-\mathsf{A}(s)]\,, \tag{D.1}$$

where we have introduced the matrix Q as

$$Q_{ij}(s) \;\equiv\; e^s s^2 G_{ij}(s). \tag{D.2}$$

Thus, Eq. (3.24) is equivalent to

$$Q_{ij}(s) \;=\; 1+s+\mathcal{O}(s^2). \tag{D.3}$$

Expanding $A_{ij}(s)$ in powers of s and inserting the result into Eq. (D.1), one gets

$$\frac{1}{2\pi}L_{ij}^{(0)} = 1 - \sum_k A_{kj}^{(0)}, \tag{D.4a}$$

$$\frac{1}{2\pi}L_{ij}^{(1)} = 1 - \sum_k \left(A_{kj}^{(1)} + A_{kj}^{(0)}\right), \tag{D.4b}$$

where

$$A_{ij}^{(n)} = (-1)^n \rho x_i \left[\frac{L_{ij}^{(0)}}{(n+3)!} - \frac{L_{ij}^{(1)}}{(n+2)!} + \frac{L_{ij}^{(2)}}{(n+1)!}\right]. \tag{D.5}$$

Equations (D.4a) and (D.4b) constitute a *linear* set of equations which allow us to express the coefficients $L_{ij}^{(0)}$ and $L_{ij}^{(1)}$ in terms of the coefficients $\{L_{kj}^{(2)}\}$. The result is given by Eqs. (3.53a) and (3.53b).

It now remains the determination of $L_{ij}^{(2)}$. This is done by application of Eq. (3.39), i.e., the ratio first term to second term in the expansion of $e^s G_{ij}(s)$ for large s must be exactly equal to t_{ij}. This is the only point where the stickiness parameters of the mixture appear explicitly.

The large-s behavior from Eq. (3.51) is

$$2\pi e^s G_{ij}(s) = L_{ij}^{(2)} + \left[L_{ij}^{(1)} + \left(\mathsf{L}^{(2)} \cdot \mathsf{D}\right)_{ij}\right] s^{-1} + \mathcal{O}(s^{-2}), \tag{D.6}$$

where

$$\begin{aligned} D_{ij} &\equiv \rho x_i \left(\frac{1}{2}L_{ij}^{(0)} - L_{ij}^{(1)} + L_{ij}^{(2)}\right) \\ &= \rho x_i \left(L_{ij}^{(2)} - \frac{\pi}{1-\eta}\right). \end{aligned} \tag{D.7}$$

Comparison of Eq. (3.38) with Eq. (D.6) yields Eq. (3.55) and

$$\frac{12\tau_{ij}L_{ij}^{(2)}}{\sigma_{ij}} = L_{ij}^{(1)} + \sum_{k=1}^{m} L_{ik}^{(2)} D_{kj}. \tag{D.8a}$$

$$\frac{L_{ij}^{(2)}}{t_{ij}} = L_{ij}^{(1)} + \sum_k L_{ik}^{(2)} D_{kj}. \tag{D.8b}$$

Taking into account Eqs. (3.53b) and (D.7), Eq. (D.8b) becomes Eq. (3.54).

E

Recovery of the pseudo-PY solution

The aim of this appendix is to prove that the pair correlation functions $\overline{g}_{ij}(r)$ obtained from the RFA method in Sec. 3.5.2 satisfy Eqs. (3.42) and (3.45).

First, note that the pseudo-OZ relation (3.45) can be rewritten in the form

$$\widehat{\overline{\mathsf{c}}}(q) = \widehat{\overline{\mathsf{h}}}(q) \cdot \Big[\mathsf{I} + \widehat{\overline{\mathsf{h}}}(q)\Big]^{-1}, \tag{E.1}$$

where I is the unit matrix and

$$\widehat{\overline{c}}_{ij}(q) = \rho\sqrt{x_i x_j} \int d\mathbf{r}\, e^{-i\mathbf{q}\cdot\mathbf{r}} \overline{c}_{ij}(r), \tag{E.2a}$$

$$\widehat{\overline{h}}_{ij}(q) = \rho\sqrt{x_i x_j} \int d\mathbf{r}\, e^{-i\mathbf{q}\cdot\mathbf{r}} \overline{h}_{ij}(r). \tag{E.2b}$$

Note that $\widehat{h}_{ij}(0) = \frac{1}{2}\left[\widehat{\overline{h}}_{ij}(0) + \widehat{\overline{h}}_{ji}(0)\right]$, where $\widehat{h}_{ij}(0)$ is defined by Eq. (3.18).

The Fourier transform $\widehat{\overline{h}}_{ij}(q)$ of the (orientational average) total correlation function $\overline{h}_{ij}(r) = \overline{g}_{ij}(r) - 1$ is related to the Laplace transform $G_{ij}(s)$ [see Eq. (3.20)] by

$$\widehat{\overline{h}}_{ij}(q) = -2\pi\rho\sqrt{x_i x_j}\left[\frac{G_{ij}(s) - G_{ij}(-s)}{s}\right]_{s=iq}. \tag{E.3}$$

Making use of Eqs. (3.51)–(3.52b), it is possible to obtain, after some algebra,

$$\begin{aligned}\frac{\widehat{\overline{c}}_{ij}(q)}{\rho\sqrt{x_i x_j}} &= \frac{4\pi}{q^3}C_{ij}^{(0)}\left(\sin q - q\cos q\right) + \frac{4\pi}{q^4}C_{ij}^{(1)}\left[2q\sin q\right. \\ &\quad \left. -2 - \left(q^2-2\right)\cos q\right] + \frac{4\pi}{q^6}C_{ij}^{(3)}\left[4q\left(q^2-6\right)\sin q\right. \\ &\quad \left. +24 - \left(24 - 12q^2 + q^4\right)\cos q\right] + 4\pi t_{ij}y_{ij}(1)\frac{\sin q}{q},\end{aligned} \tag{E.4}$$

where the coefficients $C_{ij}^{(0)}$, $C_{ij}^{(1)}$, and $C_{ij}^{(3)}$ are independent of q but depend on the density, the composition, and the stickiness parameters. Fourier inversion yields

$$\overline{c}_{ij}(r) = \left[C_{ij}^{(0)} + C_{ij}^{(1)}r + C_{ij}^{(3)}r^3\right]\Theta(1-r) + y_{ij}(1)t_{ij}\delta_+(r-1). \tag{E.5}$$

Taking into account Eq. (3.32c) we see that Eq. (E.5) has the structure

$$\overline{c}_{ij}(r) = \overline{g}_{ij}(r) - \overline{y}_{ij}(r). \tag{E.6}$$

But this is not but the PY closure relation (3.42). In passing, we get the cavity function inside the core:

$$y_{ij}(r)\Theta(1-r) = -\left[C_{ij}^{(0)} + C_{ij}^{(1)}r + C_{ij}^{(3)}r^3\right]\Theta(1-r). \tag{E.7}$$

Bibliography

[1] C. N. Likos. Effective interactions in soft condensed matter physics. *Phys. Rep.*, 348:267–439, 2001. doi: 10.1016/S0370-1573(00)00141-1. URL `http://dx.doi.org/10.1016/S0370-1573(00)00141-1`.

[2] H. N. W. Lekkerkerker and R. Tuinier. *Colloids and the Depletion Interaction*, volume 833 of *Lecture Notes in Physics*. Springer, Heidelberg, 2011.

[3] K. H. Roh, D. C. Martin, and J. Lahann. Biphasic Janus particles with nanoscale anisotropy. *Nature Mater.*, 4:759–763, 2005. doi: 10.1038/nmat1486. URL `http://dx.doi.org/10.1016/S0370-1573(00)00141-1`.

[4] B. Wang, B. Li, B. Zhao, and C. Y. Li. Amphiphilic Janus gold nanoparticles via combining "solid-state grafting-to" and "grafting-from" methods. *J. Am. Chem. Soc.*, 130:11594–11595, 2008. doi: 10.1021/ja804192e. URL `http://dx.doi.org/10.1021/ja804192e`.

[5] A. Walther and A. H. E. Müller. Janus particles: Synthesis, self-assembly, physical properties, and applications. *Chem. Rev.*, 113:5194–5261, 2013. doi: 10.1021/cr300089t. URL `http://dx.doi.org/10.1021/cr300089t`.

[6] B. P. Binks and P. D. I. Fletcher. Particles adsorbed at the oil-water interface: A theoretical comparison between spheres of uniform wettability and "Janus" particles. *Langmuir*, 17:4708–4710, 2001. doi: 10.1021/la0103315. URL `http://dx.doi.org/10.1021/la0103315`.

[7] Riccardo Fantoni. *The Janus Fluid: A Theoretical Perspective*. Springer, New York, 2013.

[8] F. Sciortino, A. Giacometti, and G. Pastore. Phase diagram of Janus particles. *Phys. Rev. Lett.*, 103:237801, 2009. doi: 10.1103/PhysRevLett.103.237801. URL `http://dx.doi.org/10.1103/PhysRevLett.103.237801`.

[9] K. P. Yuet, D. K. Hwang, R. Haghgooie, and P. S. Doyle. Multifunctional superparamagnetic Janus particles. *Langmuir*, 26:4281–4287, 2010. doi: 10.1021/la903348s. URL `http://dx.doi.org/10.1021/la903348s`.

[10] S. Onishi, M. Tokuda, T. Suzuki, and H. Minami. Preparation of Janus particles with different stabilizers and formation of one-dimensional particle arrays. *Langmuir*, 31:674–678, 2015. doi: 10.1021/la504535k. URL `http://dx.doi.org/10.1021/la504535k`.

[11] P. G. de Gennes. Soft matter. *Rev. Mod. Phys.*, 64:645, 1992. doi: 10.1103/RevModPhys.64.645. URL `https://doi.org/10.1103/RevModPhys.64.645`.

[12] E. Bianchi, R. Blaak, and C. N. Likos. Patchy colloids: state of the art and perspectives. *Phys. Chem. Chem. Phys.*, 13:6397, 2011. doi: 10.1039/C0CP02296A. URL `https://doi.org/10.1039/C0CP02296A`.

[13] Z. L. Zhang and S. C. Glotzer. Self-assembly of patchy particles. *Nano Lett.*, 4:1407, 2004. doi: 10.1021/nl0493500. URL `https://doi.org/10.1021/nl0493500`.

[14] N. Kern and D. Frenkel. Fluid-fluid coexistence in colloidal systems with short-ranged strongly directional attraction. *J. Chem. Phys.*, 118:9882–9889, 2003. doi: 10.1063/1.1569473.

[15] F. Sciortino, A. Giacometti, and G. Pastore. A numerical study of one-patch colloidal particles: from square-well to janus. *Phys. Chem. Chem. Phys.*, 12:11869, 2010. doi: 10.1039/C0CP00504E. URL `https://doi.org/10.1039/C0CP00504E`.

[16] A. Giacometti, F. Lado, J. Largo, G. Pastore, and F. Sciortino. Phase diagram and structural properties of a simple model for one-patch particles. *J. Chem. Phys.*, 131:174114, 2009. doi: 10.1063/1.3256002. URL `https://doi.org/10.1063/1.3256002`.

[17] A. Giacometti, F. Lado, J. Largo, G. Pastore, and F. Sciortino. Effects of patch size and number within a simple model of patchy colloids. *J. Chem. Phys.*, 132:174110, 2010. doi: 10.1063/1.3415490. URL `https://doi.org/10.1063/1.3415490`.

[18] S. Gangwal, A. Pawar, I. Kretzschmar, and O. D. Velev. Programmed assembly of metallodielectric patchy particles in external AC electric fields. *Soft Matter*, 6:1413–1418, 2010. doi: 10.1039/B925713F. URL `https://doi.org/10.1039/B925713F`.

[19] S. Gangwal. *Directed Assembly and Manipulation of Anisotropic Colloidal Particles by External Fields*. ProQuest, UMI Dissertation Publishing, Ann Arbor, Michigan, 2011.

[20] M. A. G. Maestre and A. Santos. One-dimensional Janus fluids. Exact solution and mapping from the quenched to the annealed system. *J. Stat. Mech.*, 20: 06321, 2020. doi: 10.1088/1742-5468/ab900d. URL `http://dx.doi.org/10.1088/1742-5468/ab900d`.

[21] M. A. G. Maestre, R. Fantoni, A. Giacometti, and A. Santos. Janus fluid with fixed patch orientations: Theory and simulations. *J. Chem. Phys.*, 138: 094904, 2013. doi: 10.1063/1.4793626. URL `http://dx.doi.org/10.1063/1.4793626`.

[22] R. Fantoni, A. Giacometti, M. A. G. Maestre, and A. Santos. Phase diagrams of Janus fluids with up-down constrained orientations. *J. Chem. Phys.*, 139: 174902, 2013. doi: 10.1063/1.4827861. URL `http://dx.doi.org/10.1063/1.4827861`.

[23] M. E. Fisher and B. Widom. Decay of correlations in linear systems. *J. Chem. Phys.*, 50:3756–3772, 1969. doi: 10.1063/1.1671624. URL `http://dx.doi.org/10.1063/1.1671624`.

[24] J. L. Lebowitz and D. Zomick. Mixtures of hard spheres with nonadditive diameters: Some exact results and solution of PY equation. *J. Chem. Phys.*, 54:3335–3346, 1971. doi: 10.1063/1.1675348. URL `http://dx.doi.org/10.1063/1.1675348`.

[25] M. Heying and D. S. Corti. The one-dimensional fully non-additive binary hard rod mixture: Exact thermophysical properties. *Fluid Phase Equil.*, 220: 85–103, 2004. doi: 10.1016/j.fluid.2004.02.018. URL `http://dx.doi.org/10.1016/j.fluid.2004.02.018`.

[26] A. Santos. Playing with marbles: Structural and thermodynamic properties of hard-sphere systems. In B. Cichocki, M. Napiórkowski, and J. Piasecki, editors, *5th Warsaw School of Statistical Physics*, Warsaw, 2014. Warsaw University Press. http://arxiv.org/abs/1310.5578.

[27] A. Santos. *A Concise Course on the Theory of Classical Liquids. Basics and Selected Topics*, volume 923 of *Lecture Notes in Physics*. Springer, New York, 2016.

[28] R. Fantoni and A. Santos. One-dimensional fluids with second nearest-neighbor interactions. *J. Stat. Phys.*, 169:1171–1201, 2017. doi: 10.1007/s10955-017-1908-6. URL `http://dx.doi.org/10.1007/s10955-017-1908-6`.

[29] A. M. Montero and A. Santos. Triangle-well and ramp interactions in one-dimensional fluids: A fully analytic exact solution. *J. Stat. Phys.*, 175:269–288, 2019. doi: 10.1007/s10955-019-02255-x. URL `http://dx.doi.org/10.1007/s10955-019-02255-x`.

[30] J.-P. Hansen and I. R. McDonald. *Theory of Simple Liquids*. Academic, London, 3rd edition, 2006.

[31] L. Tonks. The complete equation of state of one, two and three-dimensional gases of hard elastic spheres. *Phys. Rev.*, 50:955–963, 1936. doi: 10.1103/PhysRev.50.955. URL http://dx.doi.org/10.1103/PhysRev.50.955.

[32] R. J. Baxter. Percus–Yevick equation for hard spheres with surface adhesion. *J. Chem. Phys.*, 49:2770–2774, 1968. doi: 10.1063/1.1670482. URL http://dx.doi.org/10.1063/1.1670482.

[33] P. Perry and G. J. Throop. Decay of pair correlations in hard sphere fluids. *J. Chem. Phys.*, 57:1827–1829, 1972. doi: 10.1063/1.1678497. URL https://doi.org/10.1063/1.1678497. Notice that the numerical values in the two last columns of Table I of this reference are not correct.

[34] R. Fantoni, A. Giacometti, Al. Malijevský, and A. Santos. A numerical test of a high-penetrability approximation for the one-dimensional penetrable-square-well model. *J. Chem. Phys.*, 133:024101, 2010. doi: 10.1063/1.3455330. URL http://dx.doi.org/10.1063/1.3455330.

[35] C. Grodon, M. Dijkstra, R. Evans, and R. Roth. Decay of correlation functions in hard-sphere mixtures: Structural crossover. *J. Chem. Phys.*, 121:7869–7882, 2004. doi: 10.1063/1.1798057. URL http://dx.doi.org/10.1063/1.1798057.

[36] A. Statt, R. Pinchaipat, F. Turci, R. Evans, and C. P. Royall. Direct observation in 3d of structural crossover in binary hard sphere mixtures. *J. Chem. Phys.*, 144:144506, 2016. doi: 10.1063/1.4945808. URL http://dx.doi.org/10.1063/1.4945808.

[37] S. Pieprzyk, A. C. Brańka, S. B. Yuste, A. Santos, and M. López de Haro. Structural properties of additive binary hard-sphere mixtures. *Phys. Rev. E*, 101:012117, 2020. doi: 10.1103/PhysRevE.101.012117. URL http://dx.doi.org/10.1103/PhysRevE.101.012117.

[38] D. Frenkel and B. Smit. *Understanding Molecular Simulation: From Algorithms to Applications*. Academic Press, San Diego, 2nd edition, 2002.

[39] H. G. Katzgraber. Introduction to Monte Carlo Methods. arXiv:0905.1629v3, 2011. URL https://arxiv.org/abs/0905.1629v3.

[40] R. Fantoni. Lectures on Quantum Monte Carlo, 2017. URL http://www-dft.ts.infn.it/~rfantoni/research/qmc.pdf.

[41] L. Hong, A. Cacciuto, E. Luijten, and S. Granick. Clusters of amphiphilic colloidal spheres. *Langmuir*, 24:621, 2008. doi: 10.1021/la7030818. URL http://dx.doi.org/10.1021/la7030818.

[42] A. Reinhardt, A. J. Williamson, J. P. K. Doye, J. Carrete, L. M. Varela, and A. A. Louis. Re-entrant phase behavior for systems with competition between phase separation and self-assembly. *J. Chem. Phys.*, 134:104905, 2011. doi: 10.1063/1.3557059. URL http://dx.doi.org/10.1063/1.3557059.

[43] R. Fantoni, A. Giacometti, F. Sciortino, and G. Pastore. Cluster theory of Janus particles. *Soft Matter*, 7:2419, 2011. doi: 10.1039/C0SM00995D. URL https://doi.org/10.1039/C0SM00995D.

[44] R. Fantoni. A cluster theory for a Janus fluid. *Eur. Phys. J. B*, 85:108, 2012. doi: 10.1140/epjb/e2012-20820-1. URL http://dx.doi.org/10.1140/epjb/e2012-20820-1.

[45] R. Zwanzig. Dielectric relaxation in a high-temperature dipole lattice. *J. Chem. Phys.*, 39:1714, 1963. doi: 10.1063/1.1733587. URL https://doi.org/10.1063/1.1733587.

[46] R. O. Watts, D. Henderson, and R. J. Baxter. Hard spheres with surface adhesion: The Percus–Yevick approximation and the energy equation. *Adv. Chem. Phys.*, 21:421–430, 1971. doi: 10.1002/9780470143698.ch27. URL https://doi.org/10.1002/9780470143698.ch27.

[47] J. W. Perram and E. R. Smith. A model for the examination of phase behaviour in multicomponent systems. *Chem. Phys. Lett.*, 35:138–140, 1975. doi: 10.1016/0009-2614(75)85604-1. URL http://dx.doi.org/10.1016/0009-2614(75)85604-1.

[48] B. Barboy. Solution of the compressibility equation of the adhesive hard-sphere model for mixtures. *Chem. Phys.*, 11:357–371, 1975. doi: 10.1016/0301-0104(75)80055-3. URL http://dx.doi.org/10.1016/0301-0104(75)80055-3.

[49] B. Barboy and R. Tenne. Distribution functions and equations of state of sticky hard sphere fluids in the Percus–Yevick approximation. *Chem. Phys.*, 38:369–387, 1979. doi: 10.1016/0301-0104(79)89011-4. URL https://doi.org/10.1016/0301-0104(79)89011-4.

[50] E. Zaccarelli, G. Foffi, K. A. Dawson, F. Sciortino, and P. Tartaglia. Mechanical properties of a model of attractive colloidal solutions1. *Phys. Rev. E*, 63:031501, 2001. doi: 10.1103/PhysRevE.63.031501. URL http://dx.doi.org/10.1103/PhysRevE.63.031501.

[51] R. Roth, R. Evans, A. Lang, and G. Kahl. Fundamental measure theory for hard-sphere mixtures revisited: The White Bear version. *Mol. Phys.*, 14:1025, 2002. doi: 10.1088/0953-8984/14/46/313. URL http://dx.doi.org/10.1016/S0370-1573(00)00141-1.

[52] R. Fantoni, D. Gazzillo, A. Giacometti, M. A. Miller, and G. Pastore. Patchy sticky hard spheres: Analytical study and Monte Carlo simulations. *J. Chem. Phys.*, 127:234507, 2007. doi: 10.1063/1.2805066. URL https://doi.org/10.1063/1.2805066.

[53] A. Santos, S. B. Yuste, and M. López de Haro. Radial distribution function for a multicomponent system of sticky hard spheres. *J. Chem. Phys.*, 109:6814–6819, 1998. doi: 10.1063/1.477328. URL https://doi.org/10.1063/1.477328.

[54] M. López de Haro, S. B. Yuste, and A. Santos. Alternative Approaches to the Equilibrium Properties of Hard-Sphere Liquids. In A. Mulero, editor, *Theory and Simulation of Hard-Sphere Fluids and Related Systems*, volume 753 of *Lecture Notes in Physics*, pages 183–245, Berlin, 2008. Springer.

[55] A. Santos, M. López de Haro, and S. B. Yuste. Structural and thermodynamic properties of hard-sphere fluids. *J. Chem. Phys.*, 153:120901, 2020. doi: 10.1063/5.0023903. URL http://dx.doi.org/10.1063/5.0023903.

[56] A. Santos. *A Concise Course on the Theory of Classical Liquids*. Springer, 2016. ISBN 9783319296661. doi: 10.1007/978-3-319-29668-5. URL http://dx.doi.org/10.1007/978-3-319-29668-5.

[57] A. Mulero, editor. *Theory and Simulation of Hard-Sphere Fluids and Related Systems*, volume 753 of *Lecture Notes in Physics*. Springer, Berlin, 2008.

[58] S. B. Yuste and A. Santos. Sticky hard spheres beyond the Percus–Yevick approximation. *Phys. Rev. E*, 48:4599–4604, 1993. doi: 10.1103/physreve.48.4599. URL http://dx.doi.org/10.1103/physreve.48.4599.

[59] L. Acedo. Continuity conditions for the radial distribution function of square-well fluids. *J. Stat. Phys.*, 99:707–723, 2000. doi: 10.1023/A:1018631109833, url={https://doi.org/10.1023/A:1018631109833}.

[60] J. Abate and W. Whitt. The Fourier-series method for inverting transforms of probability distributions. *Queueing Syst.*, 10:5–88, 1992. doi: 10.1007/BF01158520. URL http://dx.doi.org/10.1007/BF01158520.

[61] A. Santos. On the equivalence between the energy and virial routes to the equation of state of hard-sphere fluids. *J. Chem. Phys.*, 123:104102, 2005. doi: 10.1063/1.1992469. URL https://doi.org/10.1063/1.1992469.

[62] A. Santos. Are the energy and virial routes to thermodynamics equivalent for hard spheres? *Mol. Phys.*, 104:3411–3418, 2006. doi: 10.1080/00268970600968011. URL https://doi.org/10.1080/00268970600968011.

[63] N. F. Carnahan and K. E. Starling. Equation of state for nonattracting rigid spheres. *J. Chem. Phys.*, 51:635–636, 1969. doi: 10.1063/1.1672048. URL http://dx.doi.org/10.1063/1.1672048.

[64] G. Stell. Sticky spheres and related systems. *J. Stat. Phys.*, 63:1203–1221, 1991. doi: 10.1007/BF01030007. URL https://doi.org/10.1007/BF01030007.

[65] M. A. Miller and D. Frenkel. Competition of percolation and phase separation in a fluid of adhesive hard spheres. *Phys. Rev. Lett.*, 90:135702, 2003. doi: 10.1103/PhysRevLett.90.135702. URL http://dx.doi.org/10.1103/PhysRevLett.90.135702.

[66] M. A. Miller and D. Frenkel. Phase diagram of the adhesive hard sphere fluid. *J. Chem. Phys.*, 121:535–545, 2004. doi: 10.1063/1.1758693. URL http://dx.doi.org/10.1063/1.1758693.

[67] Al. Malijevský, S. B. Yuste, and A. Santos. How "sticky" are short-range square-well fluids? *J. Chem. Phys.*, 125:074507, 2006. doi: 10.1063/1.2244549. URL http://dx.doi.org/10.1063/1.2244549.

[68] M. G. Noro and D. Frenkel. Extended corresponding-states behavior for particles with variable range attractions. *J. Chem. Phys.*, 113:2941–2944, 2000. doi: 10.1063/1.1288684. URL https://doi.org/10.1063/1.1288684.

[69] P. Bolhuis, M. Hagen, and D. Frenkel. Isostructural solid-solid transition in crystalline systems with short-ranged interaction. *Phys. Rev. E*, 50:4880, 1994. doi: 10.1103/PhysRevE.50.4880. URL https://doi.org/10.1103/PhysRevE.50.4880.

[70] E. Lomba and N. G. Almarza. Role of the interaction range in the shaping of phase diagrams in simple fluids. The hard sphere Yukawa fluid as a case study. *J. Chem. Phys.*, 100:8367–8372, 1994. doi: 10.1063/1.466781. URL http://dx.doi.org/10.1063/1.466781.

[71] M. H. J. Hagen and D. Frenkel. Determination of phase diagrams for the hard-core attractive Yukawa system. *J. Chem. Phys.*, 101:4093–4097, 1994. doi: 10.1063/1.467526. URL https://doi.org/10.1063/1.467526.

[72] L. Mederos and G. Navascués. Solid-to-solid isostructural transition in the hard sphere/attractive Yukawa system. *J. Chem. Phys.*, 101:9841, 1994. doi: 10.1063/1.467950. URL https://doi.org/10.1063/1.467950.

[73] E. Zaccarelli, G. Foffi, P. Tartaglia, F. Sciortino, and K.A. Dawson. Binary mixtures of sticky spheres using Percus-Yevick theory. *Prog. Colloid Polym. Sci.*, 115:371, 2000. doi: 10.1007/3-540-46545-6_71. URL http://dx.doi.org/10.1007/3-540-46545-6_71.

[74] A. Z. Panagiotopoulos. Direct determination of phase coexistence properties of fluids by Monte Carlo simulation in a new ensemble. *Mol. Phys.*, 61:813, 1987. doi: 10.1080/00268978700101491. URL https://doi.org/10.1080/00268978700101491.

[75] B. Smit, Ph. de Smedt, and D. Frenkel. Computer simulations in the Gibbs ensemble. *Mol. Phys.*, 68:931, 1989. doi: 10.1080/00268978900102641. URL https://doi.org/10.1080/00268978900102641.

[76] B. Smit and D. Frenkel. Calculation of the chemical potential in the Gibbs ensemble. *Mol. Phys.*, 68:951, 1989. doi: 10.1080/00268978900102651. URL https://doi.org/10.1080/00268978900102651.

[77] H. Liu, S. Garde, and S. Kumar. Direct determination of phase behavior of square-well fluids. *J. Chem. Phys.*, 123:174505, 2005. doi: 10.1063/1.2085051. URL https://doi.org/10.1063/1.2085051.

[78] T. Vissers, Z. Preisler, F. Smallenburg, M. Dijkstra, and F. Sciortino. Predicting crystals of Janus colloids. *J. Chem. Phys.*, 138:164505, 2013. doi: 10.1351/10.1063/1.4801438. URL https://doi.org/10.1063/1.4801438.

[79] J. V. Sengers and J. M. H. Levelt-Sengers. In C. A. Croxton, editor, *Progress in Liquid Physics*, chapter 4. Wiley, Chichester, 1978.

[80] F. Wegner. Corrections to scaling laws. *Phys. Rev. B*, 5:4529, 1972. doi: 10.1103/PhysRevB.5.4529. URL https://doi.org/10.1103/PhysRevB.5.4529.

[81] N. B. Wilding. Critical-point and coexistence-curve properties of the Lennard-Jones fluid: A finite-size scaling study. *Phys. Rev. E*, 52:602, 1995. doi: PhysRevE.52.602. URL https://doi.org/10.1103/PhysRevE.52.602.

[82] N.B. Wilding, F. Schmid, and P. Nielaba. Liquid-vapor phase behavior of a symmetrical binary fluid mixture. *Phys. Rev. E*, 58:2201, 1998. doi: 10.1103/PhysRevE.58.2201. URL https://doi.org/10.1103/PhysRevE.58.2201.

[83] R. Fantoni, D. Gazzillo, and A. Giacometti. Thermodynamic instabilities of a binary mixture of sticky hard spheres. *Phys. Rev. E*, 72:011503, 2005. doi: 10.1103/PhysRevE.72.029904. URL http://dx.doi.org/10.1103/PhysRevE.72.029904.

[84] W. M. Jacobs and D. Frenkel. Predicting phase behavior in multicomponent mixtures. *J. Chem. Phys.*, 139:024108, 2013. doi: 10.1063/1.4812461. URL http://dx.doi.org/10.1063/1.4812461.

[85] C. Gögelein, F. Romano, F. Sciortino, and A. Giacometti. Fluid-fluid and fluid-solid transitions in the Kern-Frenkel model from Barker-Henderson thermodynamic perturbation theory. *J. Chem. Phys.*, 136:094512, 2012. doi: 10.1063/1.3689308. URL https://doi.org/10.1063/1.3689308.

[86] E. Bianchi, J. Largo, E. Zaccarelli, and F. Sciortino. Phase diagram of patchy colloids: Towards empty liquids. *Phys. Rev. Lett.*, 97:168301, 2006. doi: 10.1103/PhysRevLett.97.168301. URL https://doi.org/10.1103/PhysRevLett.97.168301.

[87] L. van Hove. Sur l'intégrale de configuration pour les systèmes de particules à une dimension. *Physica*, 16:137–143, 1950. doi: 10.1016/0031-8914(50)90072-3. URL http://dx.doi.org/10.1016/0031-8914(50)90072-3.